October 2018

EXPERIMENTAL INVESTIGATION OF HYDRAULIC FRACTURING FLUID ON SHALE AND SOIL

Zhenning Yang

EXPERIMENTAL INVESTIGATION OF HYDRAULIC FRACTURING FLUID ON SHALE AND SOIL

A Dissertation Presented

by

ZHENNING YANG

Submitted to the Graduate School of the
University of Massachusetts Amherst in partial fulfillment
of the requirements for the degree of

DOCTOR OF PHILOSOPHY

September 2018

Department of Civil and Environmental Engineering

EXPERIMENTAL INVESTIGATION OF HYDRAULIC FRACTURING FLUID ON SHALE AND SOIL

A Dissertation Presented

by

ZHENNING YANG

Approved as to style and content by:

_____
Dr. Carlton L. Ho, Chair

_____
Dr. David A. Reckhow, Member

_____
Dr. Guoping Zhang, Member

_____
Dr. Baoshan Xing, Member

_____
Richard N. Palmer, Department Head
Department of Civil and Environmental Engineering

DEDICATION

To my beloved grandparents, Mr. Changqing Yang and Mrs. Cunhui Li who passed away during my Ph.D. program.

ACKNOWLEDGMENTS

I would like to thank my advisor, Dr. Carlton L. Ho for all his consistent support and guidance throughout the years. He has been such a great mentor in both my studies and my daily life. I would also like to extend my gratitude to my co-advisor, Dr. Guoping Zhang for leading me into the powerful tool: nanoindentation. Special thanks to my committee members, Dr. David A. Reckhow and Dr. Baoshan Xing for sharing their expertise and advice during the course of my research. I would also like to thank Dr. Ching S. Chang for his continuously care and encouragement since I came to the United States.

I would like to show my appreciation to Dr. Thomas J. McCarthy and Dr. Liming Wang, who generously shared their time and provided polymer synthesis support for my research. Many thanks to all the graduate students who helped me in different stages of this project.

I am thankful for my parents, Mr. Jianxin Yang and Mrs. Jingyi Wang, for their selfless love and understanding. I want to thank my wife, Xiaoran, who has been very encouraging and supporting all these years, and my son, Frederick, who writes new chapter in my life.

ABSTRACT

EXPERIMENTAL INVESTIGATION OF HYDRAULIC FRACTURING FLUID ON SHALE AND SOIL

SEPTEMBER 2018

ZHENNING YANG

B.S., LIAONING TECHNICAL UNIVERSITY
B.A., LIAONING TECHNICAL UNIVERSITY
M.S., UNIVERSITY OF MASSACHUSETTS AMHERST
Ph.D., UNIVERSITY OF MASSACHUSETTS AMHERST

Directed by: Professor Carlton L. Ho

Mitigation and prevention of shale-formation damage caused by hydraulic-fracturing fluid/rock interactions play an important role in well-production stability and subsequent refracturing design. This study presents three experimental investigations on the interaction of water/shale, fluid/clay, and fluid/shale. A series of experiments were designed to investigate fluid/shale interactions: hydrophilic to hydrophobic alteration through chemical-vapor deposition, nanoindentation testing on shale sample, geotechnical laboratory experiments on contaminated clay, X-ray photoelectron spectroscopy (XPS), X-ray diffraction (XRD), and scanning electron microscope (SEM) on shale sample. A clay-matrix-based data-screening criterion is proposed for nanoindentation. The continuous-stiffness-measurment (CSM) method is proved to have better definition and characterization of softening of shale based on the proposed criterion. This study furthered the numerical model of clay deformation by Hattab and Chang (2015) by considering different pore fluid concentration. The fracturing fluid contaminated clay produced changes of geotechnical properties. Based on the proposed criterion and designed experiments, fracturing fluid contaminated shale was observed to

gain 4 to 6% of NaCl. However, all other minerals contents are found to decrease after the shale powder-fluid interaction. A characteristic depth was proposed to consider reduction of hardness and mineral content at the same time. Moreover, an empirical equation was proposed to describe fracture toughness of shale by using a selection of indentation depth, its corresponding hardness and Young's modulus.

TABLE OF CONTENTS

Page

LIST OF TABLES

Table Page

LIST OF FIGURES

Figure Page

LIST OF SYMBOLS AND ABBREVIATIONS

COGCC	Colorado Oil and Gas Conservation Commission
AER	Alberta Energy Regulator
MHF	Massive Hydraulic Fracturing
FE-SEM	Field-Emission Scanning Electron Microscopy
OGPW	Oil and Gas Production Wastewater
EC	Electrical Conductivity
EDL	Electrical-Double-Layer
BH	Brinell Hardness
DIC	Digital Image Correlation
$h_{\max}$	Maximum Indentation Depth
F_{max}	Maximum Load
CSM	Continuous Stiffness Measurement
$\dot{h}/h$	Indentation Strain Rate
t_{h}	Holding Time
$\dot{F}$	Loading Rate
t_L	Loading Time
L/U	Cycles of Loading and Unloading
$F_{P,i}$	Peak Load
ν_i	Poisson's Ratio of the Diamond Indenter
E_i	Elastic Modulus of the Diamond Indenter
E_r	Reduced Elastic Modulus of the Indentation Contact
A_c	Projected Contact Area at F_{max} and h_{max}
β	Constant Related to Geometry of the Indenter
S	Contact Stiffness
h_c	Contact Depth
ε	Constant Related to the Geometry of the Indenter
H	Hardness of Sample
K_c	Fracture Toughness

U_t	Total Energy
U_e	Elastic Energy
U_p	Plastic Energy
U_{pp}	Pure Plastic Energy
U_{frac}	Induced Fracture Energy
F_L	Loading Force
F_{UL}	Unloading Force
h_{creep}	Creep Displacement
h_r	Residual Displacement
h_{th}	Thermal Drift
h_f	Final Displacement
G_c	Strain Energy Release Rate
C_c	Compression Index
CL	Low Plasticity Clay
SM	Silty Sand
SP	Poorly Graded Sand
ML	Silt
GA	Glutaraldehyde
PEG	Polyethyleneglycol
PAM	Polyacrylamide
e_N	Normalization Void Ratio
N	Normalization Pressure
P	Consolidation Pressure
CEC	Cation Exchange Capacity
SSA	Specific Surface Area
T	Absolute Temperature
y_d	Scaled Midway Potential
ζ	Scaled Distance
y	Scaled Electrostatic Potential

ε	Dielectric Constant
c_0	Molar Concentration of the Ions in Bulk Solution
K_BT	Thermal Energy per Ion
y_0	Scaled Potential at the Clay Surface
G	Specific Gravity
e	Void Ratio
ρ_w	Density of Water
d	Midway Distance Between the Particles
ϕ	Electrostatic Potentials Values
CH	High Plasticity Clay
OTMS	Octadecyltrimethoxysilane
E	Young's Modulus
XRD	X-ray Diffraction
XPS	X-ray Photoelectron Spectroscopy
SEM	Scanning Electron Microscopy
PDMS	Polydimethylsiloxane
DMDCS	Dimethyldichlorosilane
IL	1-D Incremental Consolidation Test
DS	Direct Shear Test
R	Radius
l_c	Length Connecting Two Centers
ψ_R	Repulsive Potential
ψ_A	Attractive Potential
ψ	Resulting Potential
$\tilde{B}$	Constant of Surface Potential
$\tilde{A}$	Constant of Surface Potential
d_{min}	Minimum Distance Between Two Clusters
f	Inter-Cluster Force
$\tilde{A}_N$	$\tilde{A}$ Normalized by d_{min}

R_N	R Normalized by d_{min}
l_N	l_c Normalized by d_{min}
EOI	End of Increment Consolidation
EOP	End of Primary Consolidation
C_v	Coefficient of Consolidation
ASTM	American Society for Testing and Materials
RTS	Razor Tamped Surface
σ_y	Yield Strength of Material
ε_y	Strain at the Yield Point
a	Coefficient of Hardness
β	Constant
H_0	Hardness at An Infinite Depth
h^*	Characteristic Length

CHAPTER 1

INTRODUCTION AND SCOPE OF RESEARCH

1.1 Introduction

The oil and gas industry has successfully used the technique of hydraulic fracturing to extract oil and gas from low permeability formations. Unfortunately, this has resulted in numerous controversial incidents of water contamination (Llewellyn et al., 2015). In Colorado on 2014, 838 spills and releases of flowback and produced water were reported to Colorado Oil and Gas Conservation Commission (COGCC). In 2015, 153 releases of spills were reported to the Alberta Energy Regulator (AER) Compliance Dashboard including produced water, fracking fluid, or chemicals (McLaughlin et al., 2016).

Since 1948, Massive Hydraulic Fracturing (MHF) has been employed to increase gas production from low-permeability reservoir rocks (Ahmed et al., 1979). It is aggressively playing an important role. In the past decade, hydraulic fracturing has become more economically viable around the world. The Annual Energy Outlook 2015 with projections to 2040 reports that there was an increase of 35% in total dry natural gas production in the United States from 2005 to 2013. During the same period, the natural gas share of total United States energy consumption rose from 23% to 28% (U.S. Energy Information Administration, 2015). These reported increases are largely dependent upon the successful technique of hydraulic fracturing.

However, multiple issues remain regarding to environmental safety and engineering properties. Three phases of materials with which fracturing fluid could interact with, physicochemical influences of hydraulic fracturing fluid on shale, soil, and

water resources are increasingly of concern. Therefore, there will be a focus upon three primary phenomena related to the fracking fluid waste liquid: first, as hydraulic fracturing fluid was introduced into the fractured shale interface, the clay-rich sedimentary rock, shale interacts with aqueous liquids. The shale-fluid interactions were considered as a primary cause of shale softening and production reduction after a period. To prevent the shale formation damage by fracturing fluid-rock interactions, a deep understanding of fluid-shale interaction is needed; second, during production, the accidental contamination by spilled produced water or fracking fluid leave an environmental impact on the groundwater resources; third, due to the contamination of produced water, geotechnical properties of the contaminated soil have changed, which could have a detrimental impact on the soil mechanics or adjacent structures.

This research program focusses on the theoretically innovative methodologies combined with designed experiments to study some of the above challenges. A nanoindentation technique was proposed to investigate and characterize fluid-shale interactions. Polymer and monomer coatings are proposed to change the shale surficial characteristics. Clay/brine or clay/fluid interactions will also be investigated to explain the changes in geotechnical properties of produced water contaminated soil.

This dissertation presents detailed objectives and scope of work for the research, a review of literature relevant to fracturing fluids, description of test methodology, results of three designed research projects, and general conclusions and future work. This dissertation contains three papers that were produced during the course of the research project.

1.2 Objective and Scope of Research

The objective of this research is to perform an experimental investigation on shale and soil. Specifically, the following hypotheses are proposed and to be verified by designed experiments:

- "Shale surface can be altered from hydrophilicity to hydrophobicity using certain coatings" and "A clay-matrix-based criterion will be proposed to better screen all of the data via nanoindentation" to be characterized by designed control testing.
- "Shear behavior of high-plasticity clay contaminated by fracturing fluid is different from previous study using petroleum oil" to be testified and modeled numerically via a series of geotechnical experiments.
- "Fracturing fluid-shale interaction can be characterized based on proposed theories and experimental measurement" to be implemented by designed two-phase experiments.

CHAPTER 2

LITERATURE REVIEW

2.1 Introduction

This section presents a summary of the literature review. In order to highlight the significance of the proposed theories, a detailed thorough study was performed to determine the current state of the art and the practice in each area. The following sections include the previous literature for the following areas: composition of hydraulic fracturing fluids and produced water; possible fates of several specific hydraulic fracturing component; treatment of oil and gas production wastewater; fluid-shale interactions; nanoindentation study on shale and geotechnical properties of contaminated soil by hydraulic fracturing.

2.2 Hydraulic Fracturing Fluid and Produced Water

2.2.1 Hydraulic Fracturing Fluid

Hydraulic fracturing fluid is used for gas shale stimulations. The average composition for United States shale plays possesses approximately 99% of water with a variety of chemical additives. Vengosh et al. (2014) investigated the unconventional shale gas development and hydraulic fracturing in the United States. Four potential risks for water resources are pointed out: (1) the contamination of shallow aquifer with fugitive hydrocarbon gases (stray gas contamination); (2) the contamination of surface water and shallow groundwater from spills, leaks, and/or the disposal of inadequately treated shale gas wastewater; (3) the accumulation of toxic and radioactive elements in soil or stream sediments near disposal or spilled sites; and (4) the over-extraction of water resources

that may leads water shortage or conflicts with other water users, such as in water-scarce areas. It was also schematically illustrated in Figure 2.1 of possible modes of water impact associated with shale gas development.

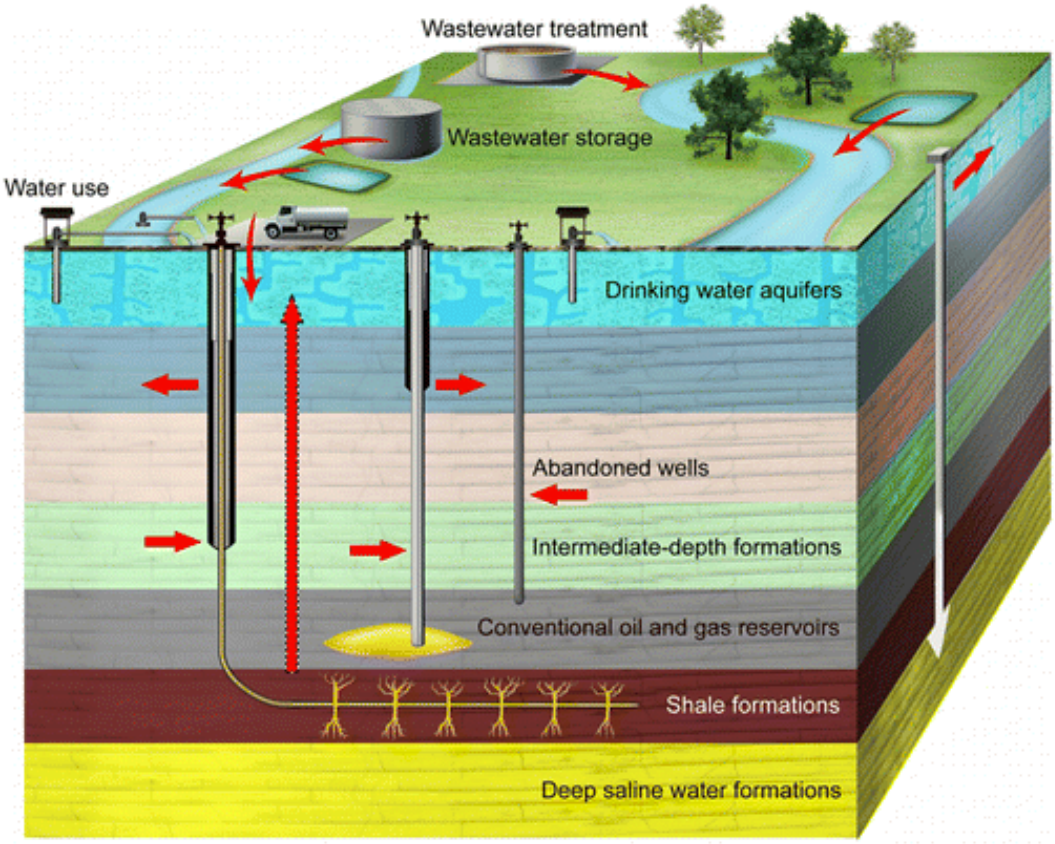

Figure 2.1 Schematic illustration of possible modes of water impacts associated with shale gas development (Vengosh et al., 2014).

In order for the public have better understanding and to address any vulnerabilities of drinking water resources to hydraulic fracturing activities, U.S. EPA (2015) published a detailed study about the potential impact on the drinking water resources. Figure 2.2 shows the stages of the hydraulic fracturing water cycle.

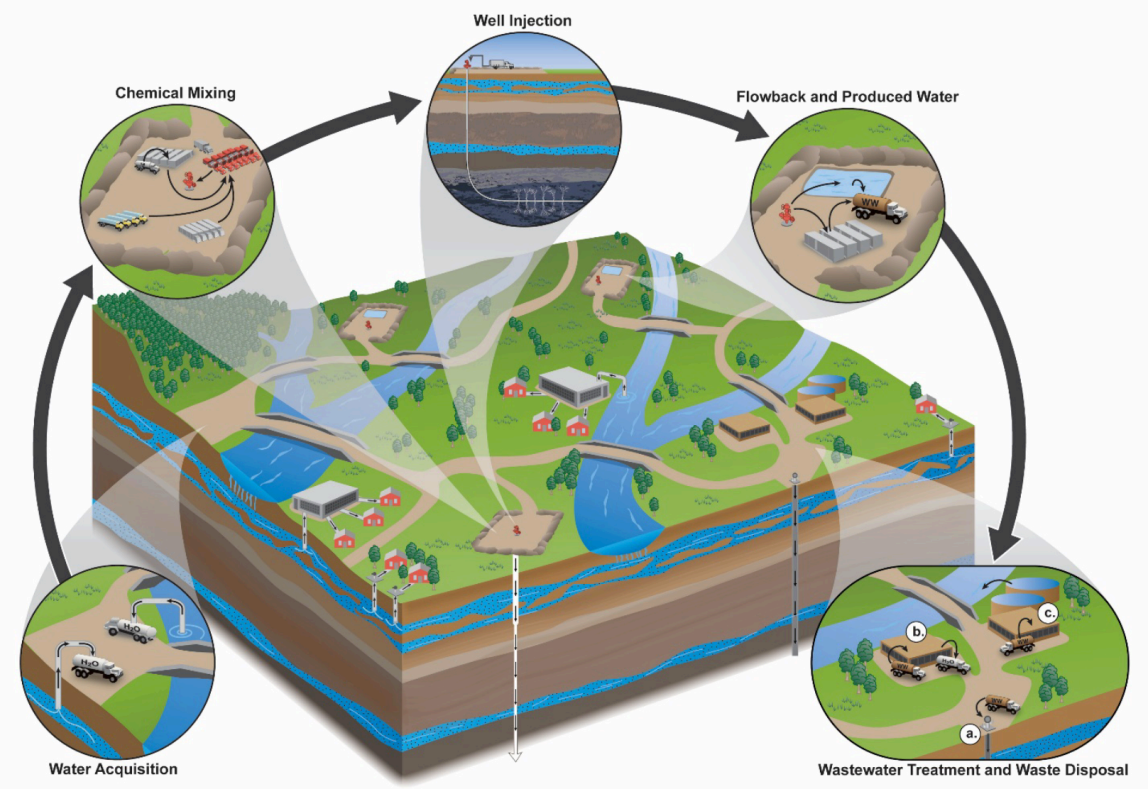

Figure 2.2 The stages of the hydraulic fracturing water cycle (U.S. EPA, 2015).

By the means of field-emission scanning electron microscopy (FE-SEM) to examine the micro-structure, Dieterich et al. (2016) investigated the interactions between the Marcellus shale and hydraulic fracturing fluid. The recipe of the synthetic fracturing fluid they used is detailed in Table 2.1. For the purpose of leaving shale surface unobscured for FE-SEM analysis, sulfate and barium were left out in that study.

Table 2.1 Synthetic hydraulic fracturing fluids recipe of Dieterich et al. (2016)

The synthetic fracturing fluid (pH of 5.7) was created with the above salts mixed in 2 L of ultrapure water to replicate the concentrations from recycled fracturing fluid collected in Greene County, PA. The final concentrations based on stoichiometric calculations are reported in the far right column of this table.

Component	Target conc. of comp. (mg/L)	Salt	Mass of salt added (g)	Atomic Mass of comp. (g/mol)	Molecular wt. of salt (g/mol)	Moles of salt	Moles of comp. added	Mass of comp. added (g)	Volume of solution (L)	Comp. conc. (mg/L)
Ca^{2+}	2100	$CaCl_2 * 2H_2O$	15.4028	40.08	147.02	0.1048	0.105	4.199	2	2100
Mg^{2+}	200	$MgCl_2 * 6H_2O$	3.3468	24.31	203.27	0.0165	0.016	0.400	2	200
K^+	160	KCl	0.6114	39.10	74.55	0.0082	0.008	0.321	2	160
Na^+	7260	NaCl	36.1755	22.90	58.44	0.6190	0.635	14.547	2	7273
Sr^{2+}	200	$SrCl_2 * 6H_2O$	1.2184	87.62	266.65	0.0046	0.005	0.400	2	200
Br^-	140	NaBr	0.3613	79.90	102.89	0.0035	0.004	0.281	2	140
HCO_3^-	260	$NaHCO_3$	0.7166	61.02	84.01	0.0085	0.009	0.520	2	260
Cl^-	–	–	–	35.45	–	–	0.879	31.154	2	15,577
SO_4^{2-}	100	Na_2SO_4	0.2965	96.06	142.04	0.0021	0.002	0.201	2	100
							Charge balance			TDS
							0.000			26,012
							pH	5.7		

Liu (2013) presented a comparison for fracturing fluid between field collected in a well site and the proposed synthetic recipe. For the synthetic recipe, the fracturing fluid component was collected and summarized from FracFocus, which is an information website launched by the Grand Water Protection Council and Interstate Oil and Gas Compact Commission since 2011 (117,600 well sites registered to date). Liu revealed that 13 components were most commonly used in those fluids: water, proppant, acid, iron control, corrosion inhibitor, friction reducer, clay stabilizer, gelling agent, biocide, cross linker, breaker, pH adjustor, and scale inhibitor. Based on the collected data, it was drawn as in Figure 2.3.

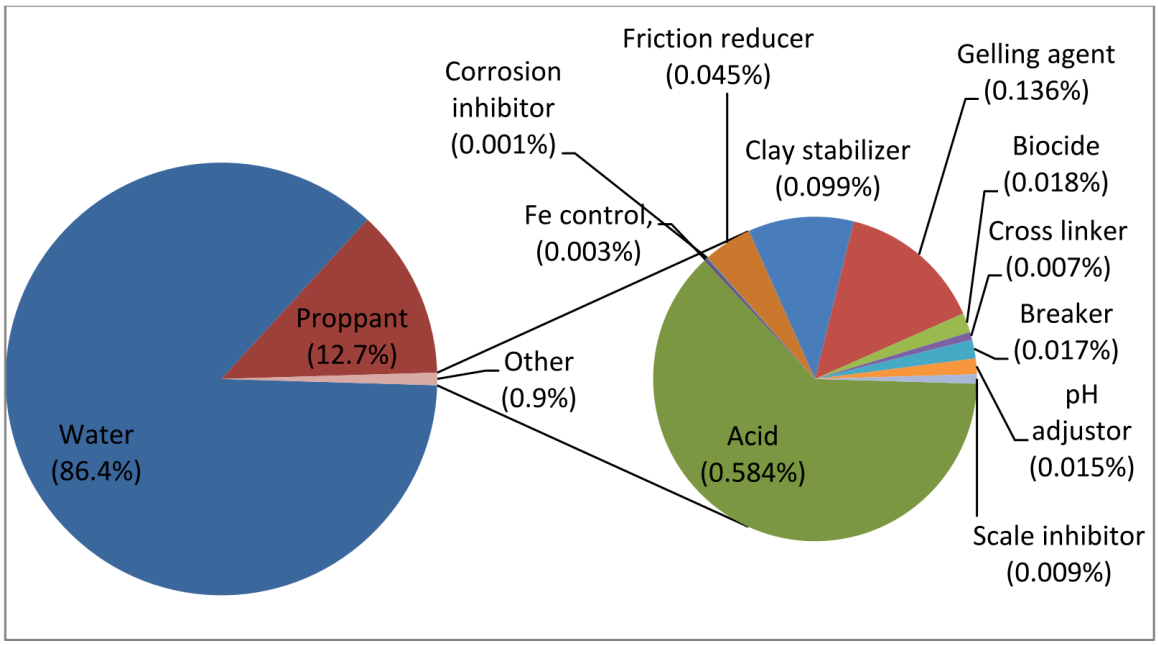

Figure 2.3 Average mass composition of hydraulic fracturing fluid based on FracFocus Data from Liu (2013)

Compared to three ranges of synthetic fracturing fluid, industry-supplied fracturing fluid investigated by Liu (2013) contained high concentrations of calcium, magnesium, sodium, barium, strontium and chloride due to the introduction of brine formation water and/or salts in the formation being fractured. Table 2.2 shows a comparison between industry-supplied and synthetic fracturing fluids, where the fracturing fluid sample were derived from three boreholes drilled from the same well pad, located in a Marcellus drilling operation in Carmichaels, Greene County, Pennsylvania. Liu (2013) also mentioned two main reasons causing difference of synthetic fluid from industry used fluids. Firstly, industry alters recipe under the circumstance of specific site and formation. Secondly, addition of fracking additives into waste water while recycling makes it difficult to replicate if recycled fluid is not accessible.

Table 2.2 Summary of water quality parameters for industry-supplied and synthetic fracturing fluid by Liu (2013)

Parameter	Industry-supplied fracking fluid	Synthetic fracking fluid (Low)	Synthetic fracking fluid (Average)	Synthetic fracking fluid (High)
Total dissolved carbon (TDC)	$463.4 \pm 92.0^{(1)\,(n)}$	$357.9 \pm 5.5^{(1)\,(n)}$	$748 \pm 16^{(2)\,(n)}$	$1685 \pm 105^{(3)\,(n)}$
Total dissolved organic carbon (TDOC)	$414 \pm 105^{(1)\,(n)}$	$345 \pm 15^{(1)\,(n)}$	$700 \pm 11^{(2)\,(n)}$	$1531 \pm 76^{(3)\,(n)}$
Total dissolved nitrogen (TDN)	$80.0 \pm 9.4^{(1)\,(n)}$	$42.9 \pm 0.6^{(2)\,(n)}$	$132.8 \pm 2.9^{(3)\,(n)}$	$550.9 \pm 9.2^{(4)\,(n)}$
Sulfate (SO_4^{2-})	$810.9 \pm 86.3^{(1)\,(n)}$	$79.3 \pm 3.2^{(2)\,(n)}$	$348 \pm 79^{(2)\,(n)}$	$1567 \pm 201^{(3)\,(n)}$
Phosphorus (P)	$6.5 \pm 3.8^{(1)\,(n)}$	$9.4 \pm 0.6^{(1)\,(n)}$	$8.9 \pm 1.1^{(1)\,(n)}$	$13.8 \pm 7.2^{(1)\,(n)}$
pH	$6.16 \pm 0.15^{(1)\,(n)}$	$1.92 \pm 0^{(2)}$	$1.48 \pm 0^{(2)}$	$1.37 \pm 0^{(2)\,(n)}$
Aluminum (Al)	N/A	$1.1 \pm 0^{(n)}$	$3.4 \pm 1.6^{(n)}$	$6.7 \pm 0^{(n)}$
Arsenic (As)	$0.9 \pm 0.2^{(1)\,(n)}$	$3.0 \pm 0.6^{(1)\,(n)}$	$1.8 \pm 0.6^{(1)\,(n)}$	$4.2 \pm 3.0^{(1)\,(n)}$
Calcium (Ca)	$2207 \pm 233^{(1)\,(n)}$	$81 \pm 0.5^{(2)\,(n)}$	$78 \pm 4.0^{(2)\,(n)}$	$93 \pm 47^{(2)}$
Iron (Fe)	$6.8 \pm 3.1^{(1)\,(n)}$	$1.6 \pm 0.5^{(1)\,(n)}$	$2.7 \pm 1.6^{(1)\,(n)}$	$2.1 \pm 0^{(1)}$
Potassium (K)	$141 \pm 21^{(1)\,(n)}$	$25.7 \pm 1.7^{(2)\,(n)}$	$113.6 \pm 9.7^{(1)\,(n)}$	$434.3 \pm 6.2^{(3)\,(n)}$
Magnesium (Mg)	$219 \pm 22^{(1)\,(n)}$	$4.3 \pm 0^{(2)}$	$6.5 \pm 3.3^{(2)}$	$18.4 \pm 5.4^{(2)\,(n)}$
Sodium (Na)	$6607 \pm 627^{(1)\,(n)}$	$27.9 \pm 1.1^{(2)\,(n)}$	$33.4 \pm 0^{(2)}$	$263 \pm 81^{(2)\,(n)}$
Sulfur (S)	$11.1 \pm 6.4^{(1)\,(n)}$	$45.6 \pm 0.0^{(2)\,(n)}$	$66.7 \pm 13.3^{(3)}$	$692.4 \pm 10.6^{(4)\,(n)}$
Silica (Si)	$17.48 \pm 3.89^{(1)\,(n)}$	$73.8 \pm 63.9^{(1)\,(n)}$	$90.3 \pm 52.9^{(1)\,(n)}$	$112.4 \pm 16.5^{(1)\,(n)}$
Uranium (U)	2.3 ± 0.62	N/A	N/A	N/A
Barium (Ba)	$306 \pm 43^{(1)\,(n)}$	$5.8 \pm 0.5^{(2)\,(n)}$	$5.3 \pm 0^{(2)}$	$5.8 \pm 2.6^{(2)\,(n)}$
Strontium (Sr)	$441 \pm 46^{(1)\,(n)}$	$6.8 \pm 0.5^{(2)\,(n)}$	$6.3 \pm 0^{(2)}$	$15.8 \pm 9.5^{(2)\,(n)}$
Chloride (Cl^-)	$15901 \pm 1252^{(1)\,(n)}$	$925 \pm 240^{(2)\,(n)}$	$1817 \pm 436^{(2)\,(n)}$	$4229 \pm 1320^{(3)\,(n)}$

Comparing for all pairs using Tukey-Kramer HSD method, alpha=0.01. Values represent the mean concentration plus standard deviation (or range) for the listed parameters in units of milligrams per liter (mg/L) except for pH. Means with similar numerical superscripts are not significantly different ($p>0.01$). "n" denotes this group of data is from the normal distribution. Data were analyzed using non-parametric Wilcoxon method if they were not from the normal distribution. Industry-supplied fluids totally had 6 replicates, while each synthetic fluid had 4 replicates.

2.2.2 Produced Water

Produced water is a mixture of injected water, formation water, hydraulic fracturing chemicals, and hydrocarbons (Pichtel, 2016). It has a complex composition but it could be broadly classified into organic and inorganic compounds, including dissolved and dispersed oil components, grease, heavy metals, radionuclides, hydraulic fracturing chemicals, dissolved formation minerals, salts, dissolved gases (including CO_2 and H_2S),

scale products, waxes, microorganisms, and dissolved oxygen. A generalized chemical composition of produced water appears in Table 2.3.

Table 2.3 Composition of oilfield produced water presented by Pichtel (2016)

Parameter	Range	Metal	Range (mg/L)
Density (kg/m^3)	1014–1140	Ca	13–29,222
Conductivity (μS/cm)	4200–58,600	Na	132–97,000
Surface tension (dyn/cm)	43–78	K	24–4,300
Turbidity (NTU)	182	Mg	8–6,000
pH	4.3–10	Fe	<0.1–100
TOC (mg/L)	0–1,500	Al	310–410
TDS	267,588	B	5–95
TSS (mg/L)	1.2–10,623	Ba	1.3–650
Dissolved oxygen (mg/L)	8.2	Cd	<0.005
Total oil (mg/L)	2–565	Cu	<0.02–1.5
Volatiles (BTEX; mg/L)	0.39–35	Cr	0.02–1.1
TPH (mg/L)	>20	Li	3–50
Chloride (mg/L)	80–200,000	Mn	<0.004–175
Bicarbonate (mg/L)	77–3,990	Pb	0.002–8.8
Sulfate (mg/L)	<2–1,650	Sr	0.02–2,204
Sulfite (mg/L)	10	Ti	
NH_3-N (mg/L)	10–300	Zn	<0.01–0.7
Phenol (mg/L)		As	0.01–35
Volatile fatty acids (mg/L)	0.009–23	Hg	<0.005–0.3
	2–4,900	Ag	<0.005–0.3
		Be	<0.001–0.15
		Ni	<0.001–0.004
			<0.001–1.7

2.3 Possible Fates of Several Specific Hydraulic Fracturing Component

McLaughlin (2016) researched the environmental fate of hydraulic fracturing fluid additives after spillage on agricultural topsoil. It is clearly to understand the spill can contaminate soil, groundwater, surface water, or get contact with nearby livestock or agriculture, all of which are vulnerable to effect environmental and human health. The following eleven components were summarized by Pichtel (2016) to describe the possible fates of fracturing fluid chemicals.

2.3.1 Gelling Agents

Guar and cellulose (Gellants) are nontoxic and readily biodegradable. For the compounds (acids and alcohols) used as gelling agents helps the microbiological growth.

2.3.2 Friction Reducers

Polyacrylamide is readily biodegradable. However, it may be formed into acrylamide via heating or exposure to ultraviolet radiation.

2.3.3 Cross-Linkers

Boron and amines used in cross-linkers have toxic effects and they could be transported or mobile in soil and groundwater.

2.3.4 Breakers

For the reason of environmentally benign, the utilization of enzymes is preferable than that of oxidizers. However, enzyme's mobility stays unknown.

2.3.5 Acids and Bases

Strong acids or bases are believed to render adverse effects on soil. Extremes in pH may dramatically change microbial composition.

2.3.6 Biocides

Some common used biocides are known to be volatile or sorb to soils and can persist in the environment, antecedent fates are mainly unknown.

2.3.7 Corrosion Inhibitors

In general, corrosion inhibitors are highly soluble and biodegradable. In this group, compounds are toxic and/or carcinogenic. Propargyl alcohol and thiourea ($SC(NH_2)_2$) are GHS Category 2 chemicals. They are among the most toxic chemicals used in the fracturing fluids. Propargyl alcohol is considered readily biodegradable, which is mobile in soil. Thiourea is considered biodegradable and highly mobile in soil. Volatilization of propargyl alcohol from soil ranges from 12.6 days to 13 days in an alkaline silt loam soil (pH 7.8, 3.25% organic carbon) and an acidic sandy loam (pH 4.8, 0.94% organic carbon), respectively.

2.3.8 Iron Control Agents

Among acetic acid, citric acid, sodium erythorbate, and mercaptoacetic acid (thioglycolic acid), most of them tend to be readily degraded and are not persistent. However, thioglycolic acid are the greatest concern for the reason of an oral LD_{50} value of 114 mg kg^{-1}.

2.3.9 Surfactants

Most of the surfactants are highly soluble in water and readily biodegradable.

2.3.10 Excess Salinity

Soil salinity imposes ion toxicity, nutrient (N, Ca, K, P, Fe, and Zn) deficiencies, nutritional imbalances, osmotic stress, and oxidative stress on plants. Salinity hinders seed germination, seedling growth, enzyme activity, DNA, RNA, and protein synthesis, and mitosis.

2.3.11 Hydrocarbons

Aromatic and phenol fractions of dissolved hydrocarbons are the primary hydrocarbons contributing acute toxicity in waste fracturing fluids.

2.4 Treatment of Oil and Gas Production Wastewater (OGPW) Contaminated Soil

The treatments for OGPW tend to be straight forward, which include (1) salt removal in the soil solution through leaching with irrigation or natural precipitation; (2) replacement of exchangeable Na^+ with Ca^{2+}; (3) clearance or elimination of hydrocarbons; and (4) removal or immobilization of metals.

2.4.1 Treatment of Salinity and Sodicity

Lloyd (1985) and Ahmad et al. (2012) concluded that the salt concentration of OGPW was the primary factor in estimating the waste loading rate in soil system. Utilization of inexpensive amendments if usually successful in treating soil salinity and sodicity problems. Both inorganic amendments (calcium amendments) and organic materials (animal manures) have proven to be effective. The most commonly used dry amendments are gypsum ($CaSO_4 \cdot 2H_20$) and calcium nitrate ($Ca(NO_3)_2$), although calcium chloride ($CaCl_2$) may be used if adequate drainage control is prepared and leachate is managed (Alberta Environment, 2001). Organic amendments must be mixed thoroughly into the affected soil, where a high-N fertilizer such as ammonium nitrate, ammonium sulfate, or calcium nitrate should be included (Alberta Environment, 2001).

Additional amendments may be beneficial in treating OGPW-affected soil. For example, polyacrylamide, is proved to successfully improve the physical properties of

Na-enriched soils (Sumner, 1993; Alberta Environment, 2001). To reduce soil biological activity, it was suggested to apply mycorrhizal fungi to the soil (Sharma et al., 2015).

Another technology to treat saline soil is electrokinetic remediation (Anderson, 2015), by allowing for separation and removal of Na^+, Cl^-, and other highly soluble ions (Pichtel, 2007).

When the electrical conductivity (EC) of the uppermost soil is greater than 35,000 uS/cm, it is suggested to remove or replace the contaminated soil rather than treatment considering economy efficiency (Anderson, 2015).

2.4.2 Treatment of Hydrocarbon Contamination

Given the relatively low concentration happened in OGPW, it is typically not expected to be significant for hydrocarbon contamination of OGPW-affected soil. However, as a catastrophic release happens, it still needs few techniques to make the treatment.

Bioremediation is one way to treat contaminated soil in situ. Aerated and nutrient-enriched water will be introduced into the contaminated zone through an array of injection wells, sprinklers, or trenches. Indigenous microbial communities and the contaminants are reacted with sufficient time, where the affected soil receive adequate nutrients (mainly N and P) to promote microbial growth and activity.

Another way is called slurry biodegradation. In this method, the contaminated soil is transferred to a lined lagoon and mixed with water. The soil slurry is continuously stirred and aerated, where the decomposition of the hydrocarbon is conducted via aerobic microbial processes.

Landfarming is another commonly used treatment for hydrocarbon-contaminated soil (Ward et al., 2003). It can be considered as a combination of biodegradation and soil venting, where the microbial oxidation reaction occurs in combination with volatilization.

Another field treatment needs high water application rates. Excavation and transference of contaminated soil is required, where a land treatment unit or cell is designed for controlling the process. The cell is usually graded at the base to provide for drainage and lined with clay and/or plastic to contain all runoff within the unit.

2.4.3 Treatment of Metals Contamination

Metals at OGPW-contaminated sites are usually in complex forms. Soil flushing technology can extract metals from soil via elutriation. The flushing solution is applied to the affect site (either the vadose zone or the saturated zone) via sprinklers or irrigations, or by subsurface injection. The applied reagent is allowed for sufficient period to percolate downward and react with contaminant metals. After that, the elutriate is then collected in prepared wells. The only drawback of this method is the possible production of residuals containing excess chelating agent, which is required to add when metals are minimally soluble in water. In addition, the leaching of soil may destroy the biological portion of soil.

For shallow depth contamination with metals, phytoremediation is a useful simple and common method. It is a cost-effective, low-technology process that green plants are used to extract, accumulate, and/or detoxify environmental contaminants. Phytoextraction is an application that utilize hyperaccumulating plants to take up metals from the contaminated soil and transport them into roots and aboveground shoots. In the following harvest, the metal-rich plant biomass can be ashed, and the residue can be processed as an

"ore" to recover the metals. This method works well in low permeability soil, where many other methods have a low success rate. Overall, phytoremediation can be a substitute for soil flushing.

2.5 Fluid-Shale Interactions

The effects of the interactions between shale and aqueous liquids can be reflected by the induced changes in shale properties, such as elasticity. Swelling and softening behavior have been studied for the exposure of clay shales (i.e., overconsolidated clays with well-developed diagenetic bonds) to water with various salinities (Wong 1998). Swelling occurs because of changes in pore-fluid chemistry or a decrease in confining pressure that falls below the swelling pressure. The Young's modulus was found to decrease with increasing swelling. It was also found that fluid/shale interactions depend primarily on the characteristics of interacting surfaces. Many researchers studied the surface characteristics of shales rich in clay minerals. Jaynes and Boyd (1991) investigated the nature of the siloxane surface in smectites by measuring the adsorption of aromatic hydrocarbons from water with organo-clays (clays with trimethylphenylammonium). They concluded that the strong hydration potential of exchangeable cations obscured the inherent hydrophobicity or hydrophilicity of the siloxane surfaces, and that a large part of the siloxane surface in smectites has a hydrophobic nature. In fact, a surface thermodynamics theory was proposed to quantitatively measure the magnitude of surface hydrophobicity or hydrophilicity (Van Oss and Giese 1995). In addition to the general agreement that the presence of clay minerals is the leading factor for shale-formation instability, Wilson and Wilson (2014)

summarized a series of other factors that are related to shale instability, including texture, structure, fabric, pore-size distribution, and the salinity of pore water in shales.

At present, volume expansion is considered the principal mode of shale instability, which is attributed to the interlayer swelling of Na-smectite (Wilson and Wilson 2014). Illitic and kaolinitic shales do not behave the same as those rich in smectite, where interlayer expansion in smectite is a dominant mechanism for shale instability. These authors also envisaged a mechanism for the failure of smectitic and illitic shales based on the electrical-double-layer (EDL) model. As shown in Fig. 2.4, the basal surfaces of clay minerals carry permanent negatively charges. As a dipole, water molecules are adsorbed to the negatively charged surfaces, forming the adsorbed water layer on the clay basal surface. Furthermore, a diffuse layer of hydrated cations also exists near the basal surface. The overlapping of the EDL associated with the charged basal surfaces of the clay minerals, which are exposed in opposite walls of micro- or mesosized pores in the shale, leads to an increase in pore/hydration pressure. As a result, the inhibiting effect of polymers on shale softening also can be explained by their coverage of the clay minerals' external surfaces so that the adsorbed cations are difficult to hydrate.

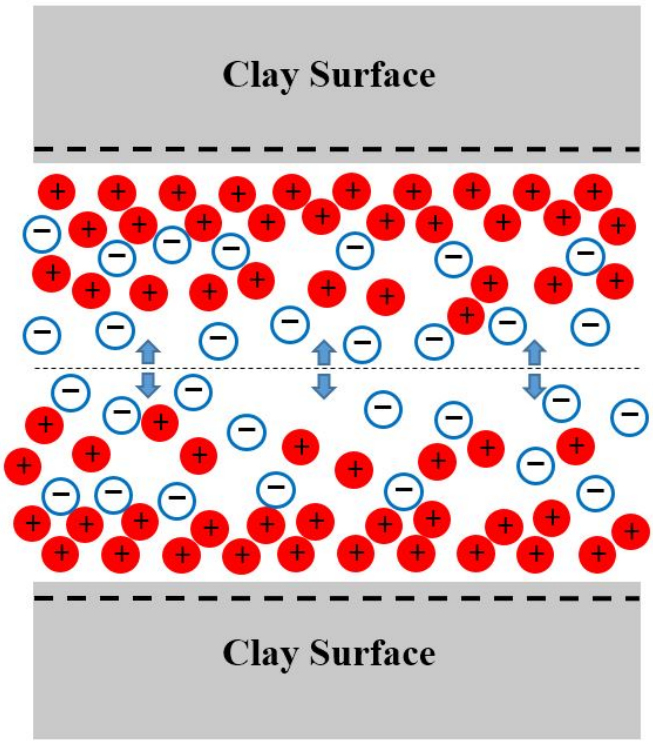

Figure 2.4 A simplified sketch of the electrical double layer (EDL) associated with the surface of clay minerals in shale pores indicating pressure generated by forced overlap of the EDL.

Fluid/shale interactions were characterized by the macroscale Brinell hardness (BH) by Lafollette and Carman (2010). They performed long-term proppant diagenesis tests with fracturing fluids, whereas the rock/fluid interactions were captured by the BH, which are time-dependent processes, implying that, after awhile, the damaged shale surface may cause proppant embedment. Lafollette and Carman (2013) investigated the effects of the fracturing fluid's compositional pH on shale by comparing pre- and post-immersion BH values of shale. They concluded that the fracture wall may be much softer in the early life of the well, and the finding has since brought much attention to shale/fluid interactions.

2.6 Nanoindentation Study on Shales

2.6.1 Introduction

As a sedimentary rock, shales usually contain a wide range of rock-forming minerals, including framework silicates, clay minerals, oxides and hydroxides, carbonates, sulfur minerals, organic materials, and other constituents (Potter et al., 1980). Different compositions and their varied mechanical properties of these minerals result in shales' heterogeneity in both microstructure and microscale mechanical properties. Of these constituents, fine-grained clay minerals form the clay matrix that usually dominates the overall mechanical behavior of the shale rock. Using digital image correlation techniques (DIC) on clayey rocks (e.g., shales), it was found that the clay matrix deforms much more than other mineral inclusions, and the deformation field is nonhomogeneous with a few areas nearly non-deformed (Bornert et al., 2010). It is understandable that the non-clay inclusions, only occupying a small volume fraction of the rock, cannot manifest the whole rock's mechanical behavior, but the clay matrix as a medium encapsulating the inclusions mainly controls the overall mechanical properties of shales.

2.6.2 Nanoindentation Study on Shale

Shale's resistance to fracturing plays an important role in the exploration, extraction, and recovery of oil and gas in unconventional reservoirs (e.g., shales). Performing nanoindentation testing on shale cuttings is a convenient way to characterize the rock's mechanical properties, since it eliminates the need for high quality core samples, which is costly and difficult or sometimes impractical. In fact, nanoindentation techniques have been used to study the mechanical properties of shales, mostly on high-

quality core samples (Ulm & Abousleiman, 2006; Ulm et al., 2007; Ulm et al., 2010; Bobko et al., 2011; Kumar et al., 2012; Deirieh et al., 2012; Shukla et al., 2013; Tran et al., 2014; Shukla et al., 2015; Bennett et al., 2015; Chen et al., 2015; Han et al., 2015; Liu, 2015). Shukla et al. (2015) believed that the nanoindentation results (i.e., Young's modulus) on shales are representative of the whole rock when the indention area is greater than the average grain size, which reaffirmed the viability of nanoindentation technique as an approach for obtaining mechanical properties from core fragments and drill cuttings.

For the development of prediction of field characterization and interpretation of nanoindentation results, Bobko et al. (2011) used an inverse micromechanics approach to estimate solid cohesive-frictional strength parameters of shales. It is aimed to translate the information about the porous clay composite and clay mineral into information about the local packing density associated with each indentation test.

2.6.3 Methods of Nanoindentation

Based on development of contact mechanics, nanoindentation experiments can be performed in a nanoindentation device to obtain the information of hardness, Young's modulus. For example, the Keysight G200 nano indenter has a load resolution of 50 nN and a displacement resolution of 0.01 nm. The displacement range is 1.5 mm and the maximum load is 500 mN. A diamond Berkovich indenter was usually used, with a tip radius of less than 20 nm. The tests will run with an allowed thermal drift rate, such as 0.05 nm/s. The maximum indentation depth ($h_{\max}$) and/or maximum load (F_{max}) can be entered in the controlling computer. The ISO standard 14577, Continuous Stiffness

Measurement (CSM) method, load control standard method, and the modified repeated loading method can be adopted accordingly.

For CSM method, a constant target indentation strain rate ($\dot{h}/h$) is given, such as 0.05 s^{-1}, where h is indentation depth. The CSM method superimposed a displacement-controlled harmonic loading with a frequency of 75 Hz and amplitude of 1.0 nm. As is pointed out by Yin and Zhang (2011), a five-step loading procedure was followed (Figure 2.5), including: (1) increase load at a constant strain rate ($\dot{h}/h$) of 0.05 s^{-1} to 4 μm; (2) hold the maximum load (F_{max}) constant for a given holding time (t_h) of 10 s; (3) decrease load under load control mode to 10% of F_{max} using the same loading rate ($\dot{F}$) used to achieve F_{max}; (4) hold the load (10% of F_{max}) for 100 s to record the thermal drift for correction; and (5) decrease load linearly to zero.

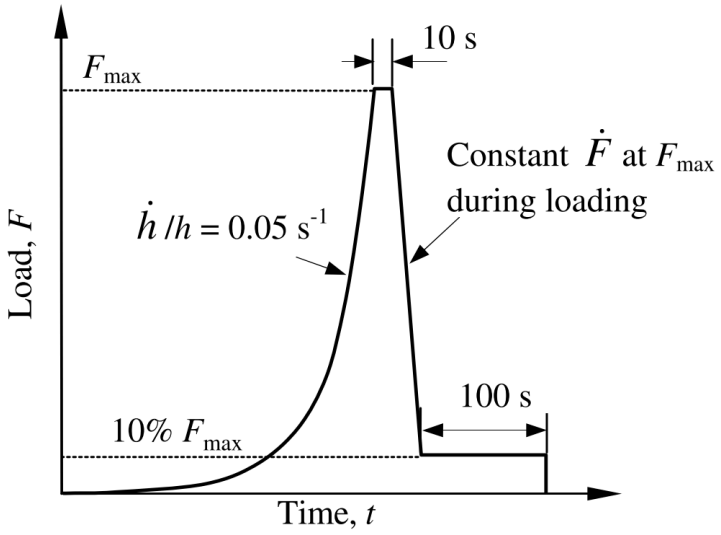

Figure 2.5 The CSM loading and unloading profile used as a monotonic loading test (Yin and Zhang, 2011)

The load control standard method applies indentation load at a constant loading rate. The maximum load (F_{max}) and loading time (t_L) were preset per different research plan. It took multiple cycles of loading and unloading (L/U) to reach the F_{max}. For the i-th

cycle (where i =1, 2,…,5), the peak load $F_{P,i}$ and loading rate to peak loading $\dot{F}_i$ are given by

$$F_{P,i} = F_{max}\frac{2^i}{2^N} \quad \text{Eq. (2.1)}$$

$$\dot{F}_i = \frac{F_{P,i}}{t_L} = \frac{F_{max}}{t_L}\frac{2^i}{2^N} \quad \text{Eq. (2.2)}$$

where N = total number of L/U cycles. Noted, the unloading rate was kept the same as that of loading section of that same cycle, and the load was reduced to the 90% of the peak load of that cycle. A holding time (t_h) was allowed at peak load in all L/U cycles. At the end of designed cycles, a holding time of 100 s could be allowed for thermal drift correction.

As a special case of the load control standard method, repeated loading made three modifications, including keeping the peak load of each cycle the same as the F_{max}, reducing the holding time to zero at all peak loads, and altering the percentage of unloading from 90% in the load control standard method to 100% in the repeated loading method. All other parameters remained the same. The loading profiles of these two methods are shown in Figure 2.6.

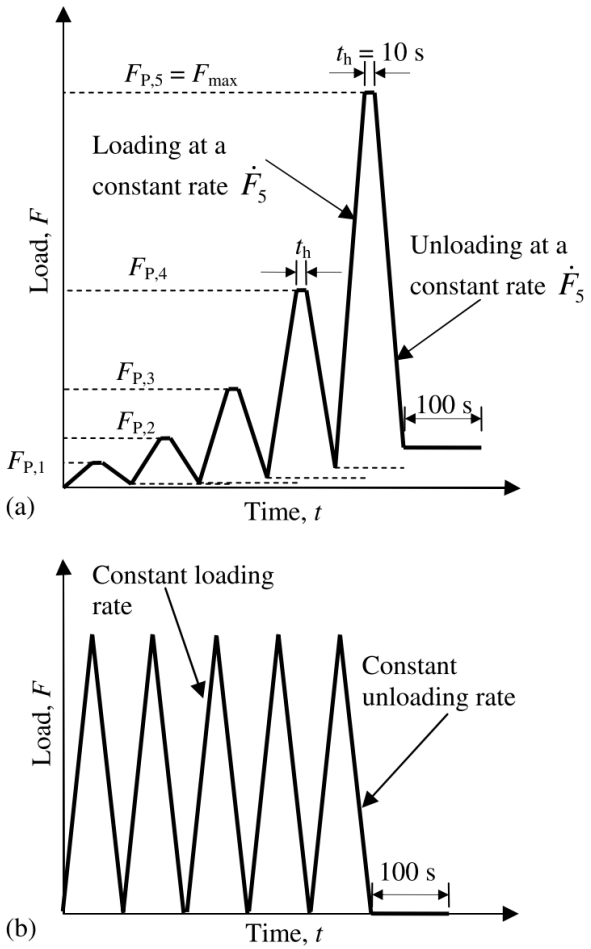

Figure 2.6 Loading profile for (a) Load control standard method and (b)modified repeated loading method from the load control standard method (Yin and Zhang, 2011)

The nanoindentation tests were performed in grid patterns and via manual selection of individual indenting locations if certain surface fracture and individual particle need to be avoided. The schematic diagrams shown in Figure 2.7 represent the behavior during loading and unloading.

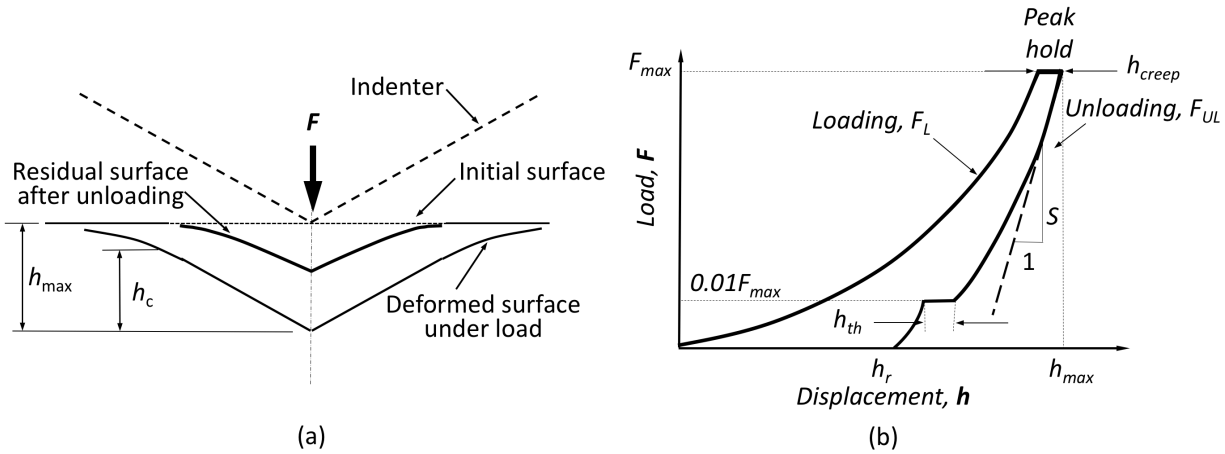

Figure 2.7 Nanoindentation schematic diagrams: (a) loading and unloading, and (b) corresponding load-dsplacement curve

The Young's modulus E is calculated using the following expression,

$$E = \frac{1-\upsilon_s^2}{\frac{1}{E_r}-\frac{1-\upsilon_i^2}{E_i}} \quad \text{Eq. (2.3)}$$

where ν_s is the Poisson's ratio of the test sample and is assumed to be $\nu_s = 0.18$; ν_i is the Poisson's ratio of the diamond indenter ($\nu_i = 0.07$); E_i is the elastic modulus of the diamond indenter ($E_i = 1140$ GPa); E_r is the reduced elastic modulus of the indentation contact, which can be calculated as follows,

$$E_r = \frac{1}{2\beta}\sqrt{\frac{\pi}{A_c}}S \quad \text{Eq. (2.4)}$$

where A_c is the projected contact area at F_{max} and h_{max} (Figure 2.7(b)); β is a constant related to geometry of the indenter, taken as 1.05; S is the contact stiffness obtained from the slope of the initial unloading curve at the maximum indentation h_{max} (Figure 2.7(b)) (Oliver and Pharr, 1992),

$$S = \frac{dF}{dh}|_{h=h_{max}} \quad \text{Eq. (2.5)}$$

The contact depth h_c can be calculated as

$$h_c = h_{max} - \varepsilon \frac{F_{max}}{S} \quad \text{Eq. (2.6)}$$

where ε is a constant related to the geometry of the indenter (ε= 0.75); the hardness of sample, H, can be expressed as

$$H = \frac{F_{max}}{A_c} \quad \text{Eq. (2.7)}$$

where A_c is also the projected contact area at F_{max} and h_{max}.

Fracture toughness, K_c, can be calculated by using the energy method (Cheng et al., 2002). During the process of loading and unloading of the indentation, the total energy, U_t, consists of two components: elastic energy, U_e, and plastic energy, U_p. Plastic energy, U_p, is irreversible work produced in the system, which is composed of pure plastic energy, U_{pp}, and the induced fracture energy, U_{frac}. Their relations can be expressed as

$$U_t = U_e + U_p = U_e + U_{pp} + U_{frac} \quad \text{Eq. (2.8)}$$

where the total energy, U_t, and elastic energy, U_e, can be calculated per the nanoindentation load-displacement curve ((Figure 2.7(b)) as

$$U_t = \int_0^{h_{max}-h_{creep}} F_L dh \quad \text{Eq. (2.9)}$$

$$U_e = \int_{h_r}^{h_{max}} F_{UL} dh - 0.01 F_{max} \times h_{th} \quad \text{Eq. (2.10)}$$

where F_L is loading; F_{UL} is unloading; h_{creep} is the creep displacement made by maximum constant load, F_{max}; h_r is the residual displacement; h_{th} is the thermal drift measured by system. Pure plastic energy, U_{pp} can be calculated by

$$U_{pp} = \left\{ 1 - \left[\frac{1 - 3\left(\frac{h_f}{h_{max}}\right)^2 + 2\left(\frac{h_f}{h_{max}}\right)^3}{1 - \left(\frac{h_f}{h_{max}}\right)^2} \right] \right\} \times U_t \quad \text{Eq. (2.11)}$$

where the final displacement, $h_f = h_r - h_{th} - h_{creep}$, can be obtained. Then the fracture energy, U_{frac}, can be determined from

$$U_{frac} = U_p - U_{pp} \quad \text{Eq. (2.12)}$$

The definition of strain energy release rate, G_c, is the energy dissipated during fracture per created fracture surface area. It can be obtained by dividing the projected contact area, A_c, by the expression of

$$A_c = 24.5h_c^2 \quad \text{Eq. (2.13)}$$

$$G_c = \frac{\partial U_{frac}}{\partial A_c} = \frac{U_{frac}}{A_c} \quad \text{Eq. (2.14)}$$

The fracture toughness, K_c, can then be calculated as the square root of strain energy release rate, G_c, multiplied by the reduced elastic modulus, E_r, by the expression of

$$K_c = \sqrt{G_c E_r} \quad \text{Eq. (2.15)}$$

2.7 Geotechnical Properties of Contaminated Soil by Hydraulic Fracturing Fluid/Produced Water

2.7.1 Studies of Geotechnical Properties on Oil-Contaminated Soil

Many researchers studied the effect on geotechnical properties by leakage gas oil on soils. However, the contamination caused by fracturing fluids (chemicals) was omitted. All the water held to clay particles by force of attraction is known as double-layer water. The innermost layer of double-layer water is known as adsorbed water, which is held strongly by clay. The adsorbed water is more viscous than free water. As is shown in Figure 2.8. This orientation of water around the clay particles gives clay soils their plastic properties (Das, 1997).

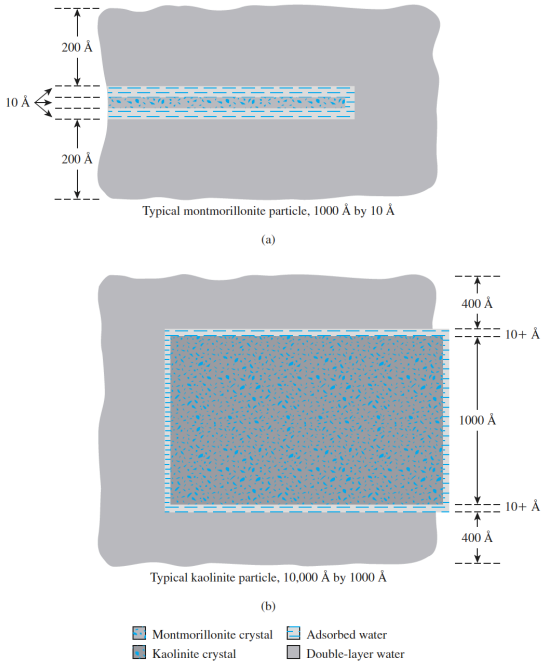

Figure 2.8 Clay water (Das, 2013)

Moore and Mitchell (1974) hypothesized that the inter-particle attraction increases as the strength of soil enhanced, and it was concluded that the effect of electrostatic force is to decrease the attraction at higher values of dielectric constant. Barbour and Yang (1993) investigated the clay-brine interactions (brine contamination) on the geotechnical properties of two Ca-montmorillonite clayey soils of glacial origin from western Canada (Indian Head till and Regina clay). The change in concentration of pore fluid to the levels of a concentrated brine can leads large alterations in the geotechnical properties of the soil. Meegoda and Rajapakse (1993) studied the changes in hydraulic conductivity of saturated clays due to short-term and long-term exposure of organic chemicals to clays. It was found that short-term permeability tests showed a change in hydraulic conductivity values but not the intrinsic permeability, yet the simulated long-term exposure leads showed an increase in the intrinsic permeability of soils.

Meegoda and Ratnaweera (1994) studied the factors that control the compressibility of contaminated fine-grained soil. It was concluded that the type and the number of chemicals in pore fluids as well as pore fluid viscosity can influence the compressibility of contaminated soil. Al-Sanad et al. (1995) investigated the oil-contaminated Kuwaiti sands using traditional geotechnical testing programs. The results indicated that a small reduction in strength and permeability and an increase in a compressibility due to oil contamination. Al-Sanad and Ismael (1997) furthered the study regarding to the aging effect. It was found that strength and stiffness of contaminated sand will be increased due to aging and a reduction of the oil content due to evaporation of volatile compounds. The compressibility and permanent deformation of oil-contaminated sand increase as the temperature increases beyond room temperatures (Aiban, 1998). Puri (2000) investigate the geotechnical properties of oil-contaminated sand. It was found that the compaction characteristics are generally similar for using water and crude oil. Shear strength parameters of sand are adversely affected by the oil contamination. Shin and Das (2001) studied the effect of three types of oil contamination (Oman crude oil, engine oil, lamp oil) on reducing the bearing capacity of a surface strip foundation. Ratnaweera and Meegoda (2006) performed unconfined compression tests on fine-grained soils contaminated with various amounts of chemicals include glycerol, propanol, and acetone. For granular soil, it showed a similar behavior, yet the mechanical interactions at particle contacts attributed to the system and it is caused by the lubrication by the viscous pore fluids. For fine-grained soil, the decrease in shear strength can be

explained by the physicochemical effects caused by a reduction in dielectric constant and mechanical interactions caused by high pore fluid viscosities.

The compressibility (the compression index, C_c) of cohesive soils with diesel oil pollution can be estimated from the established compression index of "clean" soil and dielectric constant of the porous medium of polluted soil (Olchawa and Kumor, 2007). Khamehchiyan et al. (2007) performed a series of geotechnical testing on oil-contaminated clayey and sandy soil (CL, SM and SP). Atterberg limits decrease with increasing oil contamination in CL soil, which is due to the nature of water in the clay minerals' structure and performance of existing non-polar and viscous fluids in soil. Olgun and Yildiz (2010) examined the effect of different pore fluid distribution on the geotechnical behavior of clays. It revealed that liquid limit values and consolidation parameters generally decreased while shear strength values increased with increasing organic fluid/water ratio and decreasing dielectric constant of the pore fluid. For oil-contaminated weathered basaltic rock (grades V and VI), Rahman et al. (2010) concluded that the addition of oil has adverse effects to the geotechnical properties of the residual soil. Jia et al. (2011) investigated the influence of crude oil contamination on the geotechnical properties of coastal sediments. It revealed that the more heavily polluted soil has a higher clay particle content, Atterberg limits, and compression coefficient. The over consolidated clay was studied for its geotechnical properties under oil contamination. The contamination of the clay entailed substantial microstructural changes: relatively loose packing of clay particles and their detachment from grain surface. The Atterberg limits are reduced for the first 3 months of contamination and reached constant limits. Whereas. the coefficient of permeability, compression and

swelling indexes increased in 3 and 6 months, respectively. The oil contamination has minor effect on over-consolidated ratio (Nazir, 2011). In order to promote the understanding of the influence of petroleum-derived contaminants on the geotechnical properties of soils, Khosravi et al. (2013) investigated geotechnical laboratory tests on clean and contaminated kaolinite specimen at the same relative compactions. Results show an increase of cohesion and a decrease of both the friction angle and compressibility with increasing gas oil content. As is shown in Figure 2.9. B and D show that more voids and spaces are available in the specimen mixed only with water, which result in larger settlement and higher compression indices.

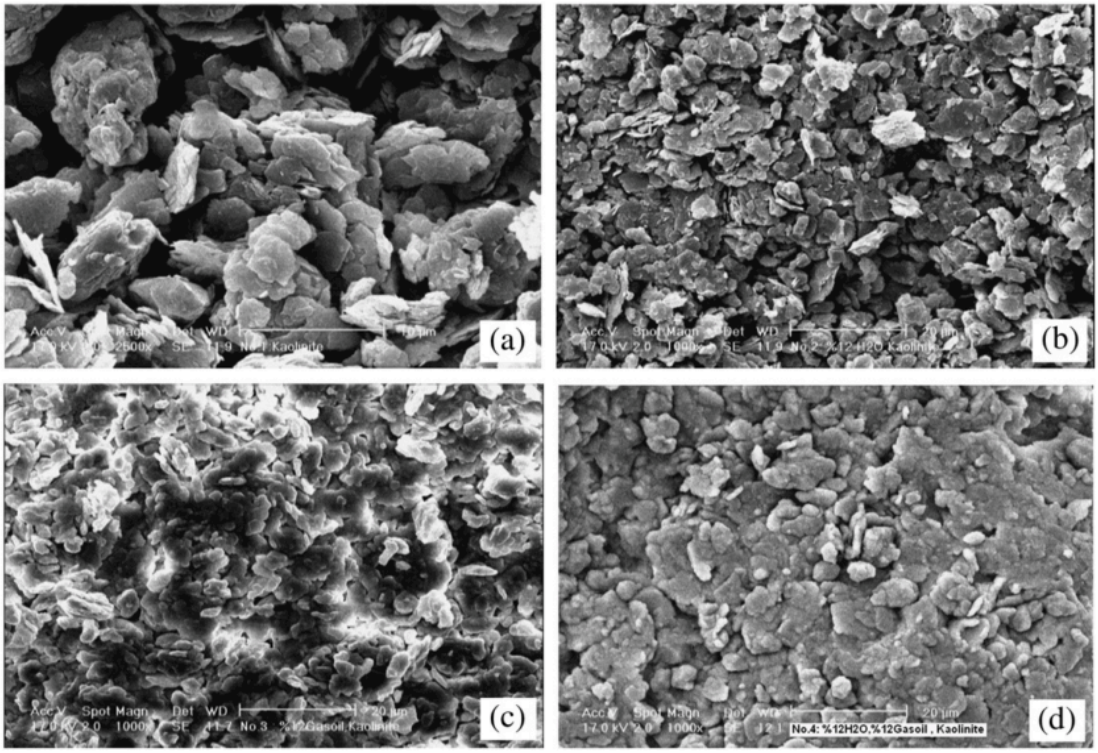

Figure 2.9 SEM images of a) clean kaolinite, b) kaolinite + 12% water, c) kaolinite + 12% gas oil, d)kaolinite + 12%water + 12% gas oil (Khosrvavi et al., 2013)

Nasehi et al. (2016) investigated the effect of gas oil contamination on the geotechnical properties of three categories of soils: poorly graded sand (SP), low

plasticity clay and silt (CL, ML). A decrease friction angle and an increase for cohesion of the soils were found with the increase of gas oil content ranging from 3% to 9%. The field emission scanning electron microscopy study stated that the increase content of clay particles will extends the rates of fabric flocculation, which is a key factor for increasing the unconfined compression strength in clayey soil. It verified the statement that flocculated soil possess a higher strength, lower compressibility and higher permeability than the same soil at dispersed state at the same void ratio (Lambe and Whitman, 1969).

2.7.2 Soil Contamination with Hydraulic Fracturing Drilling Fluid/Production Water

In order to treat the fracturing fluid-contaminated soil, Wolf et al. (2015) investigated multiple soil amendments on the growth of Bermuda grass as a revegetation method. Addition of inorganic fertilizer, broiler litter, and Milorganite® had 290%, 241%, and 172% greater shoot biomass than untreated contaminated soil, respectively. Al-Haddabi and Ahmed (2007) concluded that the application of treated-oily water even for a short duration on soil has an adverse effect on physicochemical properties. The results suggest that neither water application rates, nor depth of their interaction have significant effects on the soil salinity. No relationship was found between soil salinity and the water application. McLaughlin et al. (2016) highlighted the findings that it is necessary to consider co-contaminant effects when evaluating the risk of fracturing fluid additives and the produced water constituents, as to understand the impacts on human health, possibility for crop uptake, and potential for ground water contamination. Even though field fracturing fluid/produced water was not investigated in the research, simulated spills of HF fluid additives were studied, namely, the biocide glutaraldehyde (GA), poly

(ethylene glycol) (PEG) surfactants, and a polyacrylamide (PAM) based commercial friction reducer. Sang et al. (2014) researched on the flow-back fluids to remove colloids from sand grains and revealed that the land application of flow-back fluids can contaminate groundwater resources in two possible ways: intrinsic chemical constituents of the flow-back fluids and mobilization of colloid-associated soil contamination. By comparing the incidence rates of cement and casing failures in unconventional wells are 6 times higher than that in conventionally operated wells in Pennsylvania, the conclusion was drawn that surface water contamination increased structural failure rates of unconventional wells (Ingraffea et al., 2014; Mrdjen and Lee, 2016).

2.7.3 Prediction Model for e-log p Curve of Consolidation by the Theory of Diffuse Double Layer

Bharat and Sridharan (2015) developed a linear relationship between e/e_N *vs.* $1/\sqrt{P}$ (e_N is the normalization void ratio at normalization pressure N and P is the consolidation pressure) using diffuse double-layer theory. The study followed the theoretical equations describing the inter-relationships between void ratio and consolidation pressure for different clay-water-electrolyte interactions. The equations were proposed by Sridharan and Jayadeva (1982). The equations are shown as below.

$$P = 2c_0RT(\cosh y_d - 1) \quad \text{Eq. (2.16)}$$

$$\left(\frac{dy}{d\xi}\right)_{x=0} = -\frac{CEC}{SSA}\left(\frac{2513.6}{\sqrt{\epsilon c_0 T}}\right) \quad \text{Eq. (2.17)}$$

$$\left(\frac{dy}{d\xi}\right)_{x=0} = -(2\cosh(y_0) - 2\cosh(y_d))^{\frac{1}{2}} \quad \text{Eq. (2.18)}$$

$$\kappa d = -\int_{y_0}^{y_d}(2\cosh(y_0) - 2\cosh(y_d))^{-\frac{1}{2}}\,dy \quad \text{Eq. (2.19)}$$

$$e = G\rho_w SSAd \quad \text{Eq. (2.20)}$$

$$y_d = \operatorname{arccosh}(1 + \frac{P}{2c_0RT}) \quad \text{Eq. (2.21)}$$

$$y_0 = \operatorname{arccosh}(0.5\left\{\left[(\frac{dy}{d\xi})_{x=0}\right]^2 + 2\cosh\,(y_d)\right\}) \quad \text{Eq. (2.22)}$$

$$\kappa = \sqrt{\frac{8\pi e'^2 \nu^2 c_0}{\varepsilon K_B T}} \quad \text{Eq. (2.23)}$$

where:

CEC = cation exchange capacity (meq / 100 g)

SSA = specific surface area of the clay (m^2/g)

P = consolidation pressure (kPa)

T = absolute temperature

y_d = scaled midway potential

ζ = scaled distance (κx)

y = scaled electrostatic potential at any distance, x, from the surface of a single clay platelet

ε = dielectric constant

c_0 = molar concentration of the ions in bulk solution (M)

K_BT = thermal energy per ion (joules)

y_0 = scaled potential at the clay surface

G = specific gravity of the soil particles

e = void ratio

ρ_w = density of water (kg/m^3)

d = midway distance between the particles

ϕ = electrostatic potentials values

2.8 Summary

A review of literature has shown that fluid-shale interaction has significant effects on mechanical properties of shales. Nanoindentation method is widely adopted in the study of micro-mechanical properties of shale when soften by fracturing fluid. However, most current studies either focus single grain of shale or the bulk properties. No previous literature considers certain components or matrix in shale by excluding non-dominant minerals. In addition, the review reveals that there is no simple and reasonable data-processing method in nanoindentation especially for geomechanics studies.

The correlation between oil-contamination content and geotechnical properties of different types of soil from past literature was widely researched. However, the effect of different concentration of industry-supplied fracturing fluid on high plasticity clay (CH) is unknown and lacking.

In accordance with the existing studies on shales and soils by oil and gas production wastewater (OGPW), a comprehensive experimental investigation is needed on shale and soil by industry-supplied OGPW. It also helps to further the understanding of mechanical properties on the adjacent site near the oil-gas well from the manmade or inartificial accident of fracturing fluid spill.

CHAPTER 3

MICROMECHANICAL CHARACTERIZATION OF FLUID/SHALE INTERACTION BY MEANS OF NANOINDENTATION1

3.1 Abstract

Mitigation and prevention of shale-formation damage caused by hydraulic-fracturing fluid/rock interactions play an important role in well-production stability and subsequent refracturing design. In this paper, the effect of converting typically hydrophilic fractured surfaces to hydrophobic ones on fluid-induced softening of shales was investigated. Specifically, nanoindentation was used to characterize changes in the mechanical properties of shale samples after different surface treatments. A thin layer of octadecyltrimethoxysilane (OTMS) coating was deposited on the initially hydrophilic surface of shale, followed by inundation in water for certain periods of time to allow for fluid/rock interactions. Nanoindentation testing was then conducted on the treated shales to characterize their hardness, Young's modulus, and fracture toughness to examine the alteration of shale's mechanical properties caused by fluid/rock interactions and to check whether hydrophobic coating can mitigate shale-softening. Results from nanoindentation testing were analyzed by a newly proposed clay-matrix criterion for data screening. Different rock-surface treatments lead to changes in rock properties. Both the hardness

[1] Yang, Z., Wang, L., Chen, Z., Xiang, D., Hou, D., Ho, C. L., & Zhang, G. (2018). Micromechanical Characterization of Fluid/Shale Interactions by Means of Nanoindentation. *SPE Reservoir Evaluation & Engineering*, Preprint (Preprint). https://doi.org/10.2118/181833-PA.

and Young's modulus of the treated samples converge and stabilize at relatively large depths. Samples with hydrophobic surfaces exhibit a much lower degree of softening, as reflected by their better mechanical properties (e.g., 40% increase in hardness, 25% increase in Young's modulus, and 35% increase in fracture toughness), compared with untreated shale samples. The results of this study also demonstrate that the continuous-stiffness-measurement (CSM) method and the repeated loading method for nanoindentation loading yield similar ranges of micromechanical properties of the bulk shale. However, the CSM method, if combined with the newly proposed clay-matrix-based criterion for data screening can better define and characterize fluid/shale interactions or softening of shales.

3.2 Introduction

Hydraulic fracturing has been extensively used to increase gas production from low-permeability reservoir rocks since its first success in 1948 (Ahmed et al. 1979). Recently, several years of industry downturn have led to the search for the more-innovative and -economical techniques to improve the hydraulic-fracturing operation and to further reduce its costs. During hydraulic-fracturing operation, water-based fracturing fluids can cause some negative impacts on the surface of the created fractures within the shale formation, rendering damage to the fracture network (Akrad et al. 2011). In fact, the instability of wellbore and embedment of proppants into the weakened rocks are serious concerns induced by fluid/shale interactions. The changes in the mechanical properties such as Young's modulus and hardness of the rock indicate how shale swelling or softening develops resulting from exposure to aqueous fracturing fluids. Acoustic

logs with enhanced resolutions are widely used for quantifying mechanical properties of the formation at relatively large scales (Huang et al. 2015; Huang and Torres-Verdı´n 2016). However, characterization of fluid/rock interactions remains a challenging task, especially for a short period of time when the fluid-induced softening has just migrated into a very shallow depth, whereas acoustic logs provide bulk properties averaged from both the intact and weakened parts of the rock. This study investigates whether hydrophobic alteration to the fracture surface of shales can mitigate or even prevent fluid-induced damage or softening of shales. A clay-matrix criterion is newly proposed to screen and analyze indentation data, which can improve the accuracy of the results.

3.2.1 Nanohardness and Mohs Hardness

Hangen (2001) studied nanohardness and scratch resistance on the reference minerals used in the Mohs-hardness scale. For the nanoindentation experiments, a Berkovich-geometry indenter was used. Fig. 3.1 shows the relationship between the nanohardness and penetration depth at the nanoscale. All minerals show the same order with the Mohs scale except fluorspar, which might be caused by the size effect and/or surface roughness. Although the only clay mineral (talc) on the Mohs-hardness scale was not studied, the nanohardness of clay minerals tested in other studies falls in the range of approximately zero to 2 GPa. The nanoindentation results for hardness of muscovite are approximately 2 GPa at the depth of 2000 nm (Pant et al. 2013). Clay-rich Opalinus shale was also measured to have a hardness of 2 GPa at the depth of 3000 nm (Liu 2015).

Broz et al. (2006) conducted microindentation and nanoindentation on nine of the reference minerals on the Mohs scale with a Vickers (four-sided pyramid) diamond tip and a Berkovich (three-sided pyramid) diamond tip, respectively. Talc has a

microhardness of 0.14 ± 0.03 GPa, a nanoindentation hardness of 0.3 ± 0.18 GPa, and a nanoindentation modulus of 16.2 ± 6.6 GPa. The hardness of gypsum is slightly higher than that of talc, rendering a microhardness of 0.61 ± 0.15 GPa, a nanoindentation hardness of 1.03 ± 0.13 GPa, and a nanoindentation modulus of 25.3 ± 1.9 GPa. It was observed that the nanohardness values are, in general, greater than the microhardness ones. It was mentioned that the calculation of contact area is more sensitive to imperfections in the probe shape for nanoindentation; other sources of uncertainty in nanoindentation include determination of minimum detectable load, the calculation of contact stiffness from unloading, unknown magnitude of material pile-up around the indenter tip, and other factors of the measuring system and environment (Menčik and Swain 1995).

In this paper, a clay-matrix-based criterion is proposed and recommended to analyze the nanohardness and nanomodulus data. A clay matrix is defined as the bulk assemblage of mainly clay minerals with interparticle cementation and pores, as well as possibly some pore fluids. The integrated clay minerals and cementing agents usually have a nanohardness of 1 to 2 GPa. Carbonates and quartz are categorized at a nanohardness of 2.5 to 6 GPa and >7 GPa, respectively.

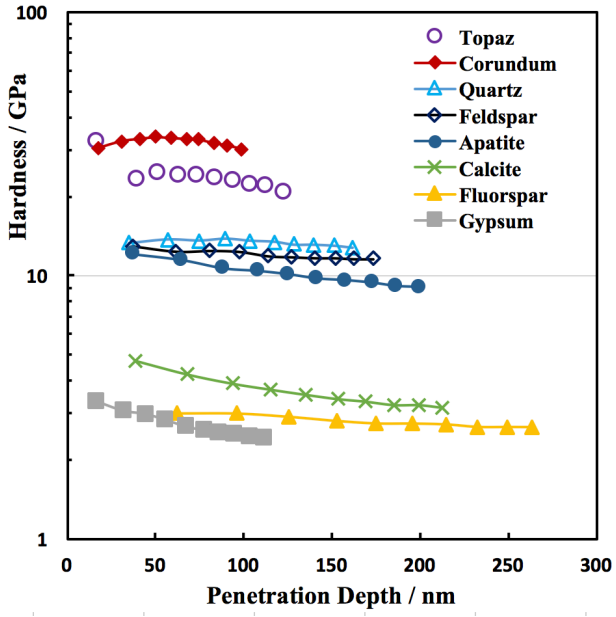

Figure 3.1 Index minerals on the Mohs scale: nanohardness vs. penetration depth (redrawing from Hangen 2001).

3.2.2 Nanoindentation Experiment on Shale

Nanoindentation technique has been developed to study a wide range of materials such as ceramics, polymers, and geomaterials. To determine the Young's modulus (E) and hardness (H) of a material at the nano-/microscale, the recorded load-displacement curves can be analyzed by the Oliver and Pharr method (Oliver and Pharr 1992, 2004; Hay and Pharr 2000). In past decades, many researchers have performed nanoindentation studies on shales and their major constituents, clay minerals, to obtain the micromechanical properties with the analysis of composition and anisotropy (Ulm and Abousleiman 2006; Zhang et al. 2009; Akrad et al. 2011; Kumar et al. 2012; Pant et al. 2013; Shukla et al. 2013; Corapcioglu et al. 2014; Shukla et al. 2015; Bennett et al. 2015). QEMSCAN was used by Akrad et al. (2011) to identify the specific mineralogy

distribution of shale core samples. They discussed the decrease in Young's modulus revealed by nanoindentation under different fluid/shale conditions. It was found that calcite, quartz, and clay-rich formations have a 30–50%, 3–30%, and 10–30% reduction in Young's modulus, respectively. The proposed concepts of "soft" and "hard" minerals were used to explain the weakening of the rock frames. Corapcioglu et al. (2014) furthered the study and concluded that mineral reactions caused by fracturing fluid are the primary cause for the reduction of Young's modulus measured by nanoindentation.

3.3 Materials and Methods

Samples were obtained from the gray/black shales from the YS108 Well at a depth of 2502–2506m in Sichuan Basin, China. A series of experiments was conducted to analyze the mineralogy, geochemistry, mechanical properties, microsurface structure, and surface hydrophobic properties through X-ray diffraction (XRD), X-ray photoelectron spectroscopy (XPS), nanoindentation testing, scanning electron microscopy (SEM), and contact-angle goniometer measurements.

3.3.1 XRD and XPS

The mineralogy of the shale sample was analyzed by XRD using the testing standard of the SY/T 5163-2010 analysis method for clay minerals and ordinary nonclay minerals in sedimentary rocks (Zeng et al. 2010). One additional intact unpolished specimen was prepared for XPS testing. The Ar ions were used to remove the surface material, sputtering each time with a 2-kV accelerating voltage for 60 seconds, followed by XPS quantitative characterization.

3.3.2 Sample Preparation

For qualitative characterization of fluid/shale interactions, the anisotropy of the rock was considered so that the same bedding planes were selected for nanoindentation. Initially, the supplied cylindrical samples had a diameter of 25mm and a height of 50 mm. They were cut into smaller pieces of approximately 10 × 10 × 5 (length × width× thickness) mm. After embedment in SamplKwick fast-cure acrylic, the top and bottom surfaces were polished so that they were parallel to each other. Then, the samples were dry polished mechanically. A MetaServ 250 polishing machine was used with SiC abrasive papers from grit size of P180 (78 mm) to P4000 (5 mm), followed by 3 mm to 0.3mm SiC abrasive papers, and finally a 0.05-mm aluminum oxide lapping film. Four ideally identical specimens (labeled as 1, 2, 3, and 4) with the same bedding orientation were prepared following the same procedure described previously. Specimens 1 and 2 were treated through chemical-vapor deposition by OTMS for 24 hours at 100°C. Specimens 1 and 3 were immersed in pure water at 21°C for 30 days. As a control experiment, Specimens 2 and 4 were placed in air at 21°C for 30 days. Fig. 3.2 shows the sample-preparation setup and the prepared specimens.

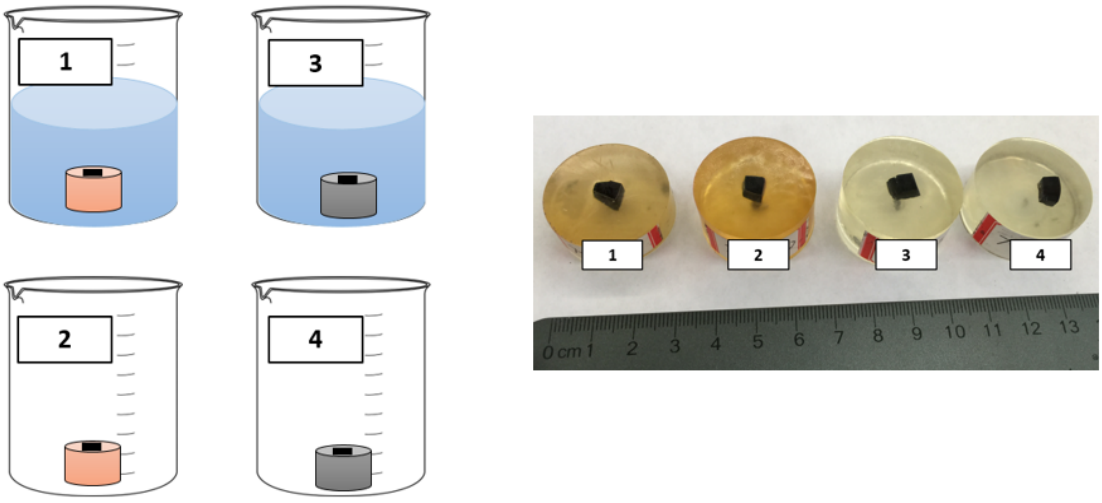

Figure 3.2 (a) Sample preparation setup: treated Specimen 1 in fresh water, treated Specimen 2 in air, untreated Specimen 3 in fresh water, and untreated Specimen 4 in air; (b) prepared samples after polishing. Specimens 1 and 2 were treated by OTMS, whereas Specimens 3 and 4 were untreated.

3.3.3 Nanoindentation Testing

Nanoindentation experiments were performed in a Keysight G200 nano indenter under depth or displacement control mode at room temperature. It has a load resolution of 50 nN and a displacement resolution of 0.01 nm. The maximum displacement range is 1.5 mm and the maximum load is 500 mN. A diamond Berkovich tip was used, with a tip radius of < 20 nm. A total of 244 individual indents were made on the four specimens. All tests were run with an allowed thermal drift rate of 0.05 nm/s. The maximum indentation depth (h_{max}) of 4 μm was selected. The CSM method with a constant target indentation strain rate ($\dot{h}/h$) of 0.05 s^{-1} was used, where h is the indentation depth. In addition, the repeated loading method under the CSM mode described in Yin and Zhang (2011) was also carried out in this study, and a five-step loading procedure was used: (1) increase load at a constant strain rate ($\dot{h}/h$) of 0.05 s^{-1} to the specified indentation depth of 4 μm; (2) hold the maximum load (F_{max}) constant for a given holding time (t_h) of 10 s; (3)

decrease load under the load control mode to 10% of F_{max} using the same loading rate ($\dot{F}$) at the maximum load $F_{\max}$; (4) hold the load (i.e., 10% of $F_{\max}$) for 100 s to record the thermal drift for correction; and (5) decrease load linearly to zero.

All indentations were performed in grid patterns. In some cases, manual selection of individual locations under the built-in optical microscope was used to avoid some rough surfaces or individual particles. Residual indent images were captured by the built-in optical microscope. The schematic diagrams shown in Figures 3.3 a and b represent the surface-deformation features and typical load-displacement curves during loading and unloading, respectively.

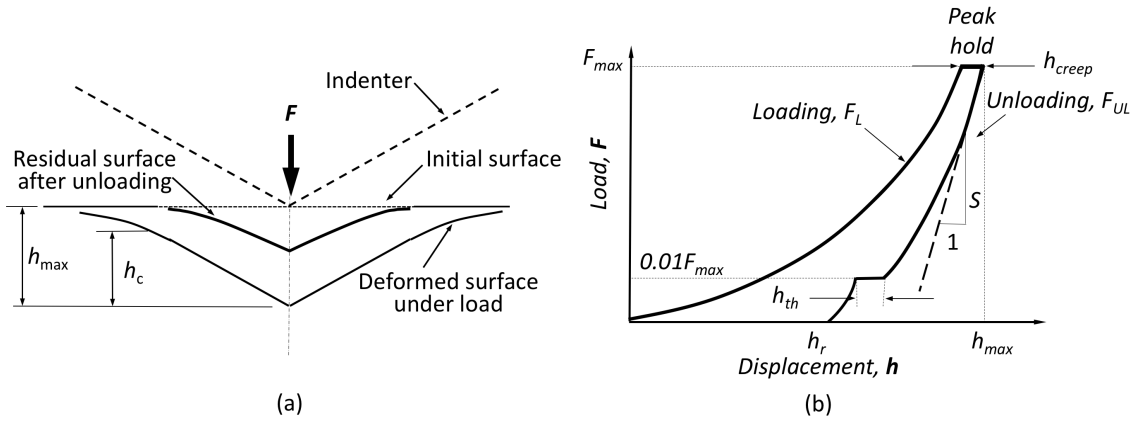

Figure 3.3 Nanoindentation diagrams: (a) loading and unloading and (b) corresponding load-displacement curve.

The Young's modulus E in the indentation-loading direction normal to the indented surface or the bedding plane is calculated with the following expression:

$$E = \frac{1-\upsilon_s^2}{\frac{1}{E_r}-\frac{1-\upsilon_i^2}{E_i}} \quad \text{Eq. (3.1)}$$

where ν_s is the Poisson's ratio of the test sample and ν_s is assumed to be 0.18 that is based on the study in the changing area (Pan et al. 2015); ν_i is the Poisson's ratio of the

diamond indenter (ν_i = 0.07); E_i is the Young's modulus of the diamond indenter (E_i = 1140 GPa); E_r is the reduced elastic modulus of the indentation contact, which can be calculated as follows:

$$E_r = \frac{1}{2\beta}\sqrt{\frac{\pi}{A_c}}S \quad \text{Eq. (3.2)}$$

where A_c is the projected contact area at F_{max} and h_{max} (Figure 3.3(b)); β is a constant related to geometry of the indenter, taken as 1.05; S is the contact stiffness obtained from the slope of the initial unloading curve at the maximum indentation h_{max} (Figure 3.3(b)) (Oliver and Pharr, 1992),

$$S = \frac{dF}{dh}\Big|_{h=h_{max}} \quad \text{Eq. (3.3)}$$

The contact depth h_c can be calculated as

$$h_c = h_{max} - \varepsilon\frac{F_{max}}{S} \quad \text{Eq. (3.4)}$$

where ε is a constant related to the geometry of the indenter (ε= 0.75); the hardness of sample, H, can be expressed as

$$H = \frac{F_{max}}{A_c} \quad \text{Eq. (3.5)}$$

where A_c is also the projected contact area at F_{max} and h_{max}.

Fracture toughness, K_c, can be calculated by using the energy method (Cheng et al., 2002). During the process of loading and unloading of the indentation, the total energy, U_t, consists of two components: elastic energy, U_e, and plastic energy, U_p. Plastic energy, U_p, is irreversible work produced in the system, which is composed of pure plastic energy, U_{pp}, and the induced fracture energy, U_{frac}. Their relations can be expressed as

$$U_t = U_e + U_p = U_e + U_{pp} + U_{frac} \quad \text{Eq. (3.6)}$$

where the total energy, U_t, and elastic energy, U_e, can be calculated per the nanoindentation load-displacement curve ((Figure 2.7(b)) as

$$U_t = \int_0^{h_{max}-h_{creep}} F_L dh \quad \text{Eq. (3.7)}$$

$$U_e = \int_{h_r}^{h_{max}} F_{UL} dh - 0.01F_{max} \times h_{th} \quad \text{Eq. (3.8)}$$

where F_L is loading; F_{UL} is unloading; h_{creep} is the creep displacement made by maximum constant load, F_{max}; h_r is the residual displacement; h_{th} is the thermal drift measured by system. Pure plastic energy, U_{pp} can be calculated by

$$U_{pp} = \left\{1 - \left[\frac{1-3\left(\frac{h_f}{h_{max}}\right)^2+2\left(\frac{h_f}{h_{max}}\right)^3}{1-\left(\frac{h_f}{h_{max}}\right)^2}\right]\right\} \times U_t \quad \text{Eq. (3.9)}$$

where the final displacement, $h_f = h_r - h_{th} - h_{creep}$, can be obtained. Then the fracture energy, U_{frac}, can be determined from

$$U_{frac} = U_p - U_{pp} \quad \text{Eq. (3.10)}$$

The strain energy release rate, G_c, is the energy dissipated during fracture per unit area of the newly created fracture-surface area. It can be obtained by dividing the projected contact area, A_c, by

$$A_c = 24.5h_c^2 \quad \text{Eq. (3.11)}$$

$$G_c = \frac{\partial U_{frac}}{\partial A_c} = \frac{U_{frac}}{A_c} \quad \text{Eq. (3.12)}$$

The fracture toughness, K_c, can then be calculated as the square root of strain energy release rate, G_c, multiplied by the reduced elastic modulus, E_r:

$$K_c = \sqrt{G_c E_r} \quad \text{Eq. (3.13)}$$

3.4 SEM and Contact-Angle Measurement

The SEM images were taken from the four differently treated specimens in a JCM-5000 NeoScope^{TM} for the purpose of comparing different treatments effects under a high vacuum. All specimen surfaces were treated with a layer of gold coating. In addition, the advancing water contact angle and receding contact angle on the surfaces of the four specimens were measured in a goniometer.

3.5 Data-Screening Criterion

Because of the heterogeneity and multiple constituents of shales, nanoindentation results from different locations are highly scattered, and the mineral compositions of each indent are unknown. It is difficult to obtain an averaged and representative curve from such a high degree of scattering. A semiempirical, hardness-based criterion is proposed to screen and analyze the scattered indentation data, so that indents made on the clay matrix can be separated from other minerals such as quartz and pyrite. In this method, the hardness/depth curves can be subdivided into three main groups that are based on the hardness values at the depth of 2 μm: 1.0 to 2.0 GPa, 2.5 to 6.0 GPa, and >7.0 GPa, which represent three types of minerals including the clay matrix, carbonates, and quartz. As such, the load-displacement and modulus-displacement curves can then be separated into three different groups, and data from each group can be averaged to obtain the representative properties. With this criterion, the separation of indentation results makes it easier to extract truly meaningful data for the mechanical properties of a clay matrix in shale, by excluding the quartz, carbonates, and other nonclay minerals. An example using this criterion can be found in the research by Xiang et al. (2017). The mechanical properties for quartz and the carbonate mineral itself shall have small variation, yet the

clay matrix is expected to vary significantly because of particle orientation, packing density, interparticle cementations, and other factors. Therefore, the variation of mechanical properties of the clay matrix can be used to characterize and define the fluid/shale interactions.

3.6 Analyses of Results

3.6.1 Mineralogy and Geochemistry

XRD analysis shows that quartz, carbonates, and clay minerals are the dominant phases in the tested shale samples. Quartz ranges from 18.5 to 42.8 wt% with an average of 30.7 wt%. Carbonates (calcite and dolomite) range from 35.9 to 54.2 wt% with an average of 45 wt%. Clay minerals range from 16.6 to 22.9 wt% with an average of 20 wt%. In addition to these three groups of major minerals, albite and pyrite also exist with a <4 wt%. For the clay minerals, illite and chlorite are the two major phases with a range of 82 to 90 wt% and 10 to 18 wt%, respectively.

Table 3.1 shows the types of elements existing in the top zero to 10 nm of the tested shale sample, with the descending order that is based on the number of atoms. Beneath etching the top 5- to 10- μm layers, a monatomic compositional profile (Fig. 3.4) was obtained. It was found that the atomic percentages do not change significantly after the removal of the top 5- to 10-μm layer of the material.

Table 3.1 Atomic percentages of the shale surface from XPS measurement.

Elements	Atom (%)
O	62.2
Si	16.1
C	9.2
Al	6.6
K	2.2
Na	2.1
Ca	0.8
Fe	0.5
N	0.2

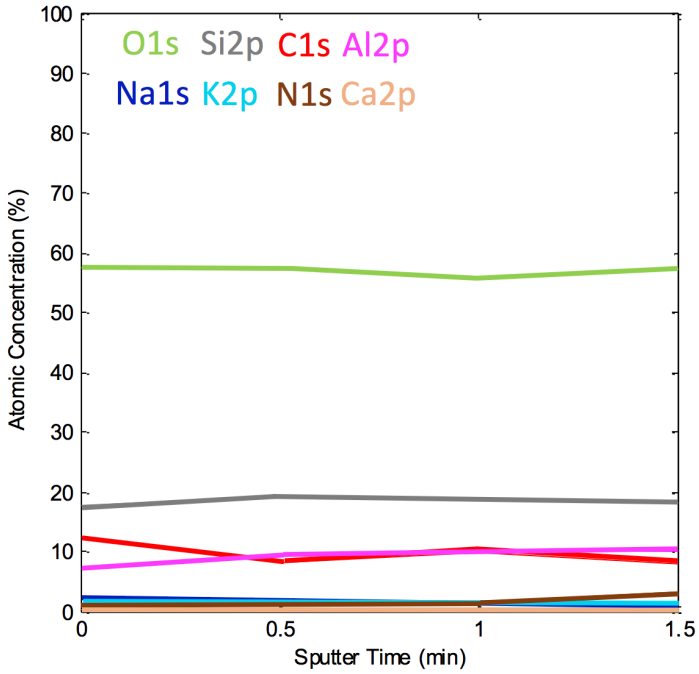

Figure 3.4 Monatomic depth profile of the shale surface. It shows that the atomic percentages do not change considerably after the top 5- to 10-μm layer of the shale surface was etched.

3.6.2 Effect of Different Hydrophobic Chemicals as Coatings

In the preliminary study, three hydrophobic-coating chemicals were used to alter the shale surface's hydrophobicity: polydimethylsiloxane (PDMS), dimethyldichlorosilane (DMDCS), and OTMS. To examine the suitability of these chemicals as hydrophobic coatings for rocks, a clay-rich shale (i.e., with a clay fraction of

40 to 70 wt%), Opalinus shale, was used. On the basis of previous work related to the fracture toughness of shales (Liu 2015), the microstructures of untreated and treated Opalinus shale are shown in Fig. 3.5. The Opalinus-sample orientation is parallel to the bedding plane.

The SEM micrographs of the Opalinus shale indicate that the hydrophobic coating does not change the surface textures of the shale sample. The coatings are generally only a few nanometers in thickness (Fadeev and McCarthy 2000), which cannot be detected by SEM, and the micromorphology of the microscale flake-shaped clay particles is not altered by such thin coatings. The cracks and voids between quartz grains and clay matrix are not filled by smaller particles. Contact-angle measurements from these coated surfaces show that the OTMS coating can lead to a more-hydrophobic surface compared with PDMS and DMDCS. Therefore, OTMS was chosen as the coat chemical for the Sichuan shale, to investigate the effects of surface hydrophobicity on the interactions between water and shale. SEM images of the four prepared shale specimens are shown in Figs. 3.6 a through 3.6 d.

One can see from Fig. 3.6 a that the surface of Specimen 1 has slight-to-moderate erosion or dissolution by water. A few incidents of surface-peeling and spallation also can be observed. Fig. 3.6 b shows that Specimen 2 also has a smooth surface even after coating. Many pyrite framboids can be observed, with a group of framboids approximately one 4-mm-deep residual indent. Some natural texture and cracks existed in the shale. Fig. 3.6 c shows that Specimen 3 exhibits high etching or dissolution by means of water/shale interactions, because some exfoliations and newly generated pores become visible. Fig. 3.6 d illustrates that Specimen 4 (as a control sample) has some naturally

formed very small pores (so-called nanoporosity) and small cracks. In addition, clay flakes, organic matter, and silt-sized quartz grains can be observed.

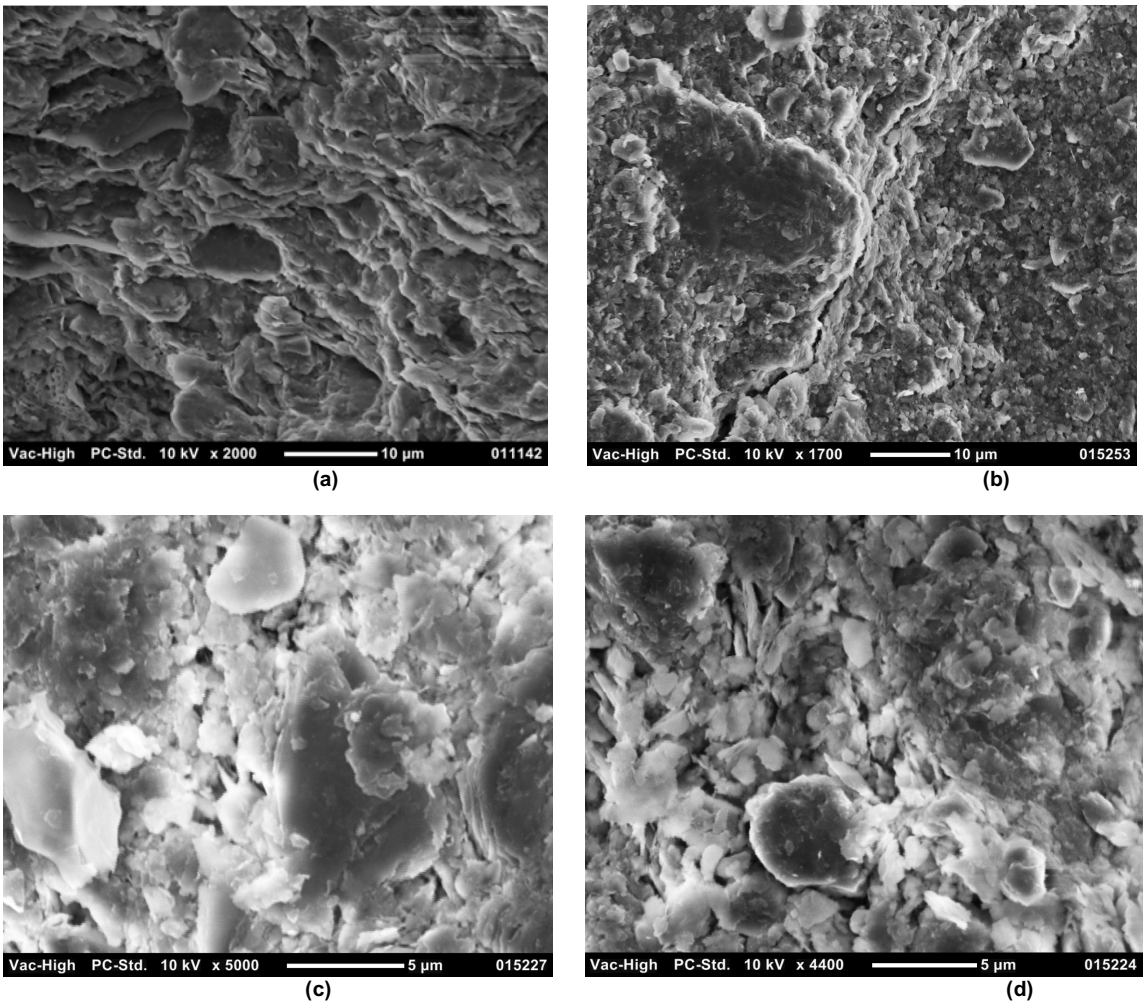

Figure 3.5 SEM images of clay-rich Opalinus shale treated by different hydrophobic chemicals: (a) clean surface without coating (Liu 2015); (b) surface treated by PDMS; (c) surface treated by DMDCS; and (d) surface treated by OTMS. The coatings do not change the surface microstructure. The flake-shaped clay particles in Opalinus shale are the dominant constituents.

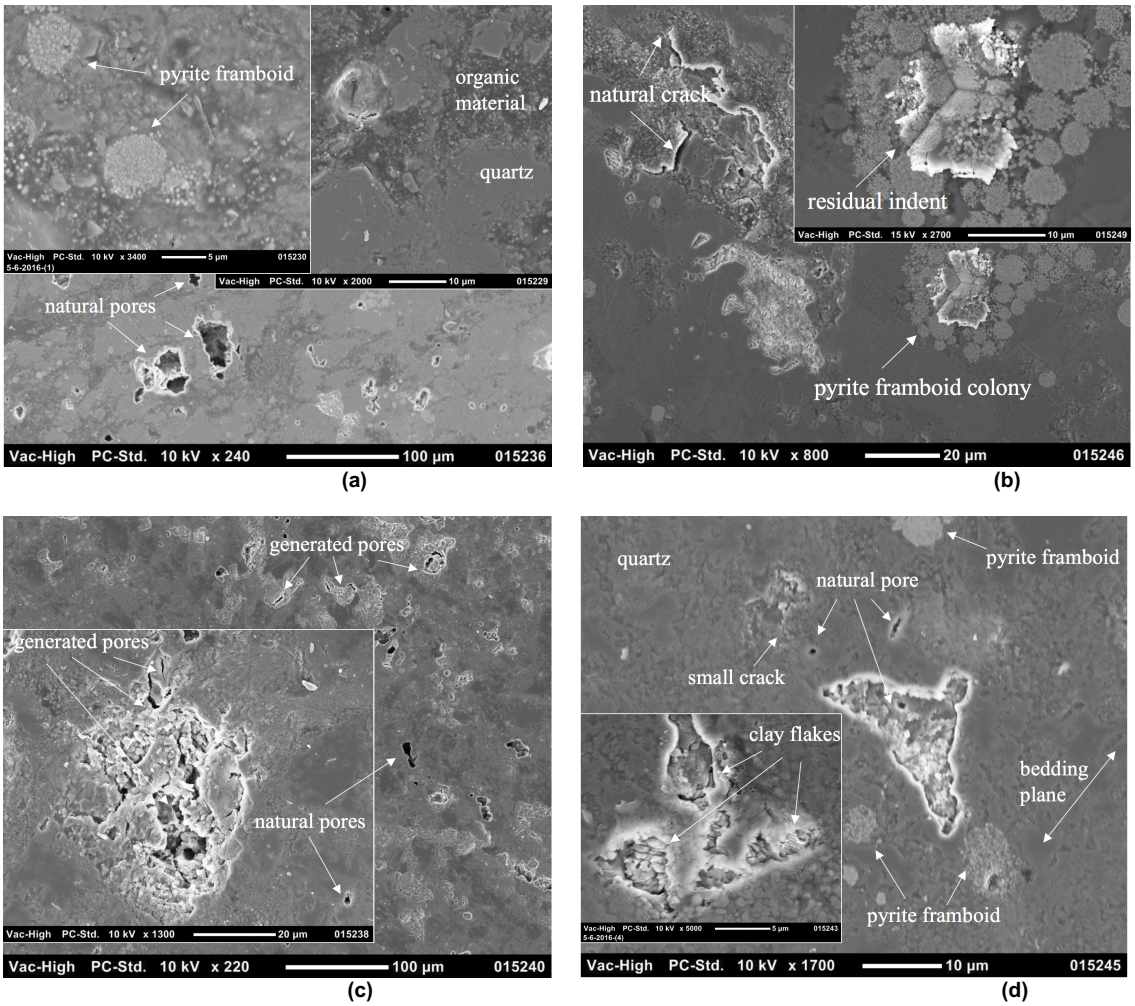

Figure 3.6 SEM images of the shale specimens: (a) OTMS-coated Specimen 1 in fresh water after 30 days; (b) OTMS-coated Specimen 2 in air after 30 days. Residual Berkovich indent with a 4-lm depth surrounded by pyrite framboids; (c) untreated Specimen 3 in water after 30 days; and (d) untreated Specimen 4 in air after 30 days.

3.6.3 Hardness, Young's Modulus, and Fracture Toughness by CSM

Micromechanical properties including hardness, Young's modulus, and fracture toughness can be obtained from the nanoindentation experiments. The descending orders of these properties including hardness, Young's modulus, fracture toughness, and water-contact angle of the clay matrix are similar for the four specimens. The hardness and the fracture toughness follow the order of Specimen 4 (uncoated in air)>1 (coated in water)>2 (coated in air)>3 (uncoated in water), whereas the Young's

modulus and contact angle are in the order of Specimen 2 (coated in water)>4 (uncoated in air)>1 (coated in water)>3 (uncoated in water). After screening the nanoindentation results with the newly proposed clay-matrix-based criterion, the H and E of the clay matrix are summarized in Figs. 3.7 and 3.8, respectively. Fig. 3.7 shows that the hardness of the clay matrix does not change significantly with depth, particularly at large depths. Despite the scattering at smaller depths, the hardness becomes a constant with smaller error bars when the depth exceeds approximately 2000 nm. The hardness at a depth of 3878 nm for Specimens 1, 2, 3, and 4 is 1.23 ± 0.53 GPa, 1.13 ± 0.14 GPa, 0.74 ± 0.43 GPa, and 1.42 ± 0.12 GPa, respectively. In fact, there is a 47.8% reduction in hardness after the untreated/uncoated Specimen 3 interacted with water at room temperature for 30 days, whereas the treated/coated Specimen 1 possesses a 39.8% higher hardness than Specimen 3. For the two specimens exposed to air (Specimens 4 and 2), instead of water, their hardness/depth curves intersect at a depth of 500 nm, which is likely attributed to the scattered properties of shale. At larger depth (e.g., 4000 nm), the difference becomes much smaller compared with a smaller depth (500 nm).

In Fig. 3.8, the Young's modulus of clay matrix for the four specimens also shows significant variations after a certain level of depth. This is especially true for Specimen 3, which exhibits a trend of decreasing Young's modulus with large errors. The Young's modulus of the clay matrix at the depth of 3880 nm for Specimens 1, 2, 3, and 4 is 44 ± 14 GPa, 51 ± 4 GPa, 33 ± 11 GPa, and 45 ± 2 GPa, respectively. There is a 26.7% reduction in the Young's modulus after the untreated/uncoated Specimen 3 interacted with water at the room temperature for 30 days, whereas the treated/coated Specimen 1 possesses a 25% higher Young's modulus than Specimen 3.

Likewise, the fracture toughness of the clay matrix shows a trend similar to that of the hardness. The averaged results using the energy method for Specimens 1, 2, 3, and 4 are 2.38 ± 0.58, 2.25 ± 0.64, 1.54 ± 0.38, and 2.72 ± 0.17 MPa MPa$\sqrt{\text{m}}$, respectively. There is a 43% reduction in fracture toughness after the untreated/uncoated Specimen 3 interacted with water at room temperature for 30 days. The treated/coated Specimen 1 possesses a 35% higher fracture toughness than Specimen 3.

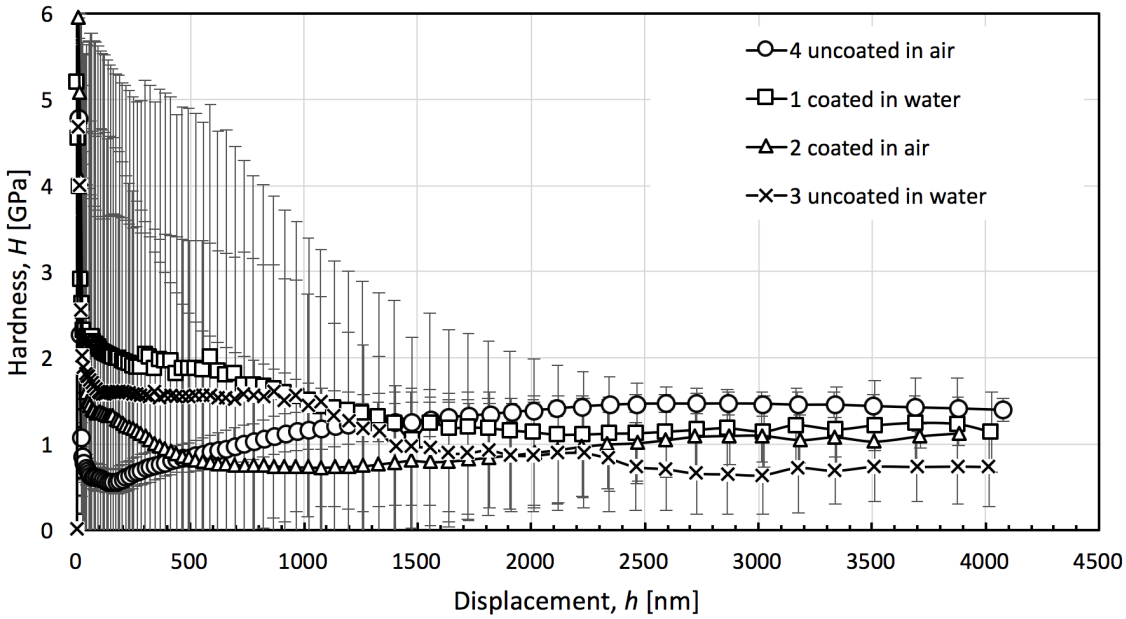

Figure 3.7Averaged hardness/depth curves of clay matrix obtained by the CSM method after 30 days at room temperature. Beyond 2000 nm of depth, the hardness values are in the order of Specimen 4 (uncoated in air) > 1 (coated in water) > 2 (coated in air) > 3 (uncoated in water).

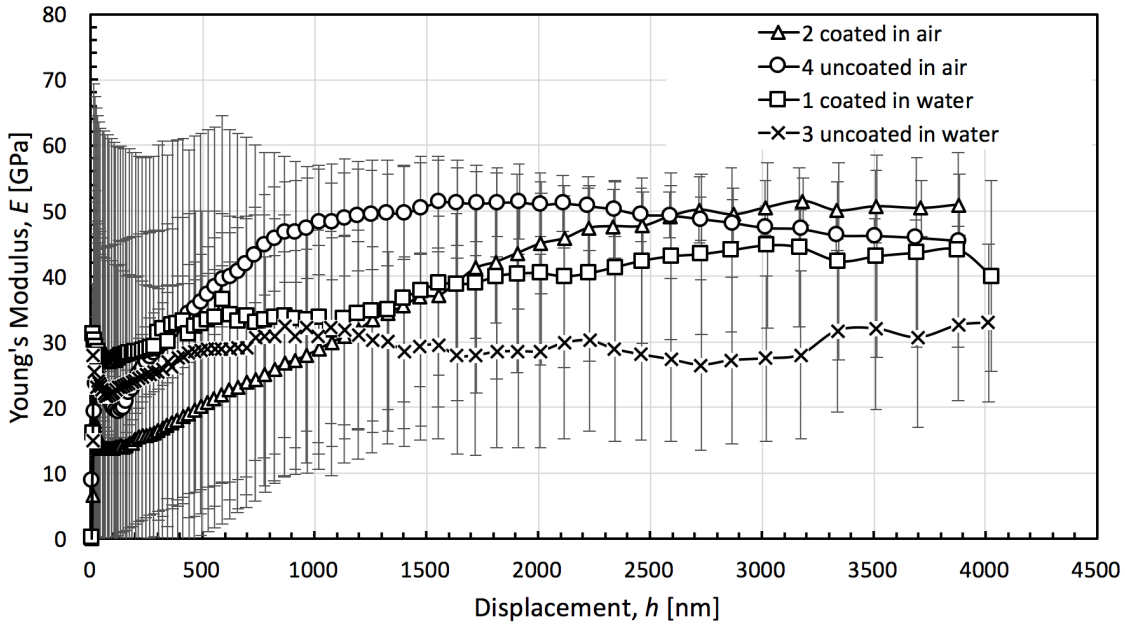

Figure 3.8 Averaged Young's-modulus/depth curves of clay matrix obtained by the CSM method after 30 days at room temperature. Beyond 2000 nm of depth, the Young's modulus values are in the order of Specimen 2 (coated in water) > 4 (uncoated in air) > 1 (coated in water) > 3 (uncoated in water).

3.6.4 Comparison of Hardness Results Obtained by the CSM Method and Repeated Loading Method

The hardness results obtained by the CSM method and repeated loading method are further compared in Figs. 10 through 13. All the scattered data in the figures are raw data obtained with the repeated loading method.

The dash line represents an average trend line for the repeated loading results, whereas two or three solid lines show where the CSM data fall inside the scattered band of data using the repeated loading method.

From these figures, there is a significant variation in the hardness and maximum load when measured at different depths. Both methods have a wide band of scattering data. Fig. 10 is a good example to show that only carbonate minerals and clay matrix (two solid lines) can be detected by both the CSM and repeated loading results, whereas

Figs. 11 through 13 yields three groups of minerals (as represented by the three solid lines) from the CSM results. For example, in Fig. 12, the three solid lines represent the averaged values after the three major groups of minerals were separated by use of the proposed clay-matrix-based data-screening criterion, which falls inside the dominant area of the scattered data obtained by the repeated loading method. Averaged values from these two methods are not comparable, because the repeated loading only uses a simplified averaging process from all data, which does not consider the screening or classification

of different mineral groups. However, the CSM method with the screening of clay matrix can retrieve the properties of three mineral groups including clay matrix, carbonates, and quartz from the complex multiphase shale. Both the CSM method and the repeated loading method can provide a similar broad range of properties for shale. Yet, only the CSM method with the clay-matrix-based data-screening criterion can capably characterize the fluid/shale interactions. In addition, the limited amount of performed indents may be another reason why the repeated loading method cannot yield the results for the separation of the three major mineral groups in shales.

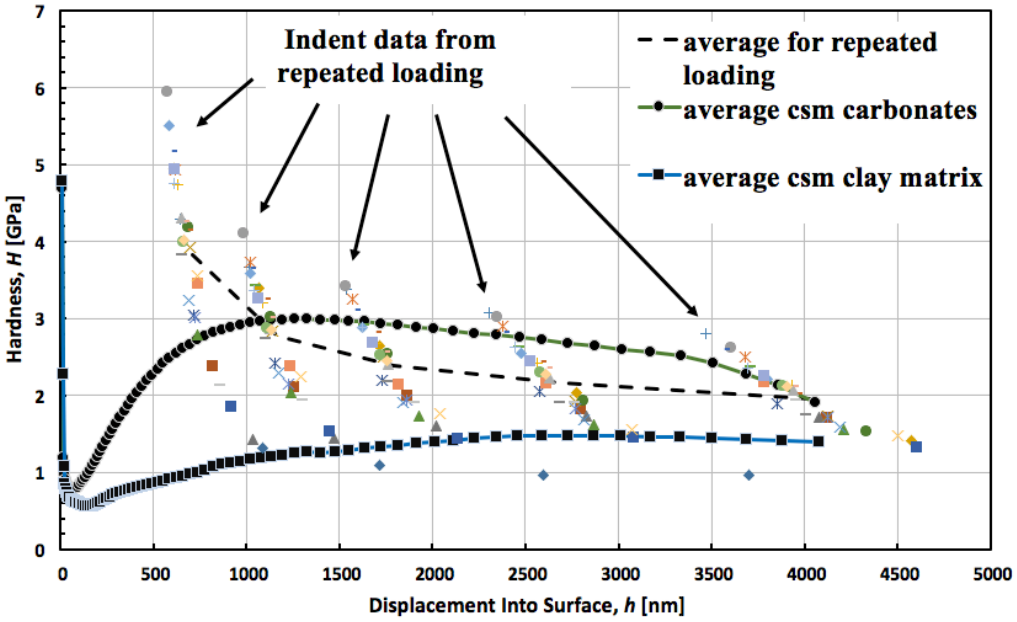

Figure 3.9 Nanoindentation results using the CSM method and the repeated loading method (Specimen 4).

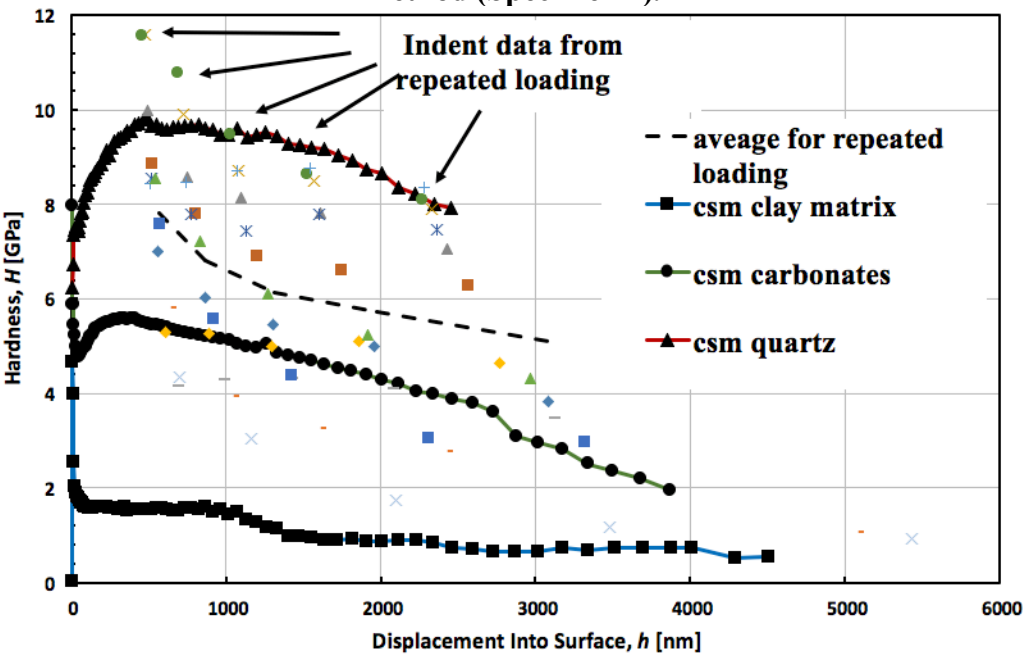

Figure 3.10 Nanoindentation results using the CSM method and the repeated loading method (Specimen 3).

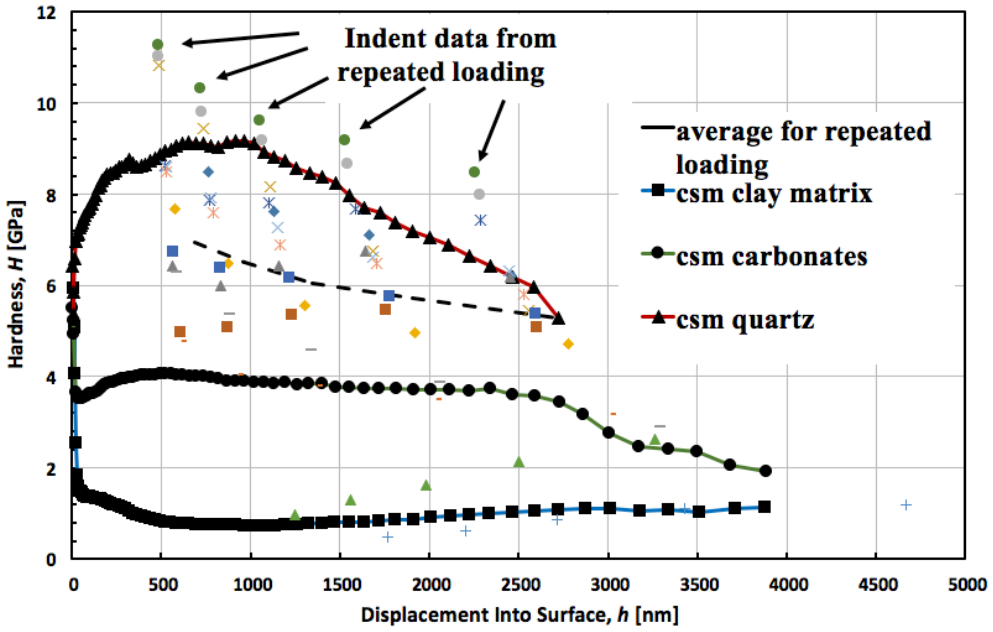

Figure 3.11 Nanoindentation results using the CSM method and the repeated loading method (Specimen 2).

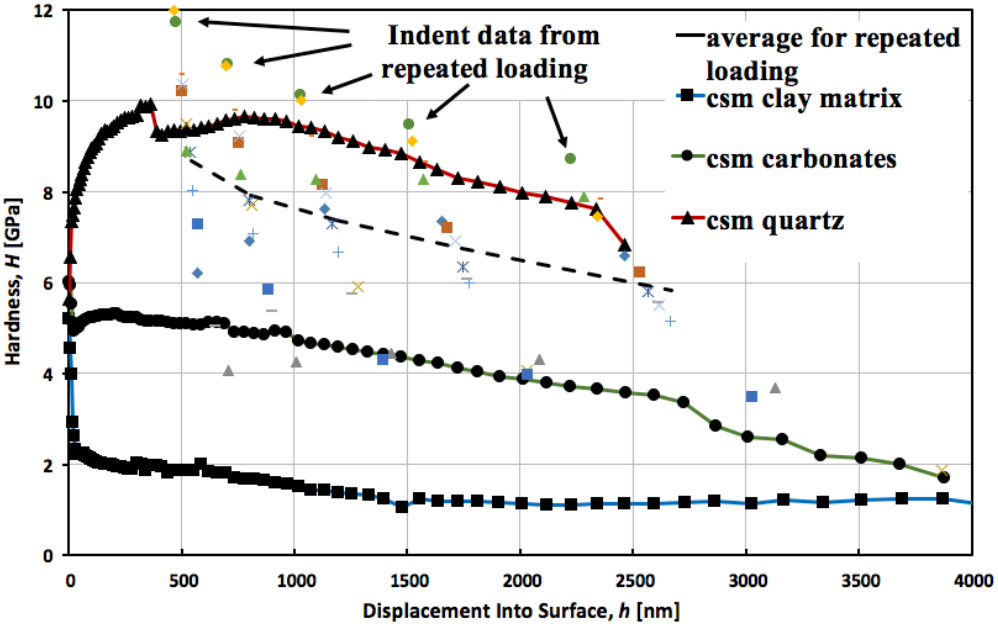

Figure 3.12 Nanoindentation results using the CSM method and the repeated loading method (Specimen 1).

3.6.5 Contact Angle

Table 3.2 shows the measured contact angles. From this table, clearly Specimen 2 has the highest degree of hydrophobicity, whereas the uncoated specimen has an advancing contact angle of 77º. The specimen with the OTMS coating in air has a water-contact angle of 103º, indicating that OTMS can convert the shale's hydrophilic surface to hydrophobic. However, prolonged (i.e., 30 days) inundation in water indicated that the OTMS hydrophobic coating on the shale surface can gradually degrade. In fact, Specimen 1 gradually recovers its hydrophilicity as the advancing and receding water-contact angles decrease to 75º and 0º, respectively, similar to those on the uncoated specimen (i.e., Specimen 4). The two uncoated specimens exhibit similar water-contact angles (i.e., 69º vs. 77º).

Table 3.2 Contact angles of the four specimens after 30 days at room temperature.

	Advancing contact angle (º)	Receding contact angle (º)
1 Coated in water	75	0
2 Coated in air	103	93
3 Uncoated in water	69	0
4 Uncoated in air	77	0

3.7 Conclusions

In this paper, surface hydrophobization was used to treat shale specimens to study the effect of hydrophobic coating of the fracture surfaces on fluid-induced damage or softening. Nanoindentation results including hardness, Young's modulus, and fracture toughness show that specimens without hydrophobic treatment, after submerging in water for a certain length of time, show significantly lower Young's modulus and hardness compared with those that have been treated with a layer of hydrophobic coating. Overall, surface hydrophobization can mitigate the negative effects of fluid/shale interaction by preventing the reduction in mechanical properties caused by softening. In addition, the following specific conclusions can be drawn:

- A significant reduction in Young's modulus, hardness, and fracture toughness was observed after shale specimens were inundated in water for 30 days at room temperature. Specifically, the specimens without any surface treatment showed a 47.8% reduction in hardness, a 26.7% reduction in Young's modulus, and a 43% reduction in fracture toughness, and such softening occurs in the clay matrix.
- Hydrophobic OTMS coating can prevent water-induced softening of shale rocks. The OTMS-coated specimen has a 39.8% higher hardness, 25% higher Young's modulus, and 35% higher fracture toughness than the uncoated one.
- The proposed clay-matrix-based data-screening criterion is convenient for dealing with highly scattered nanoindentation data obtained from highly heterogeneous shales. The hardness of the constituent minerals in shale can be classified into three major groups: clay matrix, carbonates, and quartz with hardness values of

1.0 to 2.0 GPa, 2.5 to 6.0 GPa, and >7.0 GPa, respectively. Grouping shale's constituent minerals can assist the understanding of the fluid/shale interactions and associated negative effects on shale's mechanical properties.

- The two loading methods (i.e., the CSM method and the repeated loading method) used in this study yield similar results on the shale's mechanical properties. However, only the CSM method with a clay-matrix-based data-screening criterion is capable to defining and characterizing fluid/shale interactions.

CHAPTER 4

CONTAMINATED HIGH-PLASTICITY CLAY BY HYDRAULIC FRACTURING FLUIDS[2]

4.1 Abstract

This study aims to examine the changes of geotechnical properties of high-plasticity clay by hydraulic fracturing fluid and to predict the contaminated fluid-clay behavior based on Hattab-Chang model. Similar to electrical double layer van der Waals forces, repulsive and attractive forces derived from energy potentials are used to describe soil behavior under different pore fluid concentrations. The designed contaminated samples are composed of remolded saturated high-plasticity clays and hydraulic fracturing fluids ranging from 0 to 100% industry-supplied concentration, designated as C_0, $C_{0.1}$, $C_{0.5}$, and C_1. The relationship between local model parameters and pore fluid concentration is obtained using the executed geotechnical experiments including Atterberg limits, direct shear, and one-dimensional load increment consolidation. The geotechnical experiments provide the results including soil consistency, hydraulic properties, and shear strength with respect to different pore fluid concentrations. The Hattab-Chang model is supplemented with a relationship between the surface potential characteristic value of $\widetilde{A_N}/\tilde{B}$ and different pore fluid concentrations.

[2] This paper was accepted for presentation at the GeoShanghai International Conference 2018, May 27-30, 2018, Shanghai, China, Elsevier. GSIC 2018: Proceedings of GeoShanghai 2018 International Conference: Geoenvironment and Geohazard pp 567-574. https://doi.org/10.1007/978-981-13-0128-5_62.

4.2 Introduction

When considering the success of hydraulic fracturing, multiple issues remain regarding to environmental safety and engineering properties. Due to the contamination of produced water, geotechnical properties of the contaminated soil can change, which could have a detrimental impact on the soil mechanics or adjacent structures. Plenty of researchers studied the effect on geotechnical properties by leaked gas oil on soils. However, the contamination caused by of fracturing fluids has been omitted.

The studies on contaminated fine-grained soil has been many decades. The influence of petroleum-derived oil contamination on the geotechnical properties of different soils has been widely studied (Aiban, 1998; Al-Sanad et al., 1995; Jia, Wu, Shang, Yang, & Shan, 2011; Khamehchiyan et al., 2007; Nasehi et al., 2016; Nazir, 2011; Puri, 2000; Rahman, Hamzah et al., 2010; Shin & Das, 2001). Among the factors influencing the engineering properties, the effect of electrostatic force, change in concentration of pore fluid, chemicals in pore fluids, aging effects, and dielectric constant could be found in previous studies (Al-Sanad & Ismael, 1997; Barbour & Yang, 1993; Meegoda & Ratnaweera, 1994; Moore & Mitchell, 1974; Olchawa & Kumor, 2007). However, to authors' knowledge, no previous investigation is done on contaminated high plasticity clays (CH) with industry-supplied fracturing fluid. The specific effect of contaminated fluid concentration is unknown.

This study aims to examine the changes of geotechnical properties of CH clay by fracturing fluid and to predict the contaminated fluid-clay behavior based on Hattab-Chang model, which consider clay clusters, inter-aggregate forces, and energy potential

effects (Hattab & Chang, 2015). Like electrical double layer van der Waals forces, repulsive and attractive forces derived from energy potentials are used to describe soil behavior under different pore fluid concentrations. The designed samples are composed of remolded saturated high-plasticity clays mixed with hydraulic fracturing fluids ranging from 0 to 100% industry-supplied concentrations, designated as C_0, $C_{0.1}$, $C_{0.5}$, and C_1. The relationship between local model parameters and pore fluid concentrations is obtained using the executed experiments including Atterberg limits, direct shear, one-dimensional consolidation. The modelling will be simulated to investigate the relationship between characteristic value of $\widetilde{A_N}/\tilde{B}$ and different concentrations of pore fluid.

4.3 Materials and Methods

4.3.1 Sample Preparation

A Heiden clay sample was obtained from Norman, OK with a dark grey/black color. All the soil index properties could be found in previous study (Lutenegger and Rubin, 2008). Produced water/fracturing fluid sample was provided from an industry site in Houston, TX. The industry-supplied fracturing fluid samples were of negligible viscosity and colored urine yellow. To prepare different concentrations of produced water, the stock solution concentration C_1 was diluted with Mili-Q water to 2 times and 10 times, designated as $C_{0.5}$ and $C_{0.1}$. C_0 was defined as the solution concentration of Mili-Q water. Pulverized clay samples were mixed thoroughly with different fracturing fluid samples at concentrations of C_0, $C_{0.1}$, $C_{0.5}$, and C_1 reaching their liquid limit and left in a moisture room for a week to allow to reach equilibrium.

4.3.2 Methods

To obtain a fundamental comprehension on the change of shear behavior of clayey soil contaminated by fracking fluid, a series of geotechnical laboratory tests were implemented including Atterberg limits, 1-D incremental consolidation test (IL), and direct shear tests (DS).

To further investigation of the proposition that clay can be regarded as an assembly of clusters or aggregates, the workflow by Hattab and Chang (2015) is adopted to provide a reasonable method to consider inter-aggregate forces and energy potential effect on clay deformation (Hattab & Chang, 2015). Different concentrations of contamination in pore fluid are expected to have reasonable correlation with local parameters in the model.

It was assumed that the change of intra-cluster pores is negligible. In the saturated medium, the two clusters in the model have the radius of R, with the length connecting the two centers designated as l_c. Two types of potentials govern the neighboring clusters: repulsive type ψ_R, and attractive type ψ_A. The resulting potential ψ can be described as:

$$\psi = \psi_R + \psi_A \quad \text{Eq. (4.1)}$$

$$\psi_R = \tilde{B} R e^{-d_{min}^{-1}(l_c - 2R)} \quad \text{Eq. (4.2)}$$

$$\psi_A = -\tilde{A}\left[\frac{2R^2}{l_c^2 - 4R^2} + \frac{2R^2}{l_c^2} + ln\left(\frac{l_c^2 - 4R^2}{l_c^2}\right)\right] \quad \text{Eq. (4.3)}$$

where $\tilde{B}$ and $\tilde{A}$ are parameters related to surface potential of clusters depending on the mineralogy of the clay and the pore fluid chemistry; $2d_{min}$ is the minimum distance between two clusters in the model. The inter-cluster force f is introduced in Eq. (4.4) which represents the sum of the repulsive and attractive forces

$$f = -\tilde{B}Rd_{min}^{-1}e^{-d_{min}^{-1}(l_c-2R)} + \tilde{A}R^2\left[\frac{l_c}{(l_c^2-4R^2)^2} + \frac{1}{l_c^3} - \frac{2}{l_c(l_c^2-4R^2)}\right] \quad \text{Eq. (4.4)}$$

where $\tilde{B}$ and $\tilde{A}$ can also be normalized as $\tilde{A}_N = \frac{\tilde{A}}{d_{min}}; R_N = \frac{R}{d_{min}};\ l_N = \frac{l_c}{d_{min}}$. From the experimental data, the formula derived by Hattab and Chang between branch length l_c and void ratio e can be described by the following (Hattab & Chang, 2015):

$$l_c = 2R\sqrt[3]{(1+e)/(1+0.35)} \quad \text{Eq. (4.5)}$$

where assuming the closely packed assembly has a void ratio 0.35 as hexagonal packing. The coordination number of the assembly is assumed to be 12. The relation between force f, displacement l_c, and stress p' are then given as

$$f = \frac{p'}{l_c}\frac{(\frac{\pi}{3})(2R)^3(1+e)}{12} \quad \text{Eq. (4.6)}$$

where the stress p' in the model was isotropic effective stress through experiments. In macro-scale, the experimental relation w-p' is presented in terms of water content w with respect to p'. In micro-scale, the calculated relation l_c-f can be expressed between branch length l_c and local force f between the two neighboring clusters. Then, the three parameters $\tilde{B}$, $\tilde{A}$, and d_{min} can be determined based on the three known points in the l_c-f curve.

4.4 Results and Discussion

4.4.1 Geotechnical Experiments

Atterberg limits are determined as the preliminary assessment of the soil's mechanical properties for different mixture samples (Fig. 4.1 (a)). The results indicated that the liquid limit (LL) and plastic limit (PL) decreased with increasing fracturing fluid concentration percent, which is the contrary to the effect exhibited by the role of gas oil. The decrease can be explained by the discussion of Arasan (2010), who summarized the effect of chemicals on geotechnical properties of different types of clay (Arasan, 2010). For CH clays, the salt solution tends to reduce the thickness of the Diffuse Double Layer (DDL) and flocculate the CH clay particles, resulting in a decline of LL of CH clay. Fig. 4.1 (b) – (d) present results of 4 series of IL consolidation tests for different mixtures of fracturing fluids. The consolidation curves are shown and compared either in the form of end of increment (EOI) or end of primary consolidation of (EOP) for each loading stage. Casagrande method was used to calculate the Coefficient of Consolidation (C_v) values. Results of C_v show a clear increase for contaminated CH samples ranging from $C_{0.1}$ to C_1. Yet, it also reveals that different contaminated concentrations show minor effect on variation of permeability properties of the contaminated CH soil. In general, the C_v values show a similar decreasing tendency for both the clean and contaminated CH clay as the consolidation stress increases. The Compression index (C_c) values were obtained from the virgin compression curves. The overall decrease trend shows similarity with the gas oil contamination study on Kaolinite (Khosravi et al., 2013).

Results of both undrained and drained DS tests are shown in Fig. 4.2. The quick DS tests were carried out at a consolidation period of 24 hours prior to a rate of shear

deformation equal to 0.5 mm/min at normal stress of 25, 50, and 75 kPa. The slow DS tests were implemented at a consolidation period of 24 hours following a shear deformation of 0.00694 mm/min (24 hours). To verify the fully drained condition, a shear deformation of 0.00347 mm/min (48 hours) was performed, which was proved to have a nearly identical curve. It can be seen from Fig. 4.2 (a) that the apparent cohesion is generated by building up the pore pressure when the specimen is sheared fast. The friction angle increases with increasing contaminated concentration of fracturing fluids, which is found to the opposite for contamination by gas oil (Nasehi et al., 2016). For drained DS test results on remolded mixture samples (cohesion is 0), both friction angle from peak and residual value increase with increasing contaminated concentrations (Fig. 4.2 (b)).

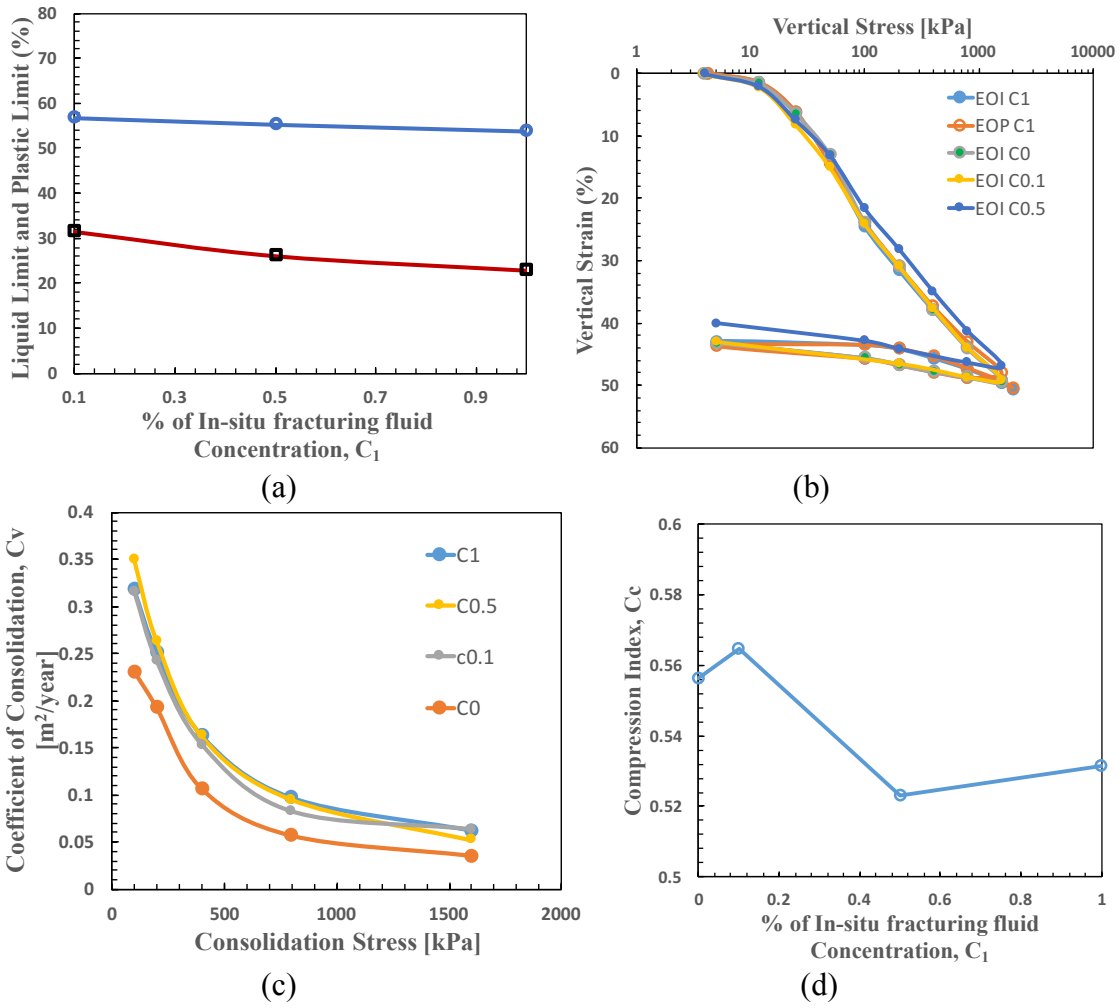

Figure 4.1 (a) Atterberg Limits Results; (b) εv-p curve of IL consolidation test; (c) Cv-p curve of IL consolidation test; (d) Cc variation with respect to different fracturing fluid concentrations.

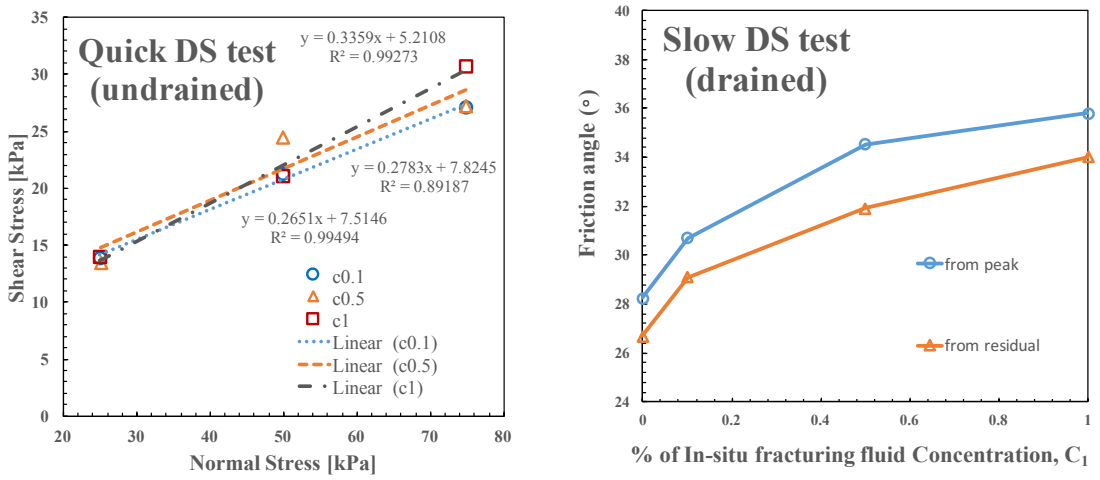

(a) (b)

Figure 4.2 (a) Quick DS test (undrained); (b) Slow DS test (drained).

4.4.2 Modelling and Prediction

As in the previous modelling for kaolinite or mixture with montmorillonite, a radius of 4 μm was assumed for single clay cluster in this modelling. Fig. 4.3 (a) shows the macro-scale *w-p'* relationship for different fluid-soil mixtures ranging from C_0 to C_1. Due to the inconsistency and man-made uncertainty of preparing the specimen at initial condition, initial water content of sample with $C_{0.1}$ shows a bit higher than its LL. This is the main reason of the deviation of the curve from others. After the calculation using Eq. (4.4), (4.5), and (4.6), micro-scale l_c-f as shown in Fig. 4.3 (b) could be obtained. Based on three known points on each curve, three characteristic parameters $\tilde{B}$, $\tilde{A}$, and d_{min} can be determined for each fluid-soil mixture. The obtained model parameters were plotted in Fig. 4.4 (a) as well as mixtures of kaolinite and montmorillonite from Chang's data (Hattab & Chang, 2015). The fluid-clay mixtures fell in the range between kaolinite and montmorillonite in the validity domain of the model. In addition, Fig. 4.4 (b) presents a relationship between characteristic values and different pore fluid concentrations.

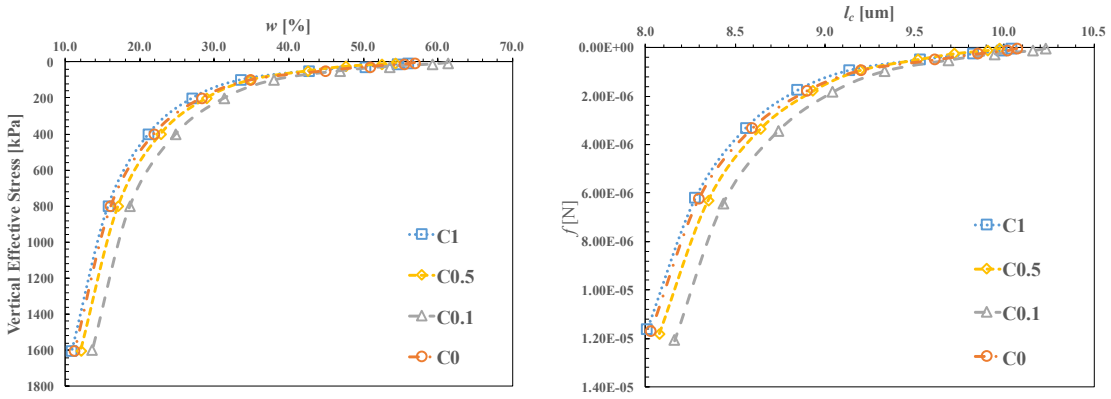

(a) (b)

Figure 4.3 (a) experimental data from IL consolidation; (b) Calculated local parameters.

The simulation curve can be obtained when three characteristic parameters $\tilde{B}$, $\tilde{A}$, and d_{min} were put into Eq. (4.4). The simulated local behavior l_c-f was found to be approximately identical to the experimental results. Even though the Eq. (4.4) has the realistic physical significance to describe micro-scale behavior, a simple exponential equation is a better fit than Eq. (4.4). Their relationship cannot be verified until further investigation is accomplished.

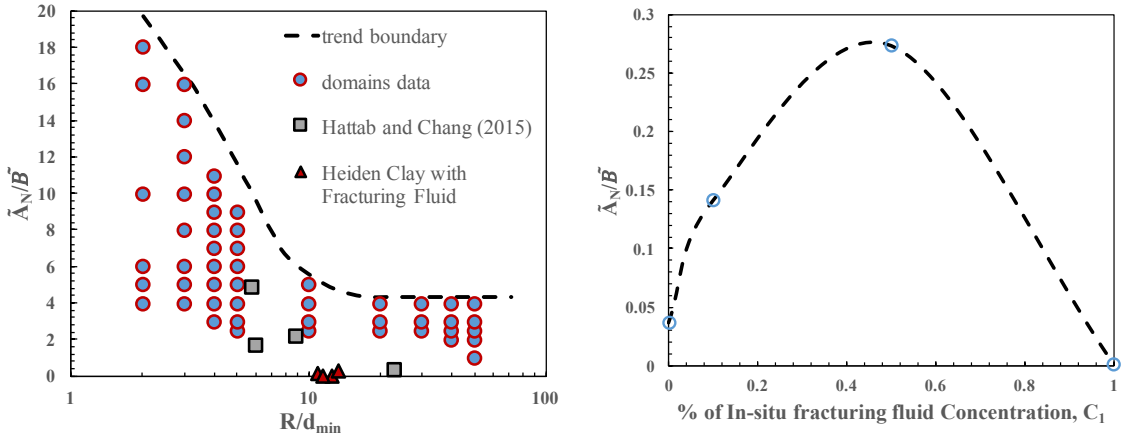

(a) (b)

Figure 4.4 (a) Model's valid domain for the Heiden Clay data and literature; (b) Effect of different concentrations of fracturing fluid on characteristic values of $\widetilde{A_N}/\tilde{B}$.

4.5 Conclusions

The study presents a series of experimental investigations and modelling on the geotechnical properties of CH clay when contaminated with different concentrations of fracturing fluids. The following conclusions are made, based on the results and discussions:

- LL and PL decrease with increasing contaminated concentration for CH clay.
- The value of C_v increases to a nearly uniform range with different contaminated concentrations from $C_{0.1}$ to C_1.
- Shear strength of CH clay increases with fracturing fluid contamination.
- Neither positive nor negative correlation is found for the C_c of fracturing fluid contaminated CH clay. The compressibility of high-plasticity clay shows a decrease and an increase afterward as the pore fluid concentration increases. Unless further studies on the variation of C_c with pore fluid concentration are accomplished, a general conclusion cannot be given.
- DS test with a shear deformation of 0.00694 mm/min is adequate to ensure no pore pressure is generated after verification with 48 hours of shearing. Performing DS test at a faster shear rate cannot provide accurate strength index for the contaminated mixture.
- The Hattab-Chang model is applicable for Heiden clay mixing with fracturing fluid. The effect of different pore fluid concentrations is provided with respect to the characteristic value of $\widetilde{A_N}/\widetilde{B}$.
- The assumed K_0 condition in this modelling is easier to fabricate in 1-D consolidation test compared to the triaxial isotropic loading method.

CHAPTER 5

EXPERIMENTAL INVESTIGATION FOR FRACTURING FLUIDS-CONTAMINATED SHALE BY MEANS OF NANOINDENTATION AND XRD

5.1 Abstract

An experimental investigation for hydraulic fracturing fluid-contaminated shale is implemented by means of nanoindentation and X-ray diffraction (XRD). This paper adopts the clay-matrix-based criterion for nanoindentation screening. The XRD result provides a means to identify mineral alterations when shale get contaminated by hydraulic fracturing fluid, which is discussed as well as the hardness changes measured by nanoindentation. This unique experimental method provides the first trial study when only considering clay minerals as the major factor in the fluid/shale interaction system and using a scanning electron microscope (SEM) allows visual verification in the process. A characteristic depth, h_c, is proposed to consider hardness and mineral alteration in the meantime. In addition, a correlation is proposed between fracture toughness (Kc) and hardness (H) with Young's modulus (E) for clean shales.

5.2 Introduction

In hydraulic fracturing, fluid/shale interaction inevitably happens during aqueous stimulation. Due to the large amount of water used in the process of hydraulic fracturing, fluid/shale interaction induces extensive dissolution of certain minerals in shale, resulting in an increase of shale porosity and softening of the shale matrix (Harrison et al., 2017). The fluid/shale reaction not only produces mineral dissolution but also generates secondary mineral precipitation in the matrix and the fractures, which acts as new proppant and low-permeability creator at the same time depending on different surficial conditions (Hakala et al., 2017). The ions transferred from shale into fluid is found to leach from clay mineral specifically (Zolfaghari et al., 2016). After 24 to 48 hours of this early stage, certain elements in the fluid either elevate or deplete during the following stage (Marcon et al., 2017). All these geochemical alterations need to be further understood from the prospective of the fundamental point of view regarding major mineral components in the reaction.

Over the past decade, the nanoindentation technique has been widely adopted on the studies of shale samples (Ulm & Abousleiman, 2006; Kumar et al., 2012; Shukla et al., 2013; Shukla et al., 2015; Bennett et al., 2015; Liu, 2015; Yang et al., 2016; Xiang et al., 2017; Yang et al., 2018). In previous studies, a clay-matrix-based criterion was developed for separation of clay matrix, quartz minerals, and carbonates minerals from scattered nanoindentation data. An Energy-based method was adopted (Cheng et al., 2002) to calculate the fracture toughness of shale via a load-displacement curve. Xiang et al. (2017) systematically illustrated the hardness-based criterion for data analysis and compared the anisotropy of shale samples. Fracture toughness is found to be anisotropic

with respect to bedding. It was concluded that the fracture toughness in the direction parallel to the bedding plane is 80% of that in the direction perpendicular to the bedding plane. To author's knowledge, no published literature has presented research on the weakening of shale via nanoindentation that only considering corresponding components instead of analyzing the matrix as a bulk material.

Poisson's ratio, fracture toughness and elastic modulus of shale are essential design parameters in hydraulic fracturing. The mechanics of the fracture processes is clearly important to understand and to predict the degree of rubblization and the resulting influence on the permeability of shale (Schmidt, 1977). Test methods and practices for measuring fracture toughness developed by American Society for Testing and Materials (ASTM) are in terms of both the linear elastic fracture mechanics and elastoplastic fracture mechanics. A long history of more than 50 years in the advancement of fracture mechanics theory can be divided into linear elastic materials testing (1950s to 1960s), elastoplastic materials testing (1970s to 1980s), transition materials (1990s), and thin-walled materials (2000s), respectively (Zhu & Joyce, 2012). However, limited conclusion or empirical correlations for fracture toughness have been proposed in terms of H and E in shale itself.

To better understand the fluid/shale interaction in fundamental terms of mechanical behavior and mineralogy alteration, this study only considers clay matrix as the major component in the fluid/shale interaction system, also relying on visual verification of SEM images illustrating how the authentic on-site fracturing fluids change the surface. Moreover, the correlation among the fracture toughness, hardness, and Young's modulus are presented statistically based on the designed experiment.

5.3 Materials and Methods

A hydraulic fracturing fluid sample was provided from an industry site in Houston, TX. The industry-supplied fluid sample is in yellow color with no significant viscosity different from water. Shale core samples were taken from the YS108 Well at a depth of 2390.11 m to 2506.61 m in Sichuan Basin, China. Due to the dual purposes of this study, two phases of experiments were designed. For Phase I, in order to examine interaction between shale samples and fracturing fluid, two clean shale samples were prepared into valid-size specimens for nanoindentation test and SEM imaging in general accordance with previous studies (Yang et al., 2016; Xiang et al., 2017; Yang et al., 2018;). The same source shale samples were then ground into dry powders using McCrone Micronising Mill for 17 minutes to reach a particle size of 2 μm (Locock et al., 2012). To obtain the mineralogy for XRD, the samples were then prepared by the razor tamped surface (RTS) method by Zhang et al. (2003). Without consideration of the in-situ hydrothermal conditions, the shale specimens and powder samples were then immersed in the onsite-obtained fracturing fluid for 7 days at room temperature. The micro-mechanical properties of the contaminated shale samples were measured again after the imbibition experiment. The mixture of powder samples with fracturing fluid was filtered using a vacuum filtering apparatus with the size opening of FG/F (0.7 μm). When the filtering process was complete, the cake-shape sediment was milled again for the subsequent XRD measurement.

In Phase II, a total of 8 clean shale samples were prepared and tested in general accordance with the procedure of nanoindentation testing used in Phase I. A typical residual indent of nanoindentation on Sichuan shale surface contaminated by Houston

hydraulic fracturing fluid is shown by means of SEM in Figure 5.1 for experiment phase I.

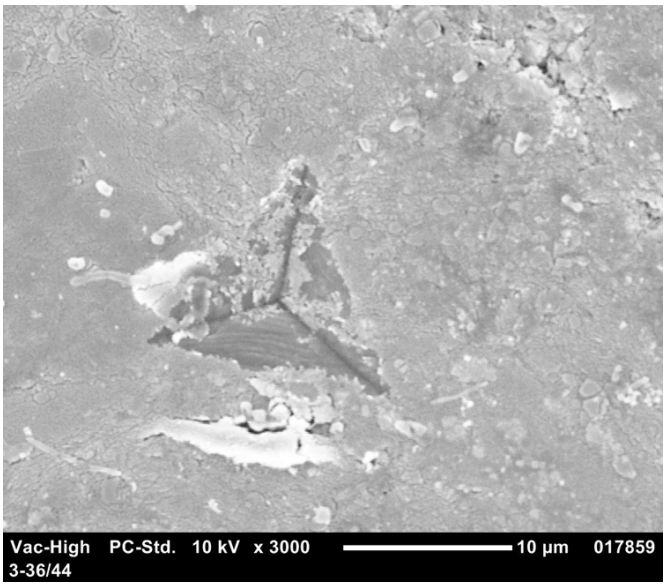

Figure 5.1 SEM image of Sichuan shale contaminated by Houston hydraulic fracturing fluid showing residual indent by a Berkovich diamond indenter

For obtaining the fracture toughness of shale, Liu (2015) investigated three different measurements of fracture toughness, where two energy methods were detailed. Of the two methods, for this study, the selected method was the one for quasi-brittle material without pop-ins on the load-displacement curves rather than the one emphasizing the delamination of the sample. Originally introduced for ductile materials by Cheng et al. (2002), fracture toughness, K_c, can be calculated by using the energy method. It is assumed that the fracture energy is accounted for as a portion of the irreversible energy and can be defined as the sum of the energy due to pure plasticity and the energy due to the cracking extension. During the process of indentation loading and unloading, the total energy, U_t, consists of two components: elastic energy, U_e, and plastic energy, U_p. U_p is irreversible work produced in the system, which is composed of

pure plastic energy, U_{pp}, and the induced fracture energy, U_{frac}. Their relations can be expressed as

$$U_t = U_e + U_p = U_e + U_{pp} + U_{frac} \quad \text{Eq. (5.1)}$$

where the total energy, U_t, and elastic energy, U_e, can be calculated from the nanoindentation load-displacement curve as

$$U_t = \int_0^{h_{max}-h_{creep}} F_L dh \quad \text{Eq. (5.2)}$$

$$U_e = \int_{h_r}^{h_{max}} F_{UL} dh - 0.01 F_{max} \times h_{th} \quad \text{Eq. (5.3)}$$

where F_L is loading; F_{UL} is unloading; h_{creep} is the creep displacement made by maximum constant load, F_{max}; h_r is the residual displacement; h_{th} is the thermal drift measured by system. Pure plastic energy, U_{pp} can be calculated by

$$U_{pp} = \left\{1 - \left[\frac{1-3\left(\frac{h_f}{h_{max}}\right)^2+2\left(\frac{h_f}{h_{max}}\right)^3}{1-\left(\frac{h_f}{h_{max}}\right)^2}\right]\right\} \times U_t \quad \text{Eq. (5.4)}$$

where the final displacement, $h_f = h_r - h_{th} - h_{creep}$, can be obtained. Then the fracture energy, U_{frac}, can be determined from

$$U_{frac} = U_p - U_{pp} \quad \text{Eq. (5.5)}$$

The definition of strain energy release rate, G_c, is the energy dissipated during fracture per created fracture surface area. It can be obtained by dividing the projected contact area, A_c, by the expression of

$$A_c = 24.5 h_c^2 \quad \text{Eq. (5.6)}$$

$$G_c = \frac{\partial U_{frac}}{\partial A_c} = \frac{U_{frac}}{A_c} \quad \text{Eq. (5.7)}$$

The fracture toughness, K_c, can then be calculated as the square root of strain energy release rate, G_c, multiplied by the reduced elastic modulus, E_r, by the expression of

$$K_c = \sqrt{G_c E_r} \quad \text{Eq. (5.8)}$$

where E_r is the reduced elastic modulus of the indentation contact, which can be calculated as follows,

$$E_r = \frac{1}{2\beta}\sqrt{\frac{\pi}{A_c}}S \quad \text{Eq. (5.9)}$$

where A_c is the projected contact area at F_{max} and h_{max}; β is a constant related to geometry of the indenter, taken as 1.05; S is the contact stiffness obtained from the slope of the initial unloading curve at the maximum indentation h_{max} (Oliver and Pharr, 1992),

$$S = \frac{dF}{dh}|_{h=h_{max}} \quad \text{Eq. (5.10)}$$

The Young's modulus E is calculated using the following expression,

$$E = \frac{1-\upsilon_s^2}{\frac{1}{E_r}-\frac{1-\upsilon_i^2}{E_i}} \quad \text{Eq. (5.11)}$$

where ν_s is the Poisson's ratio of the test sample and is assumed to be $\nu_s = 0.18$; ν_i is the Poisson's ratio of the diamond indenter ($\nu_i = 0.07$); E_i is the elastic modulus of the diamond indenter ($E_i = 1140$ GPa); E_r is the reduced elastic modulus of the indentation contact as mentioned in Eq. (9). The contact depth h_c can be calculated as

$$h_c = h_{max} - \varepsilon\frac{F_{max}}{S} \quad \text{Eq. (5.12)}$$

where ε is a constant related to the geometry of the indenter ($\varepsilon = 0.75$); the hardness of sample, H, can be expressed as

$$H = \frac{F_{max}}{A_c} \quad \text{Eq. (5.13)}$$

where A_c is also the projected contact area at F_{max} and h_{max}.

5.4 Results and Discussion

5.4.1 XRD Results

For comparison of clean shale and contaminated shale by hydraulic fracturing fluids for 7 days at room temperature, the XRD spectrum reveal a minor difference with a majority of the spectrum exhibiting the same pattern, as shown in Figure 5.2 and 5.3. All peak intensities were determined with the help of a commercial software, Profex. Assuming the aluminum/iron-substrate is as control, the alterations of minerals in shale can be obtained in Table 5.1 and 5.2. Table 5.1 provide an overview of how these components vary in the shale system. As shown in Table 5.1, quartz, clay mineral, feldspar, and carbonate are the dominant components in Sichuan shale samples. The introduction of NaCl is highly complex as a result of adsorption and crystal binding since the shale powder-fluid mixture was filtered, dried, and milled. However, the comparison of the results cannot be made without a control. The aluminum/iron-substrate in this study is assumed to be control. Therefore, the ratio comparison of other 7 minerals are provided when the results are normalized to the control shown in Table 5.2. All mineral contents except salts are found to decrease after the shale powder-fluid reaction, which might be a result of the chemical/physical reactions and the wash-out process in the experiment Phase I.

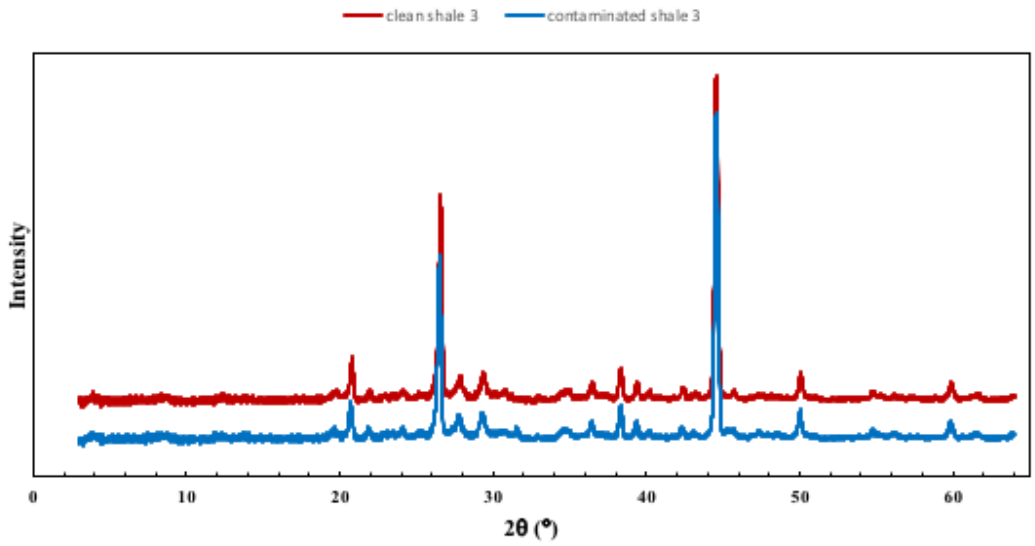

Figure 5.2 XRD result of Shale Sample 3

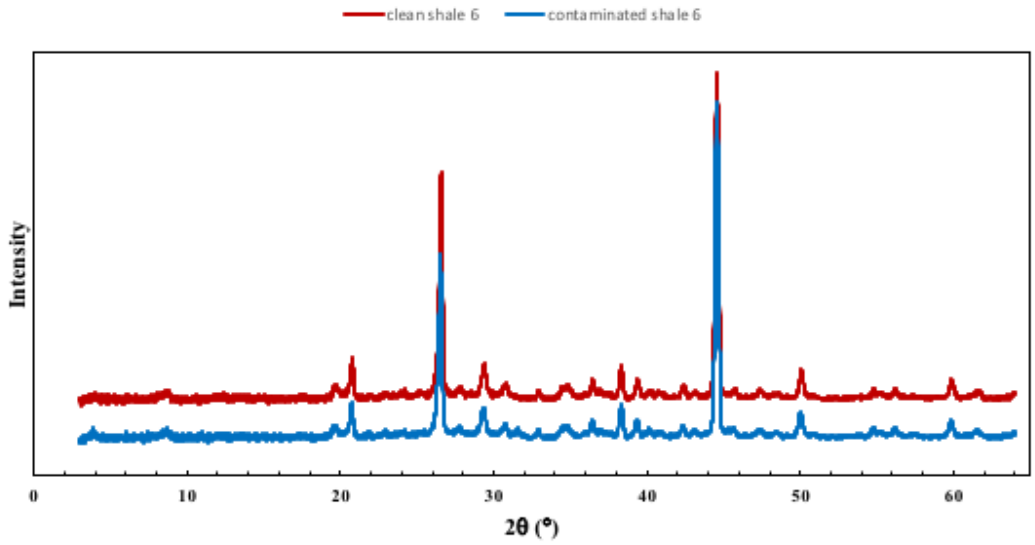

Figure 5.3 XRD result of Shale Sample 6

Table 5.1 Summary table of mineral percentage for contaminated shales from XRD

Material	Quartz	Illite	Albite	Calcite	Ankertie	Pyrite	NaCl	Substrate (Al+Iron)
Clean shale 3	37	16	11	13	2	1	-	20
Contaminated shale 3	36	15	11	11	2	1	1	24
Clean shale 6	39	20	3	10	5	2	-	21
Contaminated shale 6	35	19	3	10	5	2	1	25

Table 5.2 Ratio comparison of minerals for contaminated shales from XRD

Material	Quartz	Illite	Albite	Calcite	Ankertie	Pyrite	NaCl	Substrate (Al+Iron)
Clean shale 3	1.85	0.8	0.54	0.67	0.08	0.04	-	1.00
Contaminated shale 3	1.47	0.6	0.44	0.45	0.07	0.02	0.06	1.00
Clean shale 6	1.81	0.94	0.12	0.49	0.22	0.09	-	1.00
Contaminated shale 6	1.42	0.78	0.1	0.42	0.20	0.08	0.04	1.00

5.4.2 Nanoindentation Results for Fracturing Fluid-Contaminated Shale: Phase I

Two- or three-groups micromechanical property indices including H and E can be obtained using the clay-matrix-based criterion for all shale specimens. Figure 5.4 and 5.5 provide illustrative results for Specimen 3 after the contamination by hydraulic fracturing fluid for 7 days at room temperature. It is noted that the clay matrix in Specimen 3 has a hardness value of 1.41 ± 0.37 GPa and a Young's modulus value of 59.37 ± 11.25 GPa as

displacement reaches 2 μm. The clay matrix is observed to have a relatively stable hardness with less error bars compared with carbonates and quartz.

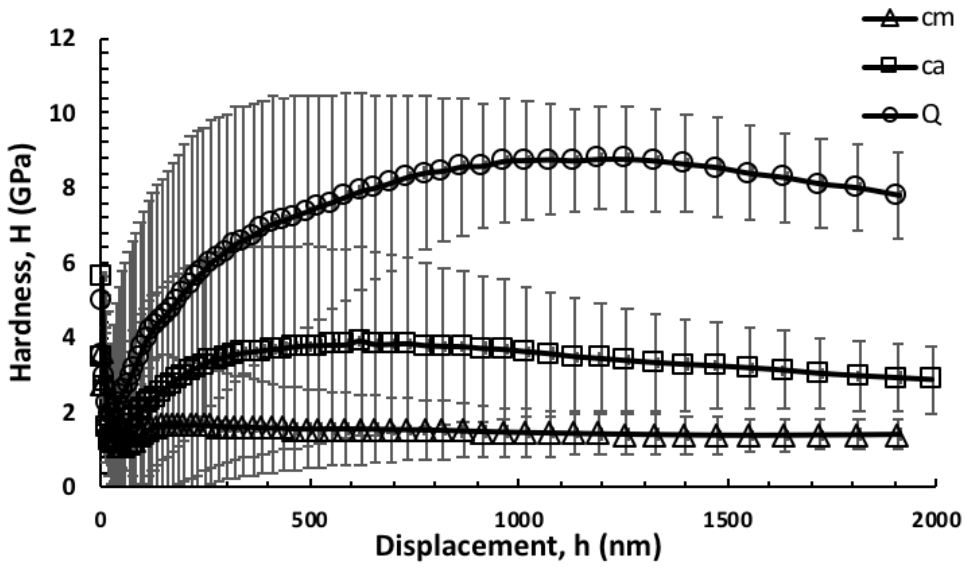

Figure 5.4 Hardness-displacement curve using clay-matrix based criterion for contaminated Shale Sample 3 by hydraulic fracturing fluid for 7 days at room temperature

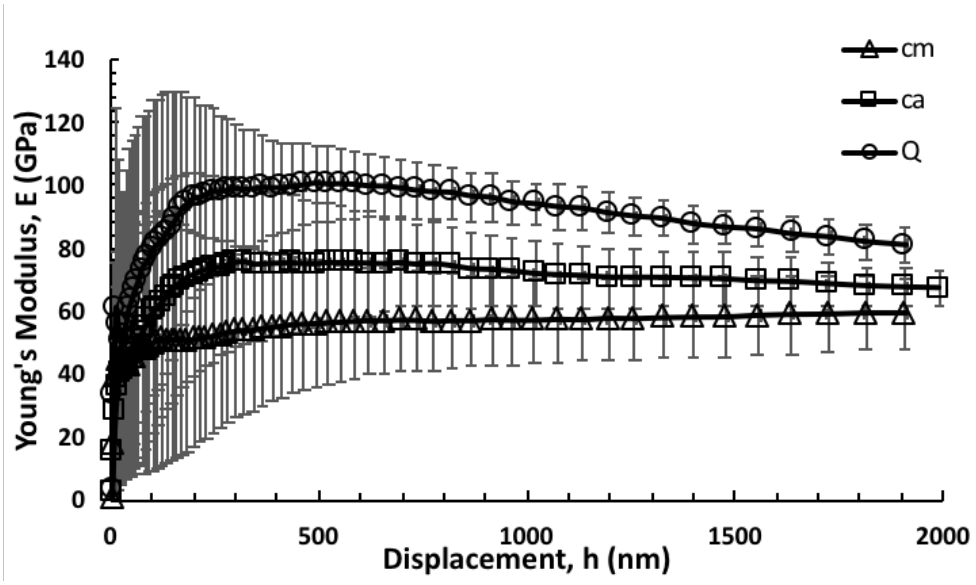

Figure 5.5 Young's modulus-displacement curve using clay-matrix based criterion for contaminated Shale Sample 3 by hydraulic fracturing fluid for 7 days at room temperature

As in the previous study on water-shale interaction, the analysis only considers the clay matrix as contributing to the softening of the shale. As it is shown in Figure 5.6 and 5.7, when considering clay matrix, fracturing fluid-contaminated shale specimen exhibits weaker hardness than clean shale at shallower depth but similar hardness with depth. The influence on the intrinsic property of the near-surface shale to fracturing fluid might be a major reason for the relative gap when the indent depth goes deeper as shown in Figure 5.6 but not Figure 5.7.

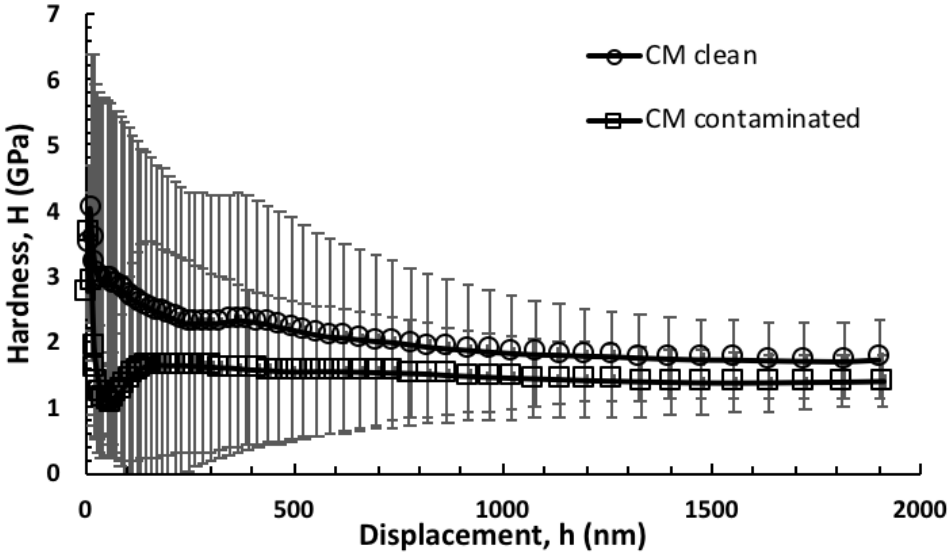

Figure 5.6 Hardness of clay matrix of Shale Sample 3 for clean and contaminated condition

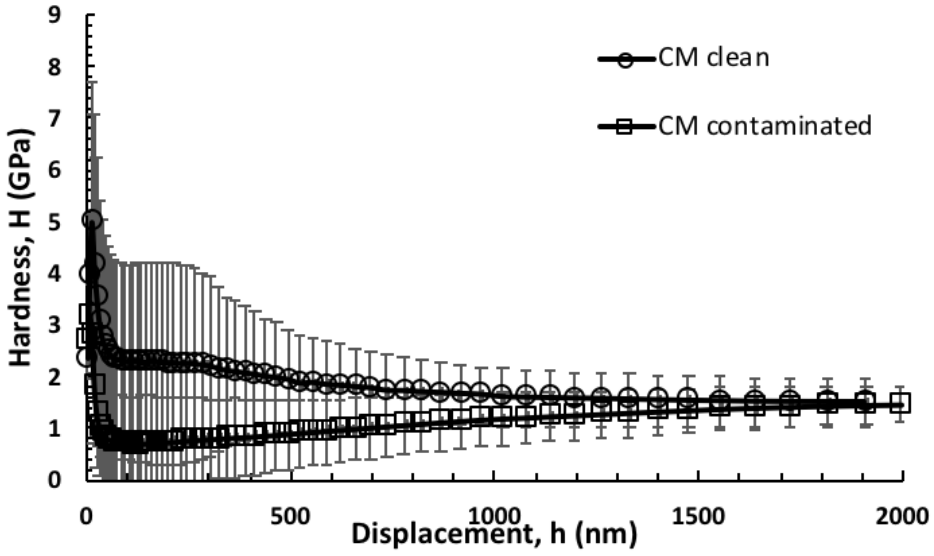

Figure 5.7 Hardness of clay matrix of Shale Sample 6 for clean and contaminated condition

Because of the permeability and hydraulic conductivity of the shale itself, hardness reduction percentages are different at different depths as it is shown in Figure 5.8 for Specimen 3 and 6. The Houston hydraulic fracturing fluid has an influence of 21% of hardness reduction on Sichuan shales at depth of 1.2 μm. When considering the hardness changes with XRD results in Table 5.1, the two samples exhibited different hardness resistance based on exposure to the fracturing fluid. The shale sample with higher clay mineral content exhibited a larger hardness reduction range with different depth by contamination. Shale Sample 3 with 16% of Illite indicates relatively narrower reduction range compared with Shale Sample 6 with 20% of Illite. Even though XRD provides quantitative analysis of the shale sample by contamination, the system hardness could not be accurately provided unless a constitutive equation is provided for the shale system. Clay matrix is assumed as the dominant component in the shale system. A characteristic depth, h_c, is defined as the depth when the reduction values are the same for

the clay matrix hardness and clay content by XRD. Therefore, Shale Sample 3 has a h_c of 700 nm with 24% reduction and Shale Sample 6 has a h_c of 1300 nm with 16.6% reduction as can be found in Figure 5.8.

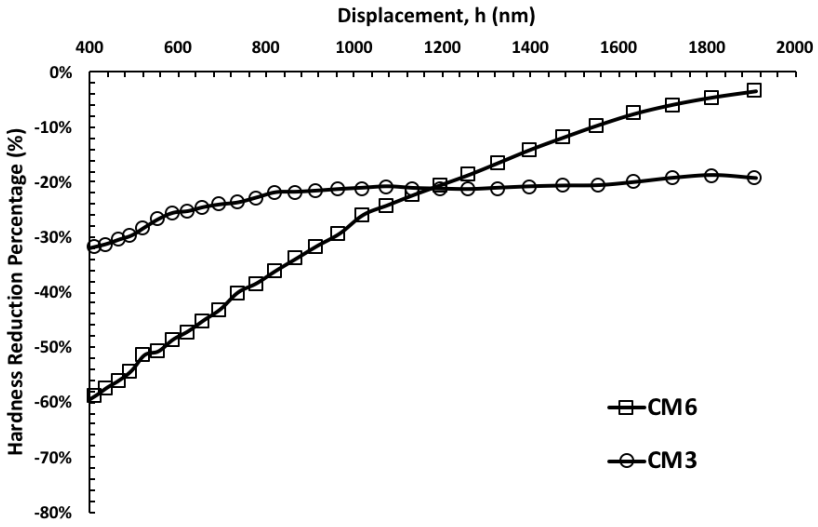

Figure 5.8 Observed hardness reduction of clay matrix with different depths for Shale Sample 3 and Shale Sample 6 of Sichuan shales contaminated by Houston hydraulic fracturing fluid

5.4.3 Relationship between Non-Crack System and H2/E: Phase II

Many researchers have investigated different types of cracks assumed in indentation fracture toughness tests. The Palmqvist crack system, Median crack system, and multiple curve fitting method were proposed in the past few decades (Lawn et al., 1980; Niihara, 1983). Either radial crack or Palmqvist crack was assumed. After visual observation in this study, the non-crack system was considered. Figure 5.9 shows how different brittle/ductile material behaves in a stress-strain curve. Shale in this study is assumed to behave as a brittle material, where the shadowed area, A, is related to the

calculated K_c value based on energy method in this study. The equations describing the relationship of K_c and H^2/E are presented from Eq. (5.14) to Eq. (5.17) as followed:

$$\varepsilon_y = \frac{\sigma_y}{E} \quad \text{Eq. (5.14)}$$

$$\sigma_y = a \times H \quad \text{Eq. (5.15)}$$

$$\mathrm{A} \cong \frac{1}{2} \times \varepsilon_y \times \sigma_y = \frac{1}{2} \times a^2 \times \frac{H^2}{E} \quad \text{Eq. (5.16)}$$

$$K_c \sim \beta \times \frac{H^2}{E} \quad \text{Eq. (5.17)}$$

where σ_y is the yield strength of material; E is Young's modulus of material; ε_y is the strain at the yield point; a is a coefficient of hardness, i.e. a = 3 in studies of metals (Tabor, 1956; Song et al., 2017); β is a constant.

Based on the obtained value K_c of clay matrix using the energy method, its trend with respect to H^2/E, H and E were provided in Figures 5.10 to 5.12. According to Eq. (5.17), the value of K_c is proportional to the H^2/E linearly. Results also imply that K_c can be approximately expressed by H or E linearly as well. Three different depths are presented in these figures, 500 nm, 1 μm, and 2 μm. These figures present a similar linear approximation that K_c of clay matrix increases with increasing values of H^2/E and H or E. For clay minerals, the data selection of deeper indentation is steeper than that with shallower indentation depth. The trendline for all of the data together can further be expressed by Eq. (5.18):

$$K_c = (-4.6879h^2 + 13.721h + 2.0133)\frac{H^2}{E} + (0.1564h^2 - 0.3662h + 1.3611) \quad \text{Eq. (5.18)}$$

where K_c is the fracture toughness in MPa $m^{0.5}$; h is the selected indentation depth in μm; H and E are the hardness in GPa and Young's modulus in GPa that obtained from nanoindentation experiments, respectively.

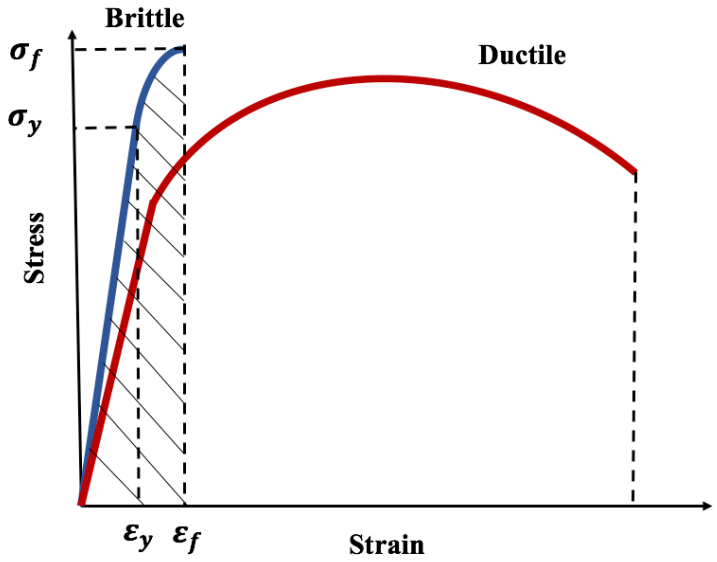

Figure 5.9 Stress-strain curves diagram for brittle and ductile materials

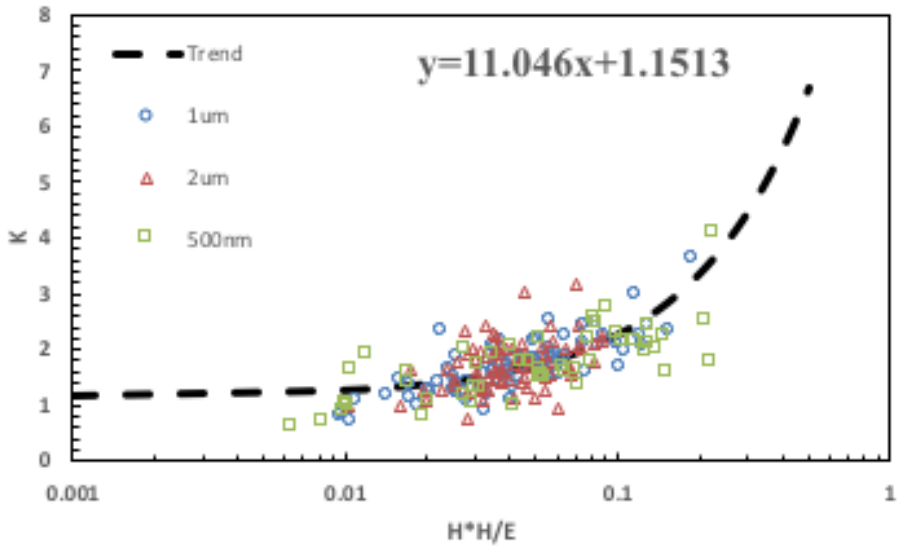

Figure 5.10 Trend of K_c with different H2/E when considering values obtained at depth of 1 μm, 2 μm, and 500 nm

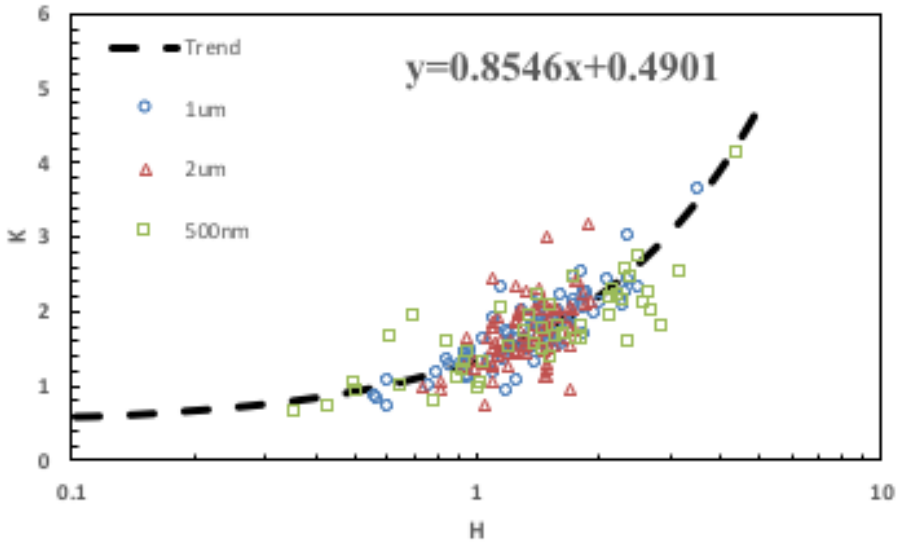

Figure 5.11 Trend of K_c with different H when considering values obtained at depth of 1 μm, 2 μm, and 500 nm

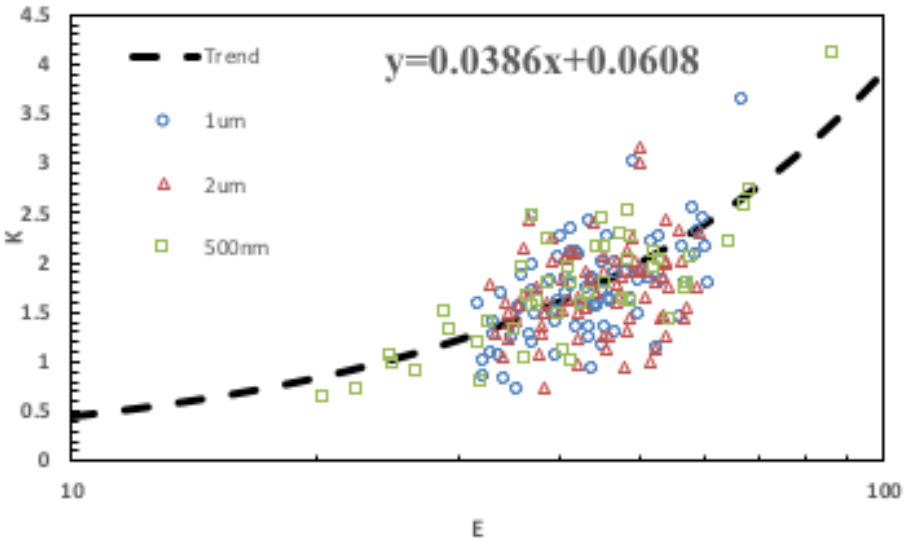

Figure 5.12 Trend of K_c with different E when considering values obtained at depth of 1 μm, 2 μm, and 500 nm

5.4.4 Effect of Indentation Size Effect

Figures 5.13 to 5.16 show results of the average trends of Young's modulus and hardness obtained from nanoindentation tests at depth of 500 nm, 1 μm, and 2 μm for clay matrix of Sichuan shale. Averaged values of E are found slightly higher with deeper depth ranging from 43.53 GPa to 44.78 GPa. The indentation size effect is clearly shown in the overall average hardness-displacement curve in Fig. 5.14, where the average hardness of clay matrix is observed to decrease with increasing indentation size ranging from 1.61 GPa to 1.35 GPa. The fracture toughness, K_c, as shown in Fig. 5.15 is found to be relatively uniform for clay matrix. In logarithm scale, values of H^2/E follow a similar trend of the combination of the E and H with respect to the displacement into surface (Fig. 5.16).

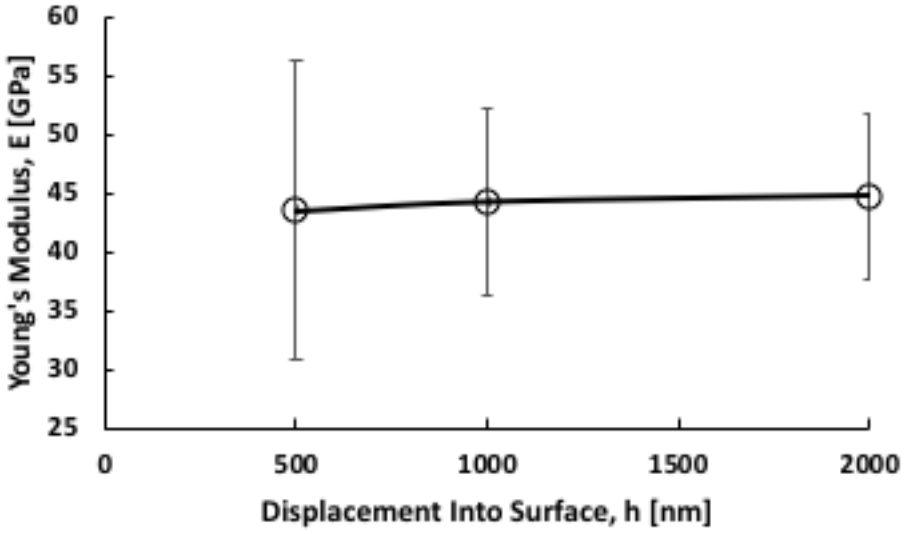

Figure 5.13 Average trends of Young's modulus and hardness obtained from nanoindentation tests at depth of 500 nm, 1 μm, and 2 μm for clay matrix

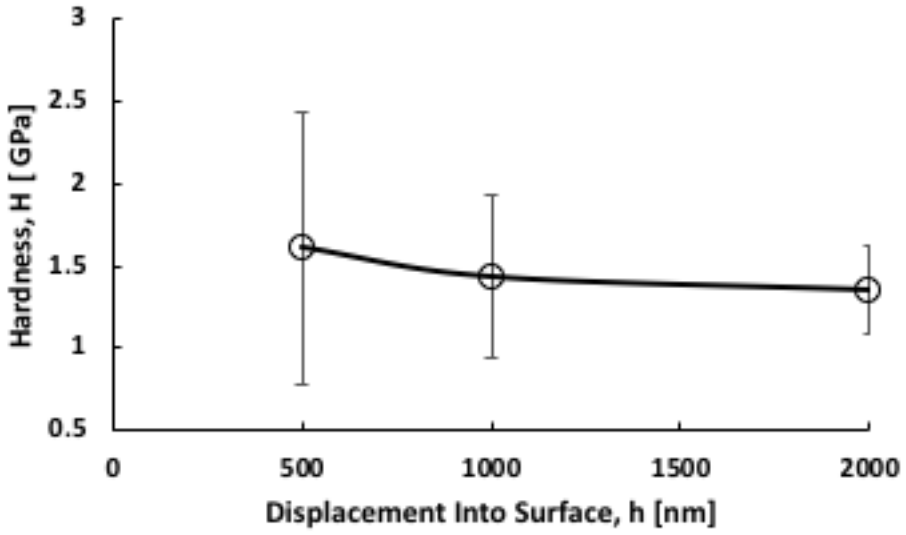

Figure 5.14 Average trends of hardness obtained from nanoindentation tests at depth of 500 nm, 1 μm, and 2 μm for clay matrix

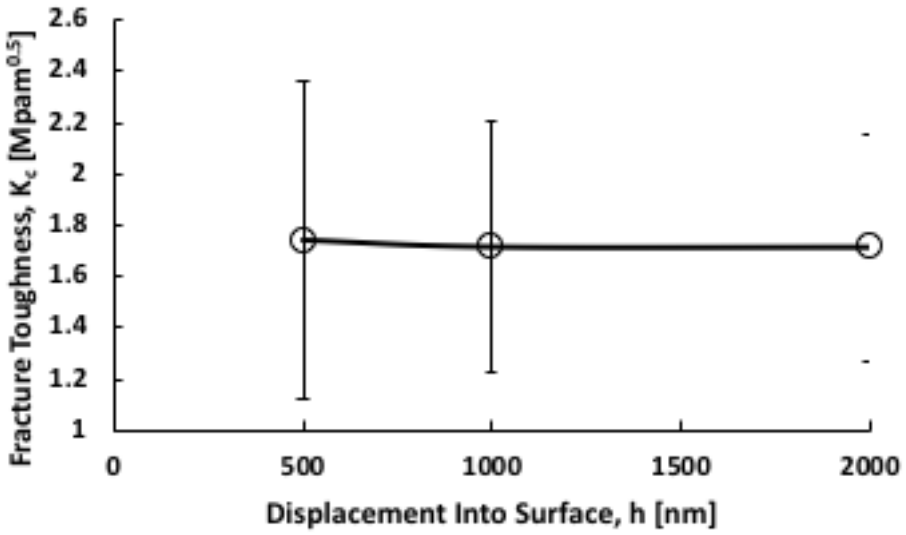

Figure 5.15 Average trends of fracture toughness from calculation at depth of 500 nm, 1 μm, and 2 μm for clay matrix

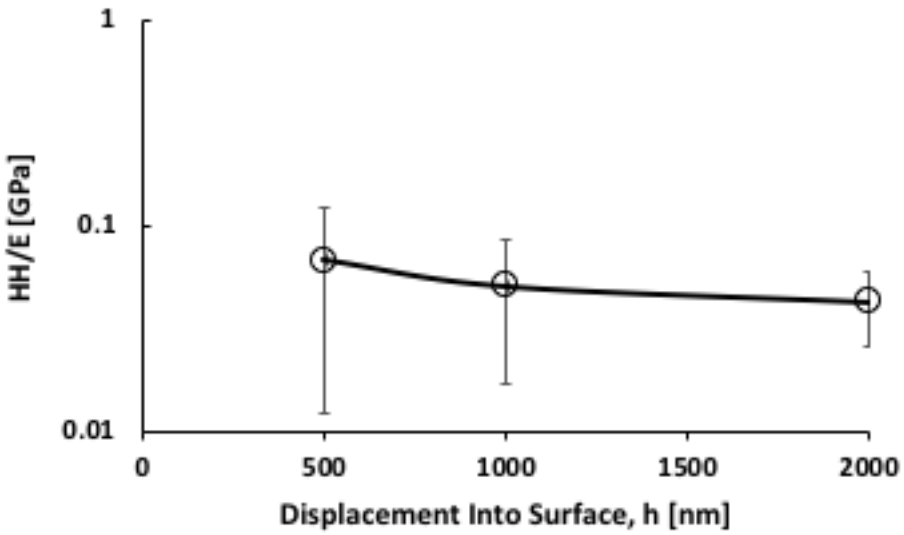

Figure 5.16 Trend of value of H2/E regarding different depth

Nix and Gao (1998) accurately modeled for crystalline materials employing the concept of geometrically necessary dislocations. The Nix-Gao model can be utilized to obtain a hardness of the clay matrix through:

$$\frac{H}{H_0} = \sqrt{1 + \frac{h^*}{h}} \qquad \text{Eq. (5.19)}$$

where H is the clay matrix hardness value obtained via nanoindentation; H_0 is the hardness at an infinite depth; h^* is a characteristic length which depends on the shape of the indenter, shear modulus, and H_0. The fitted Nix-Gao model is shown in Fig. 5.17 that the H_0 value for the clay matrix of Sichuan shale is 1.25 GPa. It is ideally fitted for the clay matrix. Therefore, the values extracted at indentation depth of 2 μm are preferential and closer to the Nix-Gao modeled results.

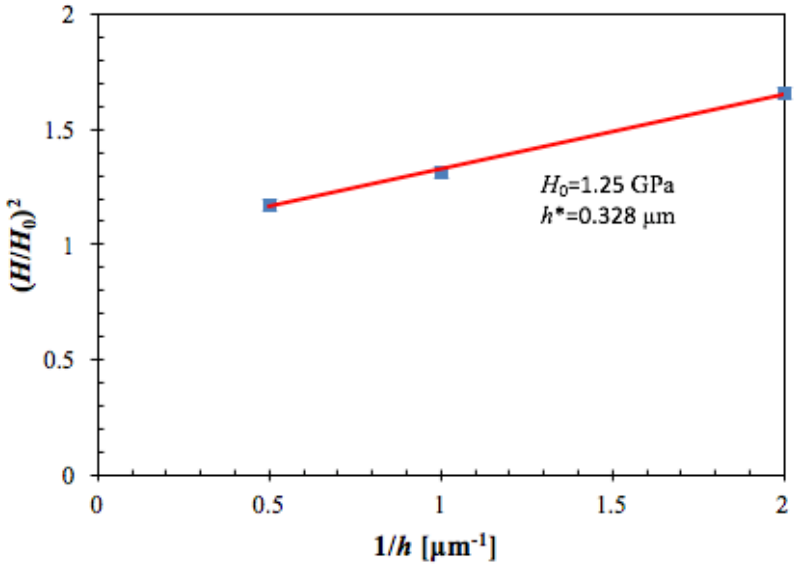

Figure 5.17 Nix-Gao model fitting for clay matrix of Sichuan shale

5.5 Summary and Conclusions

This paper provides the first trial study on the hydraulic fracturing fluid-shale interaction when only considering clay mineral as the primary factor by means of nanoindentation and XRD. The experiment phase II produced a correlation of the fracture toughness of shale with its Young's modulus and hardness. A clay-matrix-based criterion and an energy method were then used to screen and calculate the fracture toughness from the raw nanoindentation data. A few conclusions can be drawn as follows:

- NaCl increased about 4 to 6% when shale get contaminated by hydraulic fracturing fluid. However, all other minerals contents decreased after the shale powder-fluid interaction.
- Sichuan shale specimen has a hardness value of 1.41 ± 0.37 GPa and a Young's modulus value of 59.37 ± 11.25 GPa at depth of 2 μm.
- The previously proposed clay-matrix-based criterion provide fairly stable and reasonable grouping and separation in this study.

- The characteristic depth, h_c, is proposed to be based upon the reduction of hardness and mineral content at the same time.
- The non-crack system in this study was experimentally investigated to propose an empirical equation (Eq. 5.18) to describe fracture toughness using a selection of indentation depth, its corresponding hardness and Young's modulus.
- The Nix-Gao model can be utilized to obtain a hardness of the clay matrix. The H_0 value for the clay matrix of Sichuan shale is 1.25 GPa. Assuming the Nix-Gao Method as a representative way to provide unique characteristic value, nanoindentation results at a depth of 2 μm is preferential and closer to the Nix-Gao modeled results.

CHAPTER 6

CONCLUSIONS AND FUTURE WORK

6.1 Conclusions

A comprehensive experimental investigation was performed on shale and soils contaminated by industry-supplied hydraulic fracturing fluid. This study evaluated both shale sample and high-plasticity clay about their mechanical property changes due to the fluid/clay interaction. Based on the unique proposed data processing of nanoindentation for shale samples and the compared shear behavior of the high-plasticity clay samples contaminated by hydraulic fracturing fluid, many new major observations were made as follows:

- Hydrophobic OTMS coating can prevent water-induced softening of shale rocks. The OTMS-coated specimen has a 39.8% higher hardness, 25% higher Young's modulus, and 35% higher fracture toughness than the uncoated one.
- The proposed clay-matrix-based data-screening criterion is convenient for dealing with highly scattered nanoindentation data obtained from highly heterogeneous shales. The hardness of the constituent minerals in shale can be classified into three major groups: clay matrix, carbonates, and quartz with hardness values of 1.0 to 2.0 GPa, 2.5 to 6.0 GPa, and >7.0 GPa, respectively. The groupings of shale's constituent minerals can assist the understanding of the fluid/shale interactions and associated negative effects on shale's mechanical properties.
- LL and PL decrease with increasing contaminated concentration for CH clay.
- The value of C_v increases to a nearly uniform range with different contaminated concentrations from $C_{0.1}$ to C_1.

- Shear strength of CH clay increases with fracturing fluid contamination.
- Neither positive nor negative correlation is found for the C_c of fracturing fluid contaminated CH clay. The compressibility of high-plasticity clay shows a decrease and an increase afterward as the pore fluid concentration increases. Unless further studies on the variation of C_c with pore fluid concentration are accomplished, a general conclusion cannot be given.
- DS test with a shear deformation of 0.00694 mm/min is adequate to ensure no pore pressure is generated after verification with 48 hours of shearing. Performing DS test at a faster shear rate cannot provide accurate strength index for the contaminated mixture.
- The Hattab-Chang model is applicable for Heiden clay mixing with fracturing fluid. The effect of different pore fluid concentrations is provided with respect to the characteristic value of $\widetilde{A_N}/\widetilde{B}$.
- NaCl increased about 4 to 6% when shale get contaminated by hydraulic fracturing fluid. However, all other minerals contents decreased after the shale powder-fluid interaction.
- Sichuan shale specimen has a hardness value of 1.41 ± 0.37 GPa and a Young's modulus value of 59.37 ± 11.25 GPa at depth of 2 μm.
- The characteristic depth, h_c, is proposed to be based upon the reduction of hardness and mineral content at the same time.
- The non-crack system in this study was experimentally investigated to propose an empirical equation (Eq. (5.18)) to describe fracture toughness using a selection of indentation depth, its corresponding hardness and Young's modulus.

6.2 Anticipated Contribution to the Geomechanics and Geotechnical Community

The results of this study can be used in geomechanics and geotechnical community in the aspects of the following:

- Shale-fluid interactions via micro-scale rock mechanics can be characterized by only considering clay matrix. The tests will provide a few data sets of micromechanical characterization that could be used for future upscaling of correlationing with the macro-scale properties. This study also supplies a new means (OTMS) to prevent shale-fluid interactions that reduce the time of productive oil and gas production.
- A fundamental and first the research provided an understanding of the change of shear behavior of high-plasticity clay contaminated by hydraulic fracturing fluid. This resulted in useful geotechnical experimental data and a valid method of numerical modeling.
- A real case study of the currently and commercially used hydraulic fracturing fluids in United States on shale softening using nanoindentation is presented. The correlation among the fracture toughness, hardness, and Young's modulus is summarized statistically, which can provide an easier and better assessment of fracture toughness of shale.

6.3 Future Work

The findings on the fluid/clay interaction revealed the association between shear strength index and different pore fluid concentrations. However, more tests on different soils are needed to be performed to be incorporated in the Hattab-Chang numerical model domain.

The proposed testing procedure for shale/fluid interaction by means of nanoindentation on clay matrix of shale system provides a unique and reasonable way to define the shale softening. Future research will benefit from more experiments at closer in-situ geothermal condition such as high pressure and high temperature for shale core sample.

OTMS supplies a new means to prevent shale/fluid interactions that shorten the oil and gas production period. More chemicals can be coated on the shale surface to select a better candidate for the transition from hydrophilicity to hydrophobicity. Furthermore, based on the theoretical study on the surficial alteration, future research on OTMS and other candidate chemicals are expected to be effective for the transition like other additives used in the hydraulic fracturing process.

BIBLIOGRAPHY

Ahmed, U., Abou-Sayed, A. S., & Jones, A. H. (1979). SPE 7922 Experimental Evaluation Of Fracturing Fluid Interaction With Tight Reservoir Rocks And Propped Fractures. In SPE Symposium on Low Permeability Gas Reservoirs. Society of Petroleum Engineers.

Aiban, S. A. (1998). The Effect of Temperature on the Engineering Properties of Oil-Contaminated Sands. Environment International, 24(1), 153–161. http://doi.org/10.1016/S0160-4120(97)00131-1

Akrad, O., Miskimins, J., & Prasad, M. (2011). SPE 146658 The Effects of Fracturing Fluids on Shale Rock Mechanical Properties and Proppant Embedment. In SPE Annual Technical Conference and Exhibition. Society of Petroleum Engineers. http://doi.org/http://dx.doi.org/10.2118/146658-MS

Al-Haddabi, M., & Ahmed, M. (2007). Land disposal of treated saline oil production water: impacts on soil properties. Desalination, 212(1–3), 54–61. http://doi.org/10.1016/j.desal.2006.09.019

Al-Sanad HA, Eid WK, Ismael NF (1995) Geotechnical Properties of Oil-Contaminated Kuwaiti Sand. J Geotech Eng 121:407–412.

Al-Sanad HA, Ismael NF (1997) Aging Effects on Oil-Contaminated Kuwaiti Sand. J Geotech Geoenvironmental Eng 123:290–293.

Al-Sanad, H. A., & Ismael, N. F. (1997). Aging Effects on Oil-Contaminated Kuwaiti Sand. Journal of Geotechnical and Geoenvironmental Engineering, 123(3), 290–293.

Al-Sanad, H. A., Eid, W. K., & Ismael, N. F. (1995). Geotechnical Properties of Oil-Contaminated Kuwaiti Sand. Journal of Geotechnical Engineering, 121(5), 407–412.

Alberta Environment, "Salt Contamination Assessment & Remediation Guidelines," Environmental Sciences Division, Environmental Service, 2001, http://environment.gov.ab.ca/in- fo/library/6144.pdf.

Arasan, S. (2010). Effect of chemicals on geotechnical properties of clay liners: A review. Research Journal of Applied Sciences, Engineering and Technology, 2(8), 765–775.

Barbour, S. L., & Yang, N. (1993). A review of the influence of clay–brine interactions on the geotechnical properties of Ca-montmorillonitic clayey soils from western Canada. Canadian Geotechnical Journal, 30(6), 920–934. http://doi.org/10.1139/t93-090

Bennett, K. C., Berla, L. A., Nix, W. D., & Borja, R. I. (2015). Instrumented nanoindentation and 3D mechanistic modeling of a shale at multiple scales. Acta Geotechnica, 10(1), 1–14. http://doi.org/10.1007/s11440-014-0363-7

Bharat, T. V., & Sridharan, A. (2015). Prediction of Compressibility Data for Highly Plastic Clays Using Diffuse Double-Layer Theory. Clays and Clay Minerals, 63(1), 30–42. http://doi.org/10.1346/CCMN.2015.0630103

Bobko, C. P., Gathier, B., Ortega, J. A., Ulm, F., Borges, L., & Abousleiman, Y. N. (2011). The nanogranular origin of friction and cohesion in shale- A strength homogenization approach to interpretation of nanoindentation results. International Journal for Numerical and Analytical Methods in Geomechanics, 35, 1854–1876.

Bornert, M., Valès, F., Gharbi, H., & Nguyen Minh, D. (2010). Multiscale full-field strain measurements for micromechanical investigations of the hydromechanical behaviour of clayey rocks. Strain, 46(1), 33–46. http://doi.org/10.1111/j.1475-1305.2008.00590.x

Broz, M. E., Cook, R. F., & Whitney, D. (2006). Microhardness, toughness, and modulus of Mohs scale minerals. American Mineralogist, 91, 135–142.

Chen, P., Han, Q., Ma, T., & Lin, D. (2015). The mechanical properties of shale based on micro-indentation test. Petroleum Exploration and Development, 42(5), 723–732. http://doi.org/10.1016/S1876-3804(15)30069-0

Cheng, Y. T., Li, Z., & Cheng, C. M. (2002). Scaling relationships for indentation measurements. Philosophical Magazine A, 82(10), 1821–1829. http://doi.org/http://dx.doi.org/10.1080/01418610208235693

Comprehensive Environmental Inc. and the New Hampshire Department of Environmental Services. New Hampshire Stormwater Manual. Volume 3. Erosion and Sediment Controls During Construction. December 2008. Retrieved from http://des.nh.gov/organization/commissioner/pip/publications/wd/documents/wd-08-20c.pdf

Corapcioglu, H., Miskimins, J., & Prasad, M. (2014). Fracturing Fluid Effects on Young's Modulus and Enbedment in the Niobrara Formation. SPE Annual Technical Conference and Exhibition. Society of Petroleum Engineers. http://doi.org/http://dx.doi.org/10.2118/170835-MS

D. Anderson, "Effective saltwater remediation," NDPC Brine Task Force, Oasis Petroleum, 2015, https://www.ndoil.org/ image/cache/AndersonDustin.pdf.

D. Lloyd, "Drilling waste disposal in Alberta," in Proceedings of the National Conference on Disposal of Drilling Wastes, Environmental and Ground Water Institute, Norman, Okla, USA,May 1985.

Das, B. M., Sobhan, K. (2013). Principles of geotechnical engineering, 8th edition. Cengage Learning.

Deirieh, A., Ortega, J. A., Ulm, F. J., & Abousleiman, Y. (2012). Nanochemomechanical assessment of shale: A coupled WDS-indentation analysis. Acta Geotechnica, 7(4), 271–295. http://doi.org/10.1007/s11440-012-0185-4

Dieterich, M., Kutchko, B., & Goodman, A. (2016). Characterization of Marcellus Shale and Huntersville Chert before and after exposure to hydraulic fracturing fluid via feature relocation using field-emission scanning electron microscopy. Fuel, 182, 227–235. http://doi.org/http://dx.doi.org/10.1016/j.fuel.2016.05.061

Fadeev, A. Y., & McCarthy, T. J. (2000). Self-assembly is not the only reaction possible between alkyltrichlorosilanes and surfaces: monomolecular and oligomeric covalently attached layers of dichloro- and trichloroalkylsilanes on silicon. Langmuir, 16(18), 7268–7274. http://doi.org/10.1021/la000471z

Georgia Soil and Water Conservation Commission. Manual for Erosion and Sediment Control in Georgia. Six Edition, 2014. Retrieved from https://gaswcc.georgia.gov/sites/gaswcc.georgia.gov/files/Manual_for_Erosion_and_Sediment_Control_in_Georgia_Sixth_Edition_2014.pdf

Hakala, A., Crandall, D., Moore, J., Phan, T., & Lopano, C. (2017). Laboratory-Scale Studies on Chemical Reactions Between Fracturing Fluid and Shale Core From the Marcellus Shale Energy and Environmental Laboratory (MSEEL) Site. In Proceedings of the 5th Unconventional Resources Technology Conference. Tulsa, OK, USA: American Association of Petroleum Geologists. http://doi.org/10.15530/urtec-2017-2670856

Han, Q., Chen, P., & Ma, T. (2015). Influencing factor analysis of shale micro-indentation measurement. Journal of Natural Gas Science and Engineering, 27, 641–650. http://doi.org/10.1016/j.jngse.2015.09.010

Hangen, U. D. (2001). A Comparision of Nano-Hardness and Scratch- Resistance on Mobs Minerals. Zeitschrift Für Metallkunde, 92(9), 1074–1077.

Harrison, A. L., Jew, A. D., Dustin, M. K., Thomas, D. L., Joe-Wong, C. M., Bargar, J. R., … Maher, K. (2017). Element release and reaction-induced porosity alteration during shale-hydraulic fracturing fluid interactions. Applied Geochemistry, 82, 47–62. http://doi.org/10.1016/j.apgeochem.2017.05.001

Hattab, M., & Chang, C. S. (2015). Interaggregate Forces and Energy Potential Effect on Clay Deformation. Journal of Engineering Mechanics, 141(7), 4015014. http://doi.org/10.1061/(ASCE)EM.1943-7889.0000898

Hay, J. L., & Pharr, G. M. (2001). Instumented Indentation Testing. ASM Handbook.

Huang, S., & Torres-Verdín, C. (2016). Inversion-based interpretation of borehole sonic measurements using semianalytical spatial sensitivity functions. Geophysics, 81(2), D111–D124. http://doi.org/10.1190/geo2015-0335.1

Huang, S., Matuszyk, P. J., & Torres-Verdín, C. (2015). Spatial sensitivity functions for rapid numerical simulation of borehole sonic measurements in vertical wells. Geophysics, 80(5), D459–D480. http://doi.org/10.1190/geo2014-0587.1

Ingraffea, A. R., Wells, M. T., Santoro, R. L., & Shonkoff, S. B. C. (2014). Assessment and risk analysis of casing and cement impairment in oil and gas wells in Pennsylvania, 2000-2012. Proceedings of the National Academy of Sciences of the United States of America, 111(30), 10955–10960. http://doi.org/10.1073/pnas.1323422111

J. Pichtel, Fundamentals of Site Remediation for Metal- and Hydrocarbon-Contaminated Soils, Government Institutes, Rockville,Md, USA, 2nd edition, 2007

J. Sharma, A. V. Ogram, and A. Al-Agely, Mycorrhizae: Impli- cations for Environmental Remediation and Resource Con- servation, IFAS Extension ENH-1086, University of Florida, Gainesville, Fla, USA, 2015, http://ufdcimages.uflib.ufl.edu/IR/ 00/00/17/79/00001/EP35100.pdf.

Jaynes, W. F., & Boyd, S. A. (1991). Hydrophobicity of siloxane surfaces in smectites as revealed by aromatic hydrocarbon adsorption from water. Clays and Clay Minerals, 39(4), 428–436. http://doi.org/10.1346/CCMN.1991.0390412

Jia YG, Wu Q, Shang H, et al (2011) The influence of oil contamination on the geotechnical properties of coastal sediments in the Yellow River Delta, China. Bull Eng Geol Environ 70:517–525. doi: 10.1007/s10064-011-0349-8

Jia, Y. G., Wu, Q., Shang, H., Yang, Z. N., & Shan, H. X. (2011). The influence of oil contamination on the geotechnical properties of coastal sediments in the Yellow River Delta, China. Bulletin of Engineering Geology and the Environment, 70(3), 517–525. http://doi.org/10.1007/s10064-011-0349-8

Khamehchiyan M, Hossein Charkhabi A, Tajik M (2007) Effects of crude oil contamination on geotechnical properties of clayey and sandy soils. Eng Geol 89:220–229. doi: 10.1016/j.enggeo.2006.10.009

Khosravi E, Ghasemzadeh H, Sabour MR, Yazdani H (2013) Geotechnical properties of gas oil-contaminated kaolinite. Eng Geol 166:11–16. doi: 10.1016/j.enggeo.2013.08.004

Khosravi, E., Ghasemzadeh, H., Sabour, M. R., & Yazdani, H. (2013). Geotechnical properties of gas oil-contaminated kaolinite. Engineering Geology, 166, 11–16. http://doi.org/10.1016/j.enggeo.2013.08.004

Kumar, V., Sondergeld, C., & Rai, C. (2012). SPE 159804 Nano to Macro Mechanical Characterization of Shale. In SPE Annual Technical Conference and Exhibition. Society of Petroleum Engineers. http://doi.org/10.2118/159804-MS

Lafollette, R. F., & Carman, P. S. (2010). Proppant Diagenesis : Results So Far. In SPE Unconventional Gas Conference. Society of Petroleum Engineers4.

Lafollette, R. F., & Carman, P. S. (2013). SPE 166471 Comparison of the Impact of Fracturing Fluid Compositional pH on Fracture Wall Properties in Different Shale Formation Samples. In SPE Annual Technical Conference and Exhibition. Society of Petroleum Engineers.

Lambe TW, Whitman RV. (1969). Soil Mechanics, 1st Edn. Wiley, New York.

Lawn, B. R., Evans, A. G., & Marshall, D. B. (1980). Elastic/Plastic Indentation Damage in Ceramics: The Median/Radial Crack System. Journal of the American Ceramic Society, 63(9–10), 574–581. http://doi.org/10.1111/j.1151-2916.1980.tb10768.x

Liu, S. (2013). Laboratory Investigations on the Gechemical Response of Groundwater-sediment Environment to Hydraulic Fracturing Fluids. Ohio State University. Retrieved from https://etd.ohiolink.edu/rws_etd/document/get/osu1376501759/inline

Liu, Y. (2015). Fracture Toughness Assessment of Shales By Nanoindentation. University of Massachusetts Amherst. Retrieved from http://scholarworks.umass.edu/cgi/viewcontent.cgi?article=1003&context=cee_geotechnical

Llewellyn, G. T., Dorman, F., Westland, J. L., Yoxtheimer, D., Grieve, P., Sowers, T., … Brantley, S. L. (2015). Evaluating a groundwater supply contamination incident attributed to Marcellus Shale gas development. Proceedings of the National Academy of Sciences, 112(20), 6325–6330. http://doi.org/10.1073/pnas.1420279112

Locock, A. J., Chesterman, D., Caird, D., & Duke, M. J. M. (2012). Miniaturization of mechanical milling for powder X-ray diffraction. Powder Diffraction, 27(3), 189–193. http://doi.org/10.1017/S0885715612000516

Lutenegger, AJ and Rubin, A. (2008). "Tensile strength of some compacted fine-grained soils". Unsaturated Soils: Advances In Geo-Engineering. 608. Retrieved from http://scholarworks.umass.edu/cee_faculty_pubs/608

M. Ahmad, S. Soo Lee, J. E. Yang, H.-M. Ro, Y.Han Lee, and Y. Sik Ok, “Effects of soil dilution and amendments (mussel shell, cow bone, and biochar) on Pb availability and phytotoxicity in military shooting range soil,” Ecotoxicology and Environmental Safety,vol.79, pp.225–231,2012.

M. E. Sumner, “Sodic soils: new perspectives,” Australian Journal of Soil Research,vol.31, no.6,pp. 683–750, 1993.

Marcon, V., Joseph, C., Carter, K. E., Hedges, S. W., Lopano, C. L., Guthrie, G. D., & Hakala, J. A. (2017). Experimental insights into geochemical changes in hydraulically fractured Marcellus Shale. Applied Geochemistry, 76, 36–50. http://doi.org/10.1016/j.apgeochem.2016.11.005

McLaughlin, M. C. (2016). Environmental fate of hydraulic fracturing fluid additives after spillage on agricultural topsoil (Doctoral dissertation, Colorado State University. Libraries).

McLaughlin, M. C., Borch, T., & Blotevogel, J. (2016). Spills of Hydraulic Fracturing Chemicals on Agricultural Topsoil: Biodegradation, Sorption, and Co-contaminant Interactions. Environmental Science & Technology, 50(11), 6071–6078. http://doi.org/10.1021/acs.est.6b00240

Meegoda NJ, Ratnaweera P (1994) Compressibility of contaminated fine-grained soils. Geotech Test J 17:101–112. doi: 10.1520/GTJ10078J

Meegoda, B. N. J., & Rajapakse, R. A. (1993). Short-Term and Long-Term Permeabilities of Contaminated Clays. Journal of Environmental Engineering, 119(4), 725–743.

Meegoda, N. J., & Ratnaweera, P. (1994). Compressibility of contaminated fine-grained soils. Geotechnical Testing Journal, 17(1), 101–112. http://doi.org/10.1520/GTJ10078J

Menčik, J., & Swain, M. V. (1995). Errors associated with depth-sensing microindentation tests. Journal of Materials Research, 10(6), 1491–1501. http://doi.org/10.1557/JMR.1995.1491

Moore, C. A., & Mitchell, J. K. (1974). Electromagnetic Forces and Soil Strength. Géotechnique, 24(4), 627–640.

Mrdjen, I., & Lee, J. (2016). High volume hydraulic fracturing operations: potential impacts on surface water and human health. International Journal of Environmental Health Research, 26(4), 361–380. http://doi.org/10.1080/09603123.2015.1111314

Nasehi, S. A., Uromeihy, A., Nikudel, M. R., & Morsali, A. (2016). Influence of Gas Oil Contamination on Geotechnical Properties of Fine and Coarse-Grained Soils. Geotechnical and Geological Engineering, 34(1), 333–345. http://doi.org/10.1007/s10706-015-9948-7

Nazir, A. K. (2011). Effect of motor oil contamination on geotechnical properties of over consolidated clay. Alexandria Engineering Journal, 50(4), 331–335. http://doi.org/10.1016/j.aej.2011.05.002

Niihara, K. (1983). A fracture mechanics analysis of indentation-induced Palmqvist crack in ceramics. Journal of Materials Science Letters, 2(5), 221–223. http://doi.org/10.1007/BF00725625

Nix, W. D., & Gao, H. J. (1998). Indentation size effects in crystalline materials: A law for strain gradient plasticity. Journal of the Mechanics and Physics of Solids, 46(3), 411–425. http://doi.org/10.1016/s0022-5096(97)00086-0

Olchawa A, Kumor M (2007) Compressibility of organic soils polluted with diesel oil. Arch Hydroengineering Environ Mech 54:299–307.

Olchawa, A., & Kumor, M. (2007). Compressibility of organic soils polluted with diesel oil. Archives of Hydroengineering and Environmental Mechanics, 54(4), 299–307.

Olgun, M., & Yildiz, M. (2010). Effect of organic fluids on the geotechnical behavior of a highly plastic clayey soil. Applied Clay Science, 48(4), 615–621. http://doi.org/10.1016/j.clay.2010.03.015

Oliver, W. C., & Pharr, G. M. (1992). An improved technique for determining hardness and elastic modulus using load and displacement sensing indentation experiments. Journal of Materials Research, 7(6), 1564–1583.

Oliver, W. C., & Pharr, G. M. (2004). Measurement of hardness and elastic modulus by instrumented indentation: Advances in understanding and refinements to methodology. Journal of Materials Research, 19(1), 3–20. http://doi.org/10.1557/jmr.2004.19.1.3

Pan, S., Zou, C., Yang, Z., Dong, D., Wang, Y., Wang, S., … Wang, Z. (2015). Methods for Shale Gas Play Assessment : A Comparison between Silurian Longmaxi Shale and Mississippian Barnett Shale. Journal of Earth Science, 26(2), 285–294. http://doi.org/10.1007/s12583-015-0524-0

Pant, R., Hu, L., & Zhang, G. (2013). Anisotropy of Mica Probed by Nanoindentation. In Multiphysical Testing of Soils and Shales (pp. 239–245). Springer-Verlag Berlin Heidelberg.

Pichtel, J. (2016). Oil and Gas Production Wastewater: Soil Contamination and Pollution Prevention. Applied and Environmental Soil Science, 2016, 1–24. http://doi.org/10.1155/2016/2707989

Potter, P. E., Maynard, J. B., & Pryor, W. A. (1980). Sedimentology of Shale: Study Guide and Reference Source. Springer-Verlag New York Inc.

Puri, V. K. (2000). Geotechnical Aspects of Oil-Contaminated Sands Geotechnical Aspects of Oil- Contaminated Sands. Soil and Sediment Contamination, 9(4), 359–374.

Rahman, Z. A., Hamzah, U., Taha, M. R., Ithnain, N. S., & Ahmad, N. (2010). Influence of Oil Contamination on Geotechnical Properties of Basaltic Residual Soil. American Journal of Applied Sciences, 7(7), 954–961. http://doi.org/10.3844/ajassp.2010.954.961

Ratnaweera, P., & Meegoda, J. (2006). Shear Strength and Stress-Strain behavior of Contaminated Soils. Geotechnical Testing Journal, 29(2), 12686. http://doi.org/10.1520/GTJ12686

Sang, W., Stoof, C. R., Zhang, W., Morales, V. L., Gao, B., Kay, R. W., Steenhuis, T. S. (2014). Effect of hydrofracking fluid on colloid transport in the unsaturated zone. Environmental Science and Technology, 48(14), 8266–8274. http://doi.org/10.1021/es501441e

Schmidt, R. A. (1977). Fracture Mechanics of Oil Shale-Unconfined Fracture Toughness, Stress Corrosion Cracking, and Tension Test Results. In Energy Resources and Excavation Technology: Proceedings, 18th U.S. Symposium on Rock Mechanics, held at Keystone, Colorado (p. 2A2-1-2A2-6). Keystone, Colorado: Golden, Colo.: Colorado School of Mines Press, 1977.

Shin, E. C., & Das, B. M. (2001). Bearing Capacity of Unsaturated Oil-Contaminated Sand. International Journal of Offshore and Polar Engineering, 11(3).

Shukla, P., Kumar, V., Curtis, M., Sondergeld, C. H., & Rai, C. S. (2013). Nanoindentation Studies on Shales. In 47th US Rock Mechanics/Geomechanics Symposium (pp. 1194–1203).

Shukla, P., Taneja, S., Sondergeld, C., & Rai, C. (2015). Nanoindentation Measurement on Rocks. In Fracture, Fatigue, Failure, and Damage Evolution (Vol. 5, pp. 99–105).
Song, J., Sun, Q., Yang, Z., Luo, S., Xiao, X., Arwade, S. R., & Zhang, G. (2017). Effects of microporosity on the elasticity and yielding of thin-walled metallic hollow spheres. Materials Science and Engineering: A, 688(January), 134–145. http://doi.org/10.1016/j.msea.2017.01.105
Sridharan, A., & Jayadeva, M. S. (1982). Double layer theory and compressibility of clays. Géotechnique, 32(2), 133–144. http://doi.org/10.1680/geot.1982.32.2.133
Tabor, D. (1956). The physical meaning of indentation and scratch hardness. British Journal of Applied Physics, 7(5), 159. http://doi.org/10.1088/0508-3443/7/5/301
Tran, M. H., Chen, S., Rafael, S. P., Abousleiman, Y. N., & Slatt, R. M. (2014). A Geomechanics Approach to Evaluate Gas Shale Frackability : A Case Study with the Woodford Shale *, 50913.
U.S. Energy Information Administration. (2015). Annual Energy Outlook 2015 with projections to 2040. Retrieved from http://www.eia.gov/forecasts/aeo/
U.S. EPA. (2015). Assessment of the Potential Impacts of Hydraulic Fracturing for Oil and Gas on Drinking Water Resources (External Review Draft). U.S. Environmental Protection Agency, Washington, DC. http://doi.org/EPA/600/R-15/047a
Ulm, F. J., Vandamme, M., Bobko, C., Alberto Ortega, J., Tai, K., & Ortiz, C. (2007). Statistical indentation techniques for hydrated nanocomposites: Concrete, bone, and shale. Journal of the American Ceramic Society, 90(9), 2677–2692. http://doi.org/10.1111/j.1551-2916.2007.02012.x
Ulm, F. J., Vandamme, M., Jennings, H. M., Vanzo, J., Bentivegna, M., Krakowiak, K. J., … Van Vliet, K. J. (2010). Does microstructure matter for statistical nanoindentation techniques? Cement and Concrete Composites, 32(1), 92–99. http://doi.org/10.1016/j.cemconcomp.2009.08.007
Ulm, F.-J., & Abousleiman, Y. (2006). The nanogranular nature of shale. Acta Geotechnica, 1(2), 77–88. http://doi.org/10.1007/s11440-006-0009-5
USEPA, 1990. Test Methods for Evaluating Solid Wastes. Physical/Chemical Methods, SW-846, third ed., Washington D.C., USA
Van Oss, C. J., & Giese, R. F. (1995). The hydrophilicity and hydrophobicity of clay minerals. Clays and Clay Minerals, 43(4), 474–477. http://doi.org/10.1346/CCMN.1995.0430411
Vengosh, A., Jackson, R. B., Warner, N., Darrah, T. H., & Kondash, A. (2014). A critical review of the risks to water resources from unconventional shale gas development and hydraulic fracturing in the United States. Environmental Science and Technology, 48(15), 8334–8348. http://doi.org/10.1021/es405118y
Ward, O., Singh, A., & Van Hamme, J. (2003). Accelerated biodegradation of petroleum hydrocarbon waste. Journal of Industrial Microbiology and Biotechnology, 30(5), 260–270. http://doi.org/10.1007/s10295-003-0042-4
Wilson, M. J., & Wilson, L. (2014). Clay mineralogy and shale instability: an alternative conceptual analysis. Clay Minerals , 49(2), 127–145. http://doi.org/10.1180/claymin.2014.049.2.01

Wolf, D. C., Brye, K. R., & Gbur, E. E. (2015). Using Soil Amendments to Increase Bermuda Grass Growth in Soil Contaminated with Hydraulic Fracturing Drilling Fluid. Soil and Sediment Contamination: An International Journal, 24(8), 846–864. http://doi.org/10.1080/15320383.2015.1064087

Wong, R. (1998). Swelling and softening behaviour of La Biche shale. Canadian Geotechnical Journal, 35, 206–221. http://doi.org/10.1139/t97-087

Xiang, D., Chen, Z., Yang, Z., Wang, S., Wang, Q., Hou, D., & Zhang, G. (2017). Probing the Mechanical Properties of Shales by Nanoindentation. In Geotechnical Frontiers 2017.

Yang, Z., Wang, L., Chen, Z., Xiang, D., Hou, D., Ho, C. L., & Zhang, G. (2018). Micromechanical Characterization of Fluid/Shale Interactions by Means of Nanoindentation. SPE Reservoir Evaluation & Engineering, Preprint(Preprint). http://doi.org/10.2118/181833-PA

Yang, Z., Wang, L., Zhang, G., & Ho, C. (2016). Micromechanical Characterization of Fluid-Shale Interactions via Nanoindentation. In SPE Asia Pacific Hydraulic Fracturing Conference. Society of Petroleum Engineers. http://doi.org/10.2118/181833-MS

Yin, H., & Zhang, G. (2011). Nanoindentation Behavior of Muscovite Subjected to Repeated Loading. Journal of Nanomechanics and Micromechanics, 1(2), 72–83. http://doi.org/10.1061/(ASCE)NM.2153-5477.0000033.

Zeng, L., Wang, L. S., Xu, H. X., Jiao, Y. G., Cui, S. N., Han, H., & Zhang, B. S. (2010). The Oil and Gas Industry Standard of the People's Republic of China: Analysis method for clay minerals and ordinary non—clay minerals in sedimentary rocks by the X—ray diffraction (SY/T5163–2010)

Zhang, G., Germaine, J. T., Martin, R. T., & Whittle, A. J. (2003). A simple sample-mounting method for random powder X-ray diffraction. Clays and Clay Minerals, 51(2), 218–225. http://doi.org/10.1346/CCMN.2003.0510212

Zhang, G., Wei, Z., & Ferrell, R. E. (2009). Elastic modulus and hardness of muscovite and rectorite determined by nanoindentation. Applied Clay Science, 43(2), 271–281. Retrieved from http://cat.inist.fr/?aModele=afficheN&cpsidt=21095665

Zhu, X. K., & Joyce, J. A. (2012). Review of fracture toughness (G, K, J, CTOD, CTOA) testing and standardization. Engineering Fracture Mechanics, 85, 1–46. http://doi.org/10.1016/j.engfracmech.2012.02.001

Zolfaghari, A., Dehghanpour, H., Noel, M., & Bearinger, D. (2016). Laboratory and field analysis of flowback water from gas shales. Journal of Unconventional Oil and Gas Resources, 14, 113–127. http://doi.org/10.1016/j.juogr.2016.03.004